UNIVERSITY OF COPENHAGEN

PhD Thesis

Gabija Kiršanskė

Electrical control of excitons in semiconductor nanostructures:

from quantum dots in photonic-crystal devices
to the exciton Mott transition in coupled quantum wells

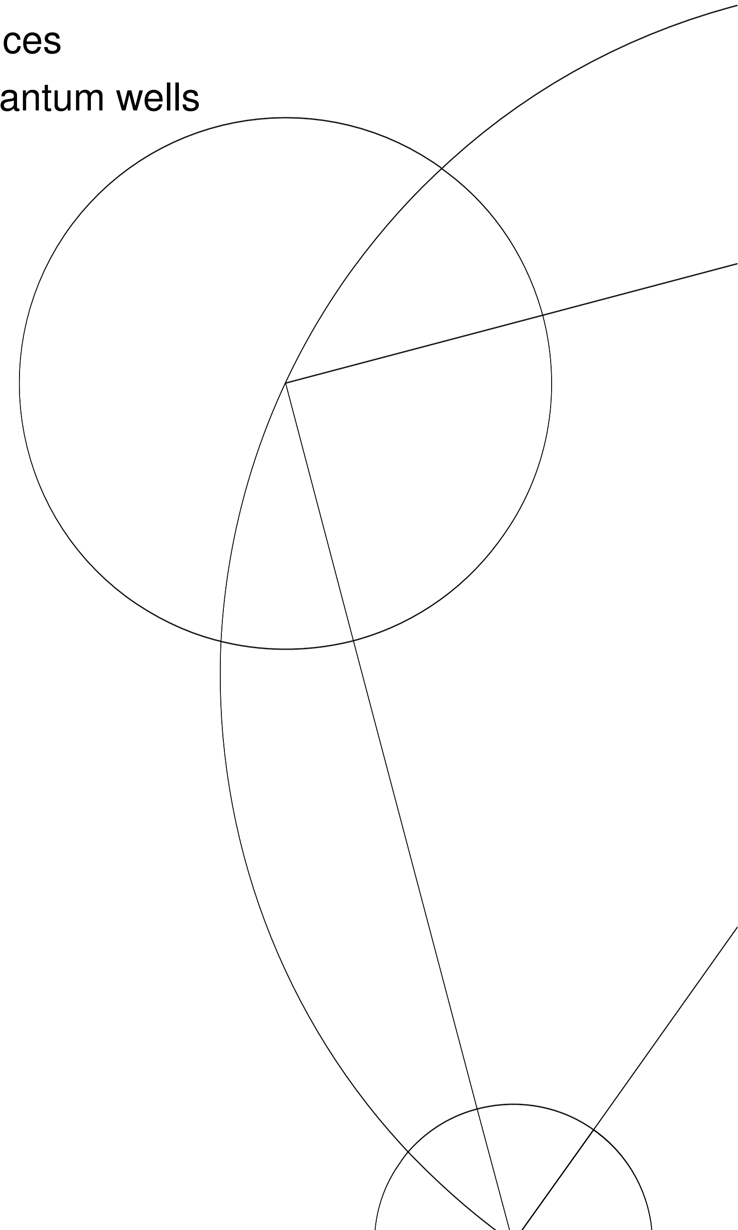

Prof. Peter Lodahl, Assoc. Prof. Søren Stobbe

Monday 1st February, 2016

Preface

The research presented in this thesis has been conducted from January 2013 to February 2016 at the Niels Bohr Institute, University of Copenhagen, and partially during an external stay at the Leibniz Institute for Solid State and Materials Research in Dresden. During the period I was enrolled as a PhD student in the Quantum Photonics group under the supervision of Prof. Peter Lodahl and Assoc. Prof. Søren Stobbe.

First of all, I would like to thank Peter for giving me the opportunity to explore many different topics in the field of quantum photonics. I express my gratitude for all the guidance and encouragement I have received from him. In addition to Peter, I was fortunate enough to have had Søren as my co-supervisor. He has been a constant source of support during my studies. I greatly appreciate his dedication to my research projects.

I would like to thank all the current and former members of the Quantum Photonics group, who contributed to the work reported in this thesis. The fabrication processes discussed in Chapter 2 were developed together with Leonardo Midolo and Tommaso Pregnolato. It was a pleasure to work with Leonardo, who shared his immense experience in the fabrication. I learnt a great deal about physics and beyond when co-supervising the master student project of Tommaso. The fabrication facilities were setup under the supervision of Søren Stobbe and with a significant contribution of Haitham El-Ella. I am indebted to Alisa Javadi and David García for fruitful discussions and feedback on the work presented in Chapter 3. Much of the experimental work discussed in Chapter 5 evolved from initial experiments performed by Raphaël Daveau. I am grateful to him for the help and pleasant company during the measurements in the bath cryostat. Also, I would like to thank Petru Tighineanu for his contribution with the sample design and many stimulating discussions to the work presented in Chapter 5.

I wish to express my gratitude to all the members of the Quantum Photonics group, who have introduced me to the optical setups and have patiently assisted in the lab throughout the years of my PhD: Kristian Høeg Madsen for introducing me to the closed-cycle cryostat, David García, Alisa Javadi, Tau Lehmann, Immo Söllner, and Petru Tighineanu for their assistance with the flow cryostat, and Marta Arcari for teaching me how to use the bath cryostat. I would also like to thank the group members for reading my thesis draft and giving me useful comments.

A sincere thanks goes to Dr. Fei Ding, Yan Chen, and Prof. Oliver Schmidt for teaching me about the strain effects on quantum dots during my stay in Dresden. The results on this topic are presented in Chapter 4. It was a pleasant stay in Dresden, and for that I want to thank several people, among them Britta Koch, Stefan Böttner, Sonja Maria Marz, and Lukas Schwarz.

Throughout this PhD project, numerous encounters with various technical challenges in the cleanroom and the optics labs have been solved with a tremendous help from the technical staff, particularly, from Nader Payami and Shivendra Upadhyay in the cleanroom, Axel Boisen, Preben Nørregaard, and Bent Jensen in the electronics workshop, and Dennis Wistisen, Erik Grønbæk, Carsten Mortensen, and Thomas Hedegaard in the mechanics workshop.

During my time at the Niels Bohr Institute, I have enjoyed the friendly atmosphere in the office, which I shared with Kristian Høeg Madsen, Immo Söllner, Tommaso Pregnolato, and Sasha Kyriienko. A special thanks goes to them. For the cosy coffee breaks and the unforgettable julefrokost I am grateful to the people in the Quantop group. Many thanks to Georgios Vasilakis for his friendship and kindness. My sincere thanks also goes to the friendly crowd of the cleanroom. With my highest respect, I would like to thank Claude, Frédéric, Piotr, Johann, and Wolfgang for the inspiration when writing the thesis.

The inspiring and enjoyable environment in the Quantum Photonics group would not have been possible without the aforementioned members of the group as well as Sahand Mahmoodian, Sofie Lindskov Hansen, and Camille Papon, with whom there is no casual lunch or a typical Friday night out. Instead, everyday we are perfecting the art of negotiation and debate, which leads to useful and/or enjoyable discussions about science and life, and is a constant source of laughter and good emotions.

Finally, I would like to thank my friends and family, especially my parents, for their continuous support through all the years. My deepest gratitude goes to my husband Gediminas, who makes it all worthwhile.

Abstract

The scope of this thesis covers investigation of the exciton Mott transition in coupled quantum wells, fabrication of photonic-crystal structures with embedded self-assembled quantum dots, and tuning of their properties by means of an external electric field.

In the first part of the thesis the focus is on quantum dots in photonic nanostructures. The fabrication process of reproducible high-quality photonic-crystal structures on electrically gated GaAs samples is presented. This process is employed to investigate light localization in short photonic-crystal waveguides with a dispersion relation facilitating a slow-light effect. The effect of the variations in the local density of optical states on electrically tuned quantum dots embedded in photonic structures is investigated. An electric field is employed to induce strain in suspended GaAs structures, where a bidirectional spectral shift of the embedded quantum dots is observed. It is suggested that the spatial distribution of strain can be engineered by designing the sample geometry, which could have potential applications in quantum photonics.

The second part of the thesis concerns the exciton Mott transition, which is a phase transition occurring in a population of interacting electrons and holes, in which insulating excitons are ionized to a metallic phase of free carriers. It is still debated in the literature whether the Mott transition in quantum wells occurs gradually or abruptly as a function of the governing parameters — exciton density and temperature. In this work, the Mott transition is studied with indirect excitons with electrically extended radiative lifetime and is found to occur gradually as a function of exciton density and temperature. The exciton-density-temperature phase diagram of the transition exposes two regions with exciton-dominant and plasma-dominant populations that are separated by a linear boundary.

Resumé

Denne afhandling indeholder undersøgelsen af exciton Mott overgangen i koblede kvante brønde, fabrikation af fotoniske-krystal strukturer med indlejrede selv-samlede kvantepunkter og kontol af deres egenskaber ved hjælp af et eksternt elektrisk felt.

I den første del af afhandlingen er fokusset på kvantepunkter i fotoniske nanostrukturer. Fremstillingsprocessen af høj kvalitets reproducerbare fotoniske-krystal strukturer i prøver med elektriske kontakter bliver præsenteret. Denne process bliver anvendt til at undersøge lokalisering af lys i korte fotoniske-krystal bølgeleder med en dispersions relation der muliggør en langsomt lys effekt. Effekten af variationer i den lokale tæthed af optiske tilstande på elektrisk kontrollerede kvantepunkter indlejeret i fotoniske strukturer bliver undersøgt. Et elektrisk felt bliver anvendt til at inducerer tøjning i fritstående GaAs strukturer, hvor et bidirektionalt spektralt skift af de indlejrede kvantepunkter er observeret. Det bliver antydet at den rummelige distribution af tøjningen kan blive manipuleret ved at designe prøvens geometri, hvilket potentielt kan finde anvendelse i kvante fotonik.

Den anden del af afhandlingen omhandler exciton Mott overgangen, hvilket er en fase overgang der finder sted i en bestand af vekselvirkende elektroner og huller, hvori isolerende excitoner bliver ioniseret til en metallisk fase tilstand af frie ladningsbærere. I litteraturen debatteres det stadigt hvorvidt Mott overgangen i kvantebrønde sker glidende eller abrubt som en funktion af de styrende parametre — exciton tæthed og temperatur. I dette arbejde, bliver Mott overgangen studeret med indirekte excitoner med elektriske forlænget radiativ levetid og det ses at overgangen sker gradvist som en funktion af exciton tæthed og temperatur. Exciton-tætheds-temperatur fasediagrammet af overgangen blotlægger to regioner med exciton domineret og plasma domineret besætninger der separeret af en linear grænse.

List of publications

The work performed during this Ph.D.-project has resulted in the following publications:

Journal publications

1. L. Midolo, T. Pregnolato, G. Kiršanskė, and S. Stobbe, "Soft-mask fabrication of gallium arsenide nanomembranes for integrated quantum photonics", Nanotechnology **26**, 484002 (2015).

2. I. Söllner, S. Mahmoodian, S. Lindskov Hansen, L. Midolo, A. Javadi, G. Kiršanskė, T. Pregnolato, H. El-Ella, E. H. Lee, J. D. Song, S. Stobbe, and P. Lodahl, "Deterministic photon-emitter coupling in chiral photonic circuits", Nat. Nanotechnol. **10**, 775–778 (2015).

3. A. Javadi, I. Söllner, M. Arcari, S. Lindskov Hansen, L. Midolo, S. Mahmoodian, G. Kiršanskė, T. Pregnolato, E. H. Lee, J. D. Song, S. Stobbe, and P. Lodahl, "Single-photon non-linear optics with a quantum dot in a waveguide", Nat. Commun. **6**, 8655 (2015).

Journal publications in preparation

1. G. Kiršanskė, P. Tighineanu, R. S. Daveau, J. Miguel-Sánchez, P. Lodahl, and S. Stobbe, "Dynamics of the exciton Mott transition in the photoluminescence of coupled quantum wells", to be submitted.

2. M. Arcari, L. Midolo, M. Matthiae, T. Pregnolato, G. Kiršanskė, S. Mahmoodian, E. H. Lee, J. D. Song, S. Stobbe, and P. Lodahl, "Efficiency and coherence of a photonic-crystal waveguide single-photon source", to be submitted.

List of abbreviations

BEC	Bose-Einstein condensate
BCS	Bardeen-Cooper-Schrieffer
CB	Conduction band
CPD	Critical point dryer
CQWs	Coupled quantum wells
DES	Density of electronic states
DOS	Density of optical states
DXs	Direct excitons
EH-plasma	Electron-hole plasma
ICP	Inductively coupled plasma
IXs	Indirect excitons
LCC	Leadless chip carrier
LDOS	Local density of optical states
PhC	Photonic crystal
QDs	Quantum dots
QWs	Quantum wells
RIE	Reactive ion etching
RTA	Rapid thermal annealing
SEM	Scanning electron microscope
TE	Transverse electric
TM	Transverse magnetic
VB	Valence band

Contents

Preface i

Abstract iii

Resumé v

List of publications vii

List of abbreviations ix

Introduction 1

1 Foundations of quantum photonics in group III-V semiconductors 5
- 1.1 Band diagram of GaAs . . . 6
- 1.2 Effect of quantum confinement . . . 7
  - 1.2.1 Quantum wells . . . 8
  - 1.2.2 Self-assembled quantum dots . . . 10
- 1.3 Photonic-crystal nanostructures . . . 13
- 1.4 Electric field on quantum-confined structures . . . 15

2 Fabrication of nanophotonic devices 17
- 2.1 Lithography . . . 18
  - 2.1.1 UV lithography . . . 19
  - 2.1.2 Electron-beam lithography . . . 20
- 2.2 Etching . . . 21
  - 2.2.1 Inductively coupled plasma etching . . . 21
  - 2.2.2 Wet chemical etching . . . 24
- 2.3 Ohmic electrical contacts . . . 26
- 2.4 Experimental setup . . . 30
- 2.5 Effects of fabrication imperfections in a glide-plane ring cavity . . . 33
- 2.6 Other experiments on the fabricated nanostructures . . . 36
- 2.7 Conclusions . . . 38

3 Electrical tuning of quantum dots across the photonic band edge 39
3.1 Quantum-confined Stark effect on quantum dots . . . 41
3.2 Quantum dots tuned in a photonic-crystal waveguide . . . 45
3.3 Light localization in short photonic-crystal waveguides . . . 48
3.4 Conclusions . . . 53

4 Control of quantum-dot photoluminescence via electroelastic fields 55
4.1 Introduction to the theory of continuum elasticity . . . 56
  4.1.1 Stress and strain relation . . . 56
  4.1.2 Deformation potentials and Pikus-Bir Hamiltonian . . . 58
4.2 Fabrication of a suspended GaAs bridge sample . . . 60
  4.2.1 Sample preparation . . . 60
  4.2.2 Piezoelectric crystal (PMN-PT) . . . 62
4.3 Strain tuning of quantum dots in suspended GaAs bridges . . . 63
  4.3.1 Experimental conditions . . . 63
  4.3.2 Photoluminescence of the wetting layer . . . 64
  4.3.3 Photoluminescence of quantum dots . . . 65
4.4 Spatial map of the strain-induced band-gap shift . . . 67
4.5 Outlook: Enhancement of the exciton energy shift in a suspended bridge geometry 71
4.6 Conclusions . . . 73

5 The exciton Mott transition in coupled quantum wells 75
5.1 Indirect excitons in GaAs-based heterostructures . . . 76
  5.1.1 Lifetime of indirect excitons . . . 78
  5.1.2 Thermalization rate . . . 78
  5.1.3 Static electric dipole moment . . . 78
5.2 Photoluminescence spectroscopy on coupled quantum wells . . . 79
  5.2.1 Time-integrated photoluminescence spectra . . . 81
  5.2.2 Decay dynamics . . . 84
5.3 The exciton Mott transition . . . 87
  5.3.1 Phenomena in cold exciton gases . . . 88
  5.3.2 The Mott transition of indirect excitons . . . 89
  5.3.3 Effective exciton density . . . 93
  5.3.4 Phase diagram . . . 95
  5.3.5 Ruling out of alternative mechanisms . . . 98
5.4 The role of dark excitons . . . 99
5.5 Conclusions . . . 100

Appendices 102

A Fabrication of photonic-crystal membranes 105

B Electrical sample mount **111**

Bibliography **115**

Introduction

Semiconductor physics is a thriving area of scientific interest celebrated with four outstanding achievements awarded the Nobel prize in physics over the past 15 years. The advance of semiconductor technology and research in electronics accelerated with the invention of heterostructures [1, 2]. Optics has successfully adopted the novelties yielding the development of semiconductor light sources and detectors. Now, the field of optoelectronics is where high expectations are directed for the next breakthrough allowing to surpass the limitations of silicon-based computing. A common goal driving this field is the realization of a new computational technology based on quantum systems [3].

A scheme of linear-optics quantum computing has been proposed requiring sources that emit single photons on demand [4]. A particularly promising realization of a semiconductor nanostructure, the self-assembled quantum dot, has been employed to develop the single-photon sources. Three-dimensional quantum confinement of charge carriers in a quantum dot results in an atomic-like spectrum of narrow peaks associated with discrete electronic transitions. The solid-state nature of the quantum dot is a blessing and a curse at the same time. The disadvantages of such a platform stem from the unavoidable quantum dot coupling to its environment, which leads to decoherence of the emitted photons. Fortunately, with assistance from semiconductor technology it has become possible to evade these effects [5]. By embedding the quantum dot into an engineered electromagnetic environment, e.g., a photonic crystal, its optical properties can be vastly tuned allowing for on-demand emission of single quanta of light. The emergence of photonic crystals interfaced with quantum dots has been driving research towards the implementation of scalable photonic circuits for quantum computation [6]. Additionally, it is a useful tool for investigating extraordinary quantum optics effects such as fractional emitter decay [7].

Aside from technological applications, semiconductors are great laboratories for investigating fundamental many-body interactions. Of particular interest is a system of photoexcited electron-hole pairs or excitons, where the Coulomb interaction leads to the formation of different phases such as the exciton gas, electron-hole plasma, Bose-Einstein and Bardeen-Cooper-Schrieffer-like condensates. Transitions between these phases have attracted intense attention in fundamental research [8–10]. The exciton Mott transition is among the most intriguing phenomena, since its exact nature is still a topic of a long-standing debate. It is associated with the critical particle density above which excitons are ionized into the electron-hole plasma [11]. In practice, to achieve such densities of particles in thermal equilibrium, long-lived excitons are required. Conventional semiconductor technology allows harnessing low-dimensional nanostructures to obtain such properties. Coupled quantum wells support the formation of an indirect exciton that straddles the potential barrier between two quantum wells. Due to a reduced wavefunction overlap between the electron and the hole residing in the adjacent wells, the lifetime of the indirect excitons is greatly extended. Owing to their superior properties, indirect excitons are an excellent test bed for studying collective quantum effects.

In this work, we employ an electric field to manipulate excitons in quantum dots and coupled quantum wells. The first part of this work is focused on the search of subtle quantum effects predicted to occur when the emitter is tuned across the photonic band edge. Processes of reproducible photonic-crystal and electrical-contact fabrication enable the required experimental environment to be achieved. In the second part, the boundary of the Mott transition in indirect excitons electrically tuned to have long lifetimes is investigated.

This thesis is organized as follows. In Chapter 1, the key concepts of quantum photonics based on group III-V semiconductors are presented. First, the main electronic and optical properties of GaAs, a representative III-V semiconductor, are reviewed. Quantum confinement in semiconductors is discussed, with a particular focus on quantum dots and quantum wells, followed by an introduction to photonic crystals as a tailored environment for quantum dots. The effect of the electric field in semiconductors is briefly reviewed.

In Chapter 2, fabrication methods for realizing diverse photonic-crystal nanostructures are discussed. Particular emphasis is put on the additional fabrication steps developed during this work. The obtained practical knowledge on the formation of ohmic contacts to GaAs is summarized. Light localization, occurring in photonic structures due to a finite fabrication disorder, is investigated in photonic-crystal ring cavities. Finally, the main achievements of some experiments carried out in the group on the fabricated samples are highlighted.

Chapter 3 deals with quantum dots near the photonic band edge. The quantum-confined Stark effect on quantum dots is employed to search for unexplored quantum optics phenomena such as fractional decay. The light localization around the cutoff frequencies seems to put the experimental realization of such effects in doubt.

Chapter 4 is concerned with the strain-induced quantum-dot tuning in a simple nanostructure, which is the first attempt to combine conventional photonic-crystal fabrication and wafer transfer via a gold layer to produce strain-tunable suspended membranes. First, the main concepts of the theory of continuum elasticity are introduced. The results of the photoluminescence measurements on the quantum dots embedded into a suspended structure under the compressive biaxial stress are discussed. The sample geometry is found to strongly influence the induced strain.

Finally, in Chapter 5, the exciton Mott transition observed in photoluminescence of coupled quantum wells is discussed. The initial characterization of the sample is reviewed providing insight into the main properties of the indirect excitons such as the long and electrically-tunable lifetime. Next, the phase diagram of cold exciton gases is discussed with a particular emphasis on the two cases, i.e., the insulating exciton gas and the metallic electron-hole plasma. The investigation of the boundary between these two phases is the main subject of this chapter. The phase diagram of the Mott transition observed for the indirect excitons is presented. The transition is observed with temperature and exciton density, and occurs gradually as revealed from the photoluminescence data. Finally, a peculiar photoluminescence quenching observed at a certain band alignment is presented. Although lacking a deep understanding of this effect, it is speculated that it might be related to dark excitons.

In Appendix A, detailed recipes for the sample fabrication are provided. Appendix B contains the description of a custom-made sample holder designed to accommodate samples with electrical contacts.

Chapter 1

Foundations of quantum photonics in group III-V semiconductors

This chapter builds a theoretical background for discussions throughout this thesis. First, a material platform used in this work — group III-V semiconductors — is considered. Compounds formed between elements of group III and group V of the periodic table, such as GaAs, InAs, GaN, AlN, InSb, InP, etc., have provided a solid base for a broad range of applications in optoelectronics and nanophotonics research [12–14]. Many of the III-V semiconductors possess a direct band gap, which is a desired property for making light emitters or absorbers. Controlled combination of elemental semiconductors allows band gap engineering, which is a powerful tool for designing such semiconductor devices. Together with reduced dimensionality this technique has yielded quantum-confined heterostructures such as quantum wells (QWs) and quantum dots (QDs), the emitters studied in this work. Many of the physical effects in QWs are present even at room temperature, which has enabled the implementation of QW-based devices, e.g., lasers, infrared photodetectors, electro-optic modulators and solar cells [13, 15]. On the other hand, QWs form an excellent platform for studying exciton physics [16–18]. Exciton formation and optical properties of the QWs are described in this chapter. Three-dimensional (3D) quantum-confinement in a semiconductor leads to the formation of QDs possessing atom-like properties. In particular, QDs can emit single photons by the radiative transitions between the discrete energy levels of charge carriers. In this chapter, the growth, structure and main properties of InAs/GaAs QDs are reviewed. QDs can be incorporated into a tailored solid-state environment based on photonic crystals (PhCs). PhC nanostructures have a great influence on the radiative properties of the QD and can be employed in building deterministic single-photon sources. The working principle of PhC-based devices is introduced in this chapter. Finally, since some of the PhC devices discussed in this thesis are embedded in a diode structure, the effect of the electric field on excitons in quantum-confined systems is briefly described. The concepts of QWs and QDs along with the description of PhC operation compose a common theoretical basis for the rest of the thesis, whereas some particular theory aspects are presented within the relevant chapters.

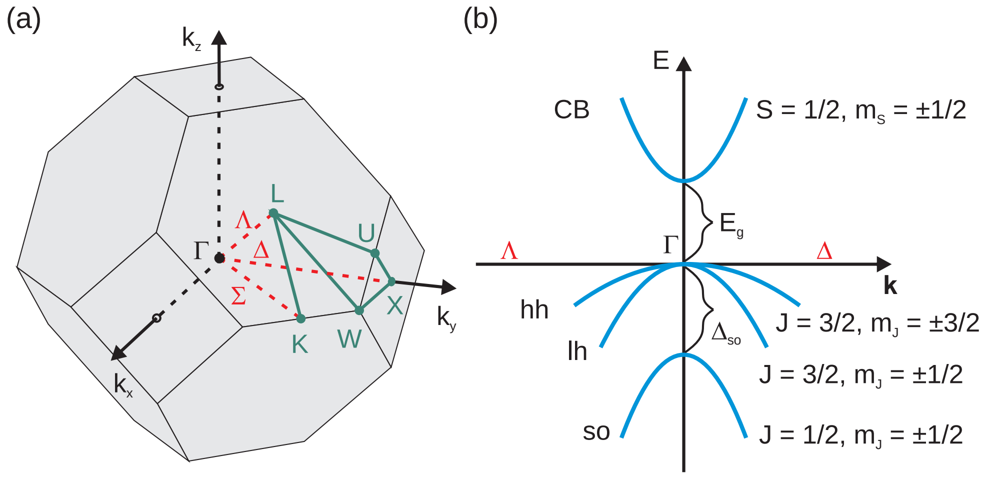

Figure 1.1: (a) First Brillouin zone of a semiconductor with a zinc blende crystal structure. Important directions, high symmetry points, and the center of the Brillouin zone are indicated. (b) Sketch of the band structure of GaAs close the Γ point along the directions Λ and Δ. The energy-momentum dispersion relation is approximately parabolic for $\mathbf{k} \approx 0$.

1.1 Band diagram of GaAs

Material parameters and properties of group III-V semiconductors share many common aspects. In the following, the discussed properties are of GaAs, nevertheless, they hold for related compounds as well.

The electronic energy band structure describes the energy dispersion in the momentum space for electrons and holes. This concept is essential to understand the electronic and optical properties of semiconductors. The band dispersion is determined by the crystal structure of a solid. GaAs, along with many other III-V semiconductors, has a zinc blende (sphalerite) crystal structure, which is a face-centered cubic (FCC) lattice with two atoms in the base, a Ga atom at (0,0,0) and an As atom at $(a_0)\left(\frac{1}{4},\frac{1}{4},\frac{1}{4}\right)$, where a_0 is the lattice constant. The first Brillouin zone of GaAs, with important directions and symmetry points, is shown in Fig. 1.1(a). Γ denotes the origin of k-space, X, K, and L are the intersection points of the Brillouin-zone boundary with the [100], [110], and [111] directions, which are represented by the symbols Δ, Σ, and Λ, respectively. A simplified sketch of the band diagram of GaAs near the Γ point is shown in Fig. 1.1(b). For GaAs the energetic maximum of the valence band (VB) and the minimum of the conduction band (CB) occurs at the center of the Brillouin zone, which results in a direct band gap denoted by E_g. This property indicates that the transition from the bottom of CB to the top of VB does not require a change in momentum and is accompanied by an emission of a photon. The CB possesses s-orbital symmetry and has a spin S = 1/2 with projections along the quantization axis $m_S = \pm 1/2$. The VB consists of three subbands with p-orbital symmetry. The upper two subbands, termed as heavy-hole (hh) and light-hole (lh) bands, are degenerate, whereas the third subband, the split-off (so) band, is energetically well separated from the top of the VB owing to the spin-orbit coupling energy Δ_{SO},

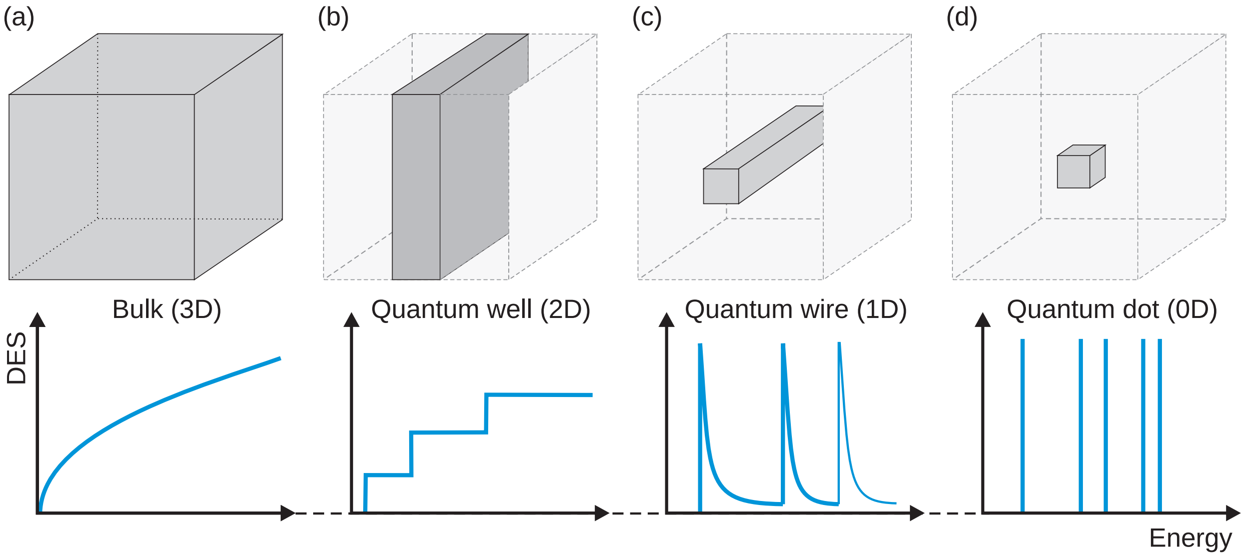

Figure 1.2: Effect of quantum confinement on the density of electronic states. The upper panel illustrates bulk (a) semiconductor and heterostructures confined in 1 (b), 2 (c), and 3 (d) dimensions. The corresponding sketches of DES are shown in the lower panel.

which is 0.34 eV for GaAs [19], and therefore, plays a minor role in optical experiments. Both lh and hh have a total angular momentum J = 3/2 and projections $\mathrm{m_J} = \pm 1/2$ and $\pm 3/2$, respectively. The split-off band has J = 1/2 and its projections $\mathrm{m_J} = \pm 1/2$. The lh and hh subbands split going away from the Γ point ($\mathbf{k} \neq 0$) due to a different curvature of the dispersion curve. This curvature defines an effective mass as $m_{\mathrm{eff}} = \hbar^2 \left(\frac{\mathrm{d}^2 E}{\mathrm{d}k^2}\right)^{-1}$. The VB subbands with smaller and larger curvature have respectively higher and lower effective masses for holes, thus the terms heavy and light hole.

In general, the energy dispersion in k-space deviates from a parabolic curve and is anisotropic depending on the direction and the amplitude of **k**. Additionally, strain effects and quantum-confinement might result in lifting the VB degeneracy at the Γ point, as discussed in Chapter 4. In many cases for semiconductor heterostructures, the properties of the VB extremum are dominated by the heavy holes since a larger m_{eff} results in a larger density of available states, as discussed in the following.

1.2 Effect of quantum confinement

As mentioned in the introduction of this chapter, a combination of two semiconductors with unequal band gap energies allows to produce a new material with a band gap different from that of the constituents. Additionally, several layers of different semiconductors can be grown in an alternating sequence resulting in a potential profile for the electrons and holes due to the band offsets. Particularly, if a lower band-gap semiconductor is sandwiched between two layers with a higher band-gap energy, the charge carriers are restricted to move only in that layer. Layer thickness on the order of the de Broglie wavelength of the charge carriers (a few nanometers) results in the quantum confinement along the growth direction. Such a structure is known as a quantum well. Conventional growth techniques also allow to create heterostructures confined in two and all three dimensions, producing quantum wires and quantum dots, respectively. The full ensemble of quantum-confined heterostructures is show in the upper panel of Fig. 1.2.

The density of electronic states (DES), defined as the number of available states per unit volume within an energy interval, is significantly modified by a reduced dimensionality. It is a key parameter, which defines the properties of optical emitters. For different degrees of semiconductor confinement, DES can be evaluated as follows:

$$g_{3\mathrm{D}}(E) = \frac{m_{\mathrm{eff}}}{\pi^2\hbar^3}\sqrt{2m_{\mathrm{eff}}(E-E_0)}, \tag{1.1a}$$

$$g_{2\mathrm{D}}(E) = \frac{m_{\mathrm{eff}}}{\pi\hbar^2}, \tag{1.1b}$$

$$g_{1\mathrm{D}}(E) = \frac{1}{\pi\hbar}\sqrt{\frac{2m_{\mathrm{eff}}}{E-E_0}}, \tag{1.1c}$$

$$g_{0\mathrm{D}}(E) = 2\delta(E-E_0). \tag{1.1d}$$

In a non-confined case (bulk semiconductor), DES is non-zero for energies above E_0 and varies proportional to $\sqrt{E-E_0}$, see the lower panel of Fig. 1.2(a). The confinement along a single direction results in a step-like behavior of DES (Fig. 1.2(b)). For a quantum wire, DES peaks for each quantized state and follows the $(E-E_0)^{-1/2}$ dependence in-between the resonances (Fig. 1.2(c)). In the case of an ultimate confinement (QD), the charge carrier energy states are discrete and DES is composed of Dirac-delta functions for each state (Fig. 1.2(d)). Such DES translates into a discrete emission spectrum of a QD. In this thesis, we focus on two types of confined heterostructures, namely QWs and QDs, which are discussed in more detail below.

1.2.1 Quantum wells

QWs impart a number of properties on excitons, thus this concept is discussed first. In semiconductors, an electron and a hole interact via the Coulomb force, which can be quantified by an attractive Coulomb potential term $-e^2/(4\pi\epsilon_0\epsilon|\mathbf{r}_e-\mathbf{r}_h|)$, similar as in the hydrogen-atom problem in quantum mechanics. Here ϵ_0 is the vacuum permittivity, ϵ is the relative permittivity of the material, and $|\mathbf{r}_e-\mathbf{r}_h|$ is the distance between the electron and the hole. Weakly bound excitons, known as Wannier excitons, can form in semiconductors with a relatively high permittivity ϵ [20]. In a 3D case, solving a hydrogen-atom problem using the effective mass approximation, allows to find the energy of an exciton:

$$E_n^{3\mathrm{D}} = E_g - \frac{\mu}{2}\left(\frac{e^2}{4\pi\epsilon_0\epsilon}\right)^2\frac{1}{(\hbar n)^2}, \tag{1.2}$$

where E_g is a band-gap energy of a material, $\mu = m_e m_h/(m_e+m_h)$ is the reduced mass of the exciton, and $n = 1,2,3,..$ is the principal quantum number.

A QW can be modelled as a quasi-two dimensional (quasi-2D) system, since the energy levels in the growth (z-) direction are discrete due to quantum-confinement, as shown in Fig. 1.3. Similarly to the case of a 2D hydrogen atom, the bound state energy of a 2D exciton can be obtained:

$$E_n^{2\mathrm{D}} = E_g - \frac{\mu}{2}\left(\frac{e^2}{4\pi\epsilon_0\epsilon}\right)^2\frac{1}{\hbar^2(n-1/2)^2}. \tag{1.3}$$

The second term in Eqs. (1.2) and (1.3) for $n = 1$ is equal to the binding energy E_b of the exciton. It is four times larger in the ideal 2D case than in 3D, where the exciton is spread over many lattice sites. A 2D exciton is confined in a QW resulting in a larger overlap of the carrier wavefunctions, which enhances optical effects as compared to excitons in bulk.

It seems reasonable to say that the exciton binding energy is largest when the spatial distance between the electron and hole is minimal. This situation corresponds to a complete overlap. In an ideal QW structure, i.e., an infinite square well, the exciton wavefunctions are fully confined. However, a real QW structure has finite barriers, leading to a finite-QW problem. Such a structure is of a quasi-2D nature with the exciton wavefunction penetrating into the barriers. For narrow QWs, where the well width is comparable to or smaller than the exciton radius in bulk GaAs (~ 10 nm), the confined energy levels are lifted closer to the barrier height, which makes the wavefunctions penetrate more into the barrier regions. This reduces the confinement of the wavefunctions within the well, and thus the binding energy. Tuning the barrier height allows to change the binding energy and the wavefunction overlap of excitons in a QW. In this way, the optical properties of a QW can be conveniently manipulated.

In QWs the optical transitions take place between the z-confined electronic states according to dipole selection rules. The transition rate can be calculated from Fermi's golden rule [15]:

$$\gamma_{if} = \frac{2\pi}{\hbar} |\langle f|e\mathbf{r}\cdot\mathbf{E}|i\rangle|^2 \rho(E_i - E_f + \hbar\omega), \tag{1.4}$$

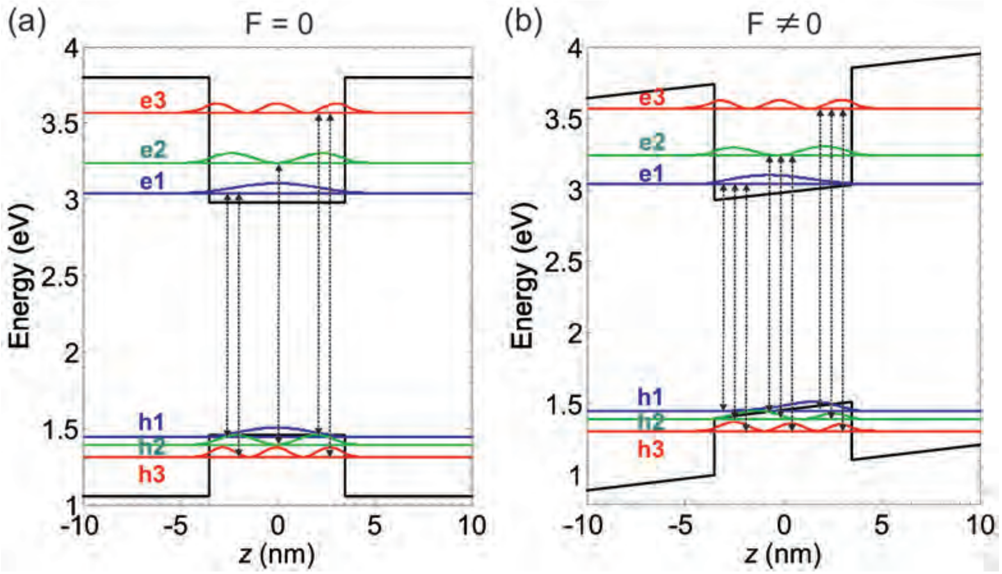

Figure 1.3: The band diagram of a finite QW. Here three eigenenergy levels and density probability are shown for the electrons (e1, e2, e3) and the holes (h1, h2, h3). In the flat band case (a), the optical transitions are allowed to occur between the states of equal parity as shown by the dotted arrows. The applied electric field breaks the symmetry of the wavefunctions, therefore, the parity is no longer well-defined, and the transitions between the opposite parity states become allowed (b).

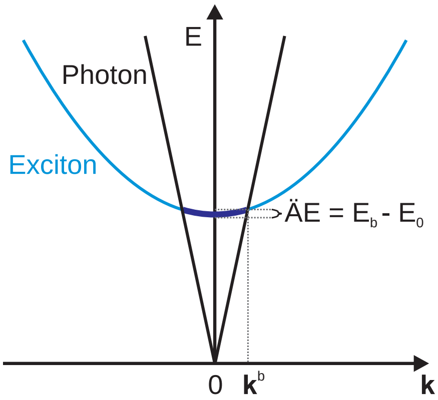

Figure 1.4: Energy-momentum dispersion relation of the exciton and the emitted photon. Only the excitons within the indicated energy interval ΔE (highlighted by the dark blue line) fulfill the in-plane momentum conservation and can contribute to the photon emission.

which defines the probability for the optical transition between the initial confined state $|i\rangle$ with energy E_i and the final confined state $|f\rangle$ with energy E_f. Here $e\mathbf{r}$ is the dipole operator, $\mathbf{E}$ is the light electric field, $\rho(E_i - E_f + \hbar\omega)$ is the 2D density of states, and $\hbar\omega$ is the photon energy.

In an infinite QW at zero electric field, the overlap integral in Eq. (1.4) is zero between the states of different quantum numbers and that gives a selection rule $\Delta n = 0$ for optical transitions. In real QWs, owing to different effective mass of an electron and a hole, the evanescent wavefunction tail into the barriers can be different such that the carrier wavefunctions are not necessarily orthogonal. This results in small departures from the selection rule of an infinite well allowing usually weak transitions for $\Delta n \neq 0$. Nevertheless, transitions between the opposite parity states ($\Delta n =$ odd number) are always forbidden since the overlap integral between them is zero. Breaking the inversion symmetry of the confining potential in a z-dimension results in an undefined parity of the wavefunctions, and thus the previously forbidden transitions become allowed.

Since excitons in a QW are free to move in the xy-plane, they can acquire an arbitrary in-plane momentum, which gives rise to the energy dispersion of excitons. For the radiative exciton recombination to take place, not only the exciton energy, but also the in-plane momentum must be conserved. Only excitons within the light cone defined by the photon dispersion fulfill these requirements and can contribute to photoluminescence. Figure 1.4 illustrates the exciton and the photon dispersion relations, where the momentum distribution of optically active excitons is highlighted by the dark blue line. The excitons with the energy (in-plane momentum) larger than E_b (k^b) are momentum dark and do not contribute to photoemission, but they play a role in many-particle effects, as discussed in Chapter 5.

1.2.2 Self-assembled quantum dots

A practical example of a semiconductor structure confined in all three dimensions is a self-assembled QD. In this work, QDs are used that form during InAs/GaAs growth by molecular-beam epitaxy in the Stranski-Krastanov mode. A QD is a nanometer-sized island of InAs (on the order of

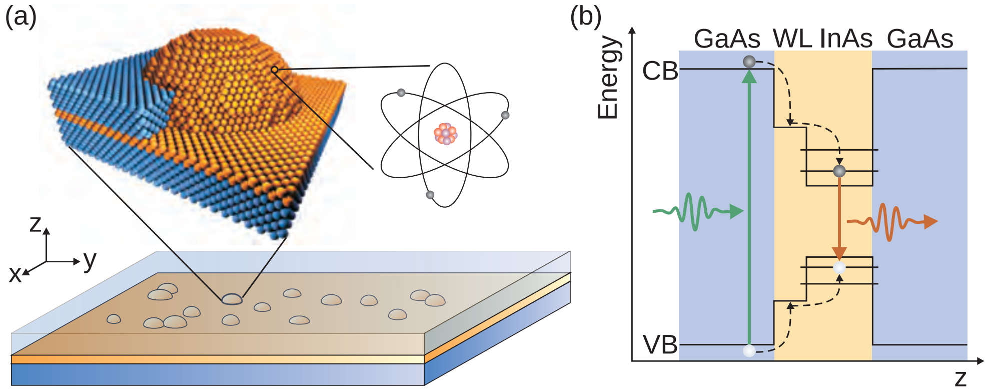

Figure 1.5: Structure and energy diagram of a self-assembled InAs/GaAs QD. (a) Sketch of a single QD formed at the interface between GaAs (blue) and InAs (orange) layers, referred to as the wetting layer (WL). Illustration from Ref. [21]. QDs are formed at random positions on the wetting layer and generally vary in size, as illustrated in the lower sketch. (b) Band structure of a single QD, where a typical optical experiment scheme is shown: a photon with the energy close to the band gap of GaAs is absorbed exciting a pair of energetic charge carriers, which relax to the ground state of an exciton in the QD and recombine via the emission of a single photon.

10^5 atoms) formed on a few atomic layers of InAs (wetting layer, WL) grown on a GaAs substrate. Sketch of a single InAs/GaAs QD is shown in Fig. 1.5(a). The QD formation is driven by the relaxation of strain due to a crystal lattice mismatch between InAs and GaAs and is a random process resulting in a spatial and size distribution of an ensemble of QDs. Typically a distribution of QDs with varying height (3–5 nm) and lateral extent (15–30 nm) is obtained [22]. The small size and the mismatch between the band gap energies of InAs (0.42 eV at 0 K) and GaAs (1.52 eV at 0 K) creates a 3D confinement potential for both the electrons and holes, as illustrated by the energy structure of a single QD in Fig. 1.5(b). In a typical photoluminescence experiment, an electron-hole pair is created via photon absorption above the GaAs band gap. The charge carriers relax via nonradiative processes to the QD potential and forms an exciton, which is annihilated by a single-photon emission. The photoluminescence spectrum of a QD contains a sharp peak and resembles atomic spectra. Therefore QDs are popularly referred to as artificial atoms.

Self-assembled QDs can be modelled as a five-level system reflecting the fine structure of the ground-state exciton, see Fig. 1.6(a). The ground state exciton is composed of an electron with spin $\mathrm{S} = 1/2$ and projections $\mathrm{m_S} = \pm 1/2$ and a heavy hole with a total angular momentum $\mathrm{J} = \pm 3/2$ and projections $\mathrm{m_J} = \pm 3/2$. The light hole is energetically separated due to strain effects during the QD growth and is thus neglected. The neutral exciton can have the total angular momentum projection $\mathrm{M} = \pm 1, \pm 2$, where the states with $\mathrm{M} = \pm 1$ are optically bright ($|X_b\rangle$ and $|Y_b\rangle$), and the states with $\mathrm{M} = \pm 2$ are optically inactive ($|X_d\rangle$ and $|Y_d\rangle$).[1] If the QD is circularly symmetric its two orthogonal dipoles represented as X and Y are circularly polarized. Additionally, the bright and dark states are energy-split by a few hundred µeV owing to the exchange interaction of electrons

---

[1] A photon carries an angular momentum ±1 and the total angular momentum is conserved only for the bright states.

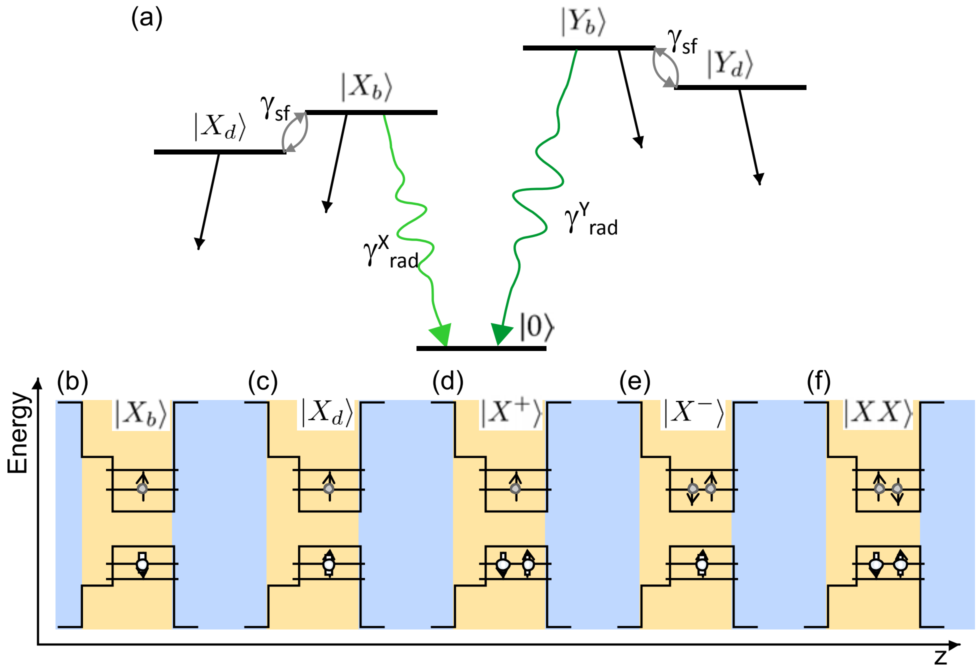

Figure 1.6: (a) Level scheme of a QD, where the two bright states $|X_b\rangle$ and $|Y_b\rangle$ are split in energy due to the exchange interaction. Each bright state couples to the respective dark state $|X_d\rangle$ and $|Y_d\rangle$ through spin-flip processes with the rate γ_{sf}. The bright states $|X_b\rangle$ and $|Y_b\rangle$ can decay radiative to the ground state $|0\rangle$ with the respective rates $\gamma_{\mathrm{rad}}^{\mathrm{X}}$ and $\gamma_{\mathrm{rad}}^{\mathrm{Y}}$. Nonradiative relaxation indicated by the black arrows is possible from all four levels. (b)-(f) Excitonic complexes in a QD: the bright exciton $|X_b\rangle$, the dark exciton $|X_d\rangle$, the positively charged exciton $|X^+\rangle$, the negatively charged exciton $|X^-\rangle$, and the biexciton $|XX\rangle$.

and holes [23]. The exchange interaction is also responsible for lifting the degeneracy of the dark states. Realistic QDs have no rotational symmetry, therefore, the exchange interaction gives rise to the fine structure splitting of the bright states $|X_b\rangle$ and $|Y_b\rangle$ by a few tens of µeV [23]. Bright and dark states are coupled via spin-flip processes with a rate γ_{sf}. The bright states decay with radiative and nonradiative processes, while the dark states only decay nonradiatively.

In a homogeneous medium, the two radiative transitions occur at similar decay rates, therefore, the five-level scheme can be reduced to the scheme of only three levels: $|X_b\rangle$, $|X_d\rangle$, and $|0\rangle$. A biexponential model is used to describe the spontaneous emission of a neutral exciton: $N(t) = A_{\mathrm{f}}\mathrm{e}^{-\gamma_{\mathrm{f}}t} + A_{\mathrm{s}}\mathrm{e}^{-\gamma_{\mathrm{s}}t}$, where A_{f} (A_{s}) is the amplitude and γ_{f} (γ_{s}) is the decay rate of the fast (slow) component, respectively. It is obtained by solving the rate equations describing the temporal evolution of the bright and dark state population probabilities [24]. Since the spin-flip rates have been measured to be slow, the fast (slow) decay rate is mainly given by the decay rate of the bright (dark) state $\gamma_{\mathrm{f}} = \gamma_{\mathrm{rad}} + \gamma_{\mathrm{nrad}}$ ($\gamma_{\mathrm{s}} = \gamma_{\mathrm{nrad}}$), where γ_{rad} and γ_{nrad} are the radiative and nonradiative decay rates, respectively [24, 25].

Other charge configurations are possible in the lowest energy state of a QD, as illustrated in Fig. 1.6(b)–(f). Apart from the already discussed neutral exciton in bright and dark spin configuration, the QD potential can trap an additional hole or electron forming a positively or a negatively charged exciton (trion $|X^{+}\rangle$ or $|X^{-}\rangle$), respectively. Pauli filling of the lowest single-particle energy levels with two electrons and two holes results in the creation of the biexciton ($|XX\rangle$). The biexciton decays to one of the neutral-exciton states via emission of a single photon.

Probing the temporal dynamics of a QD via time-resolved photoluminescence spectroscopy allows to experimentally determine the decay rates γ_{rad} and γ_{nrad}. By employing these quantities, QD efficiency to emit a single photon for each excitation event is defined as $\eta_{\mathrm{QE}} = \frac{\gamma_{\mathrm{rad}}^{\mathrm{hom}}}{\gamma_{\mathrm{rad}}^{\mathrm{hom}}+\gamma_{\mathrm{nrad}}}$, where $\gamma_{\mathrm{rad}}^{\mathrm{hom}}$ assumes a radiative decay rate into a homogeneous medium. QD can be embedded in an inhomogeneous medium, e.g., photonic crystals, which can strongly modify the optical properties of the QD. This is the subject of the following section.

1.3 Photonic-crystal nanostructures

In order to describe the dynamics of the emitter in a tailored dielectric environment, quantum theory of light-matter interaction is employed [26]. The quantum emitter is assumed to be a dipole, i.e., its spatial extent is smaller than the wavelength of light. This approximation is known as the dipole approximation and is valid for the QDs described in this thesis. The main result of this treatment is the radiative decay rate of a QD expressed as:

$$\gamma_{\mathrm{rad}}(\mathbf{r_0}, \omega_0, \hat{\mathbf{n}}_{\mathrm{p}}) = \frac{\pi\omega_0}{\hbar\epsilon_0}|\mathbf{p}|^2\rho(\mathbf{r_0}, \omega_0, \hat{\mathbf{n}}_{\mathrm{p}}), \tag{1.5}$$

where $|\mathbf{p}|$ is the magnitude of the dipole moment[2] and $\rho(\mathbf{r_0}, \omega_0, \hat{\mathbf{n}}_{\mathrm{p}})$ is the local density of optical states (LDOS) [6]. $\rho(\mathbf{r_0}, \omega_0, \hat{\mathbf{n}}_{\mathrm{p}})$ defines the number of optical modes per unit volume and energy at a given emitter position $\mathbf{r_0}$ and frequency ω_0, and provides all information about the electromagnetic environment of the emitter.

Conventional semiconductor processing technology allows to sophisticatedly modify the optical environment of QDs. The state-of-the-art structures for this purpose are called photonic crystals (PhC), first proposed more than forty years ago [27–29]. A detailed review on this topic can be found in Ref. [30]. A PhC is a periodic alternation of low- and high-refractive index materials with a periodicity on the order of the wavelength of light. Unlike in a homogeneous medium, where optical modes of all frequencies are allowed, in a PhC a photonic band gap, where certain-frequency modes are forbidden to propagate, opens up. This is due to the periodic structure of the crystal, in analogy with the electronic band gap in semiconductors. Ideally, a periodic modulation in all three dimensions is desired, where a full photonic band gap is opened and the light propagation can be suppressed in any direction. However, it is a substantial technological challenge to produce such 3D PhCs in practice, therefore, 2D photonic structures are usually implemented. An example of such a 2D PhC slab is shown in Fig. 1.7(a), where air holes with a radius r arranged in a triangular lattice with a constant a are perforated onto a GaAs membrane. The size and the central frequency of the photonic band gap can be adjusted by a proper choice of r and a. In a PhC slab, light is not confined by the LDOS effect in the direction perpendicular to the slab plane, but is strongly reflected by

---

[2] The dipole moment has been decomposed into $\mathbf{p} = |\mathbf{p}|\hat{\mathbf{n}}_{\mathrm{p}}$, where $\hat{\mathbf{n}}_{\mathrm{p}}$ is the unit vector in the direction of $\mathbf{p}$.

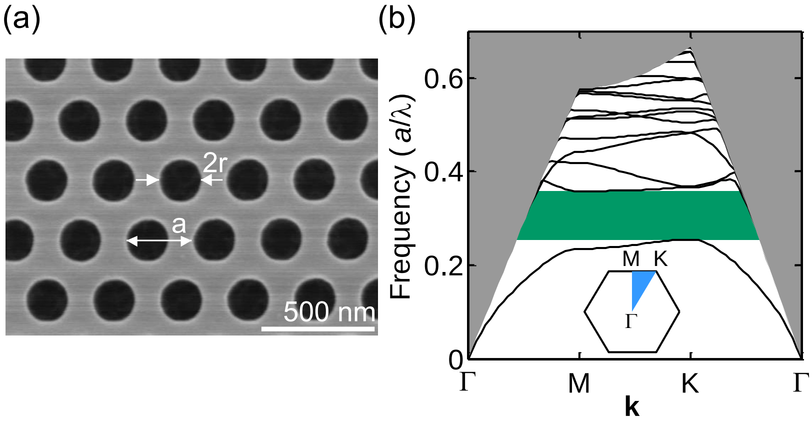

Figure 1.7: (a) Top-view scanning-electron microscope (SEM) image of a PhC fragment, where air holes with a diameter of $2r$ are arranged in a triangular lattice in a slab of GaAs. (b) Band structure (only of the TE modes) of the triangular lattice PhC. The radiation modes above the light line are illustrated by the gray shading and the band gap is shown in green. The horizontal axis is the wavevector along the edges of the region indicated by the blue shading in a hexagonal Brillouin zone. The vertical axis is the normalized frequency expressed as the ratio a/λ between the PhC lattice constant and the wavelength of light.

the total internal reflection at the air-GaAs interface. The band structure of the triangular-lattice PhC slab is shown in Fig. 1.7(b), where the black lines depict the eigenmodes of the slab and the radiation modes above the light line are shown by the gray shading. The photonic band gap for the transverse-electric (TE) modes (green shading) is opened.[3] It has been demonstrated that the spontaneous emission of an emitter could be inhibited by a factor of up to 70 due to the presence of the photonic band gap in such a slab [24]. Since the fabrication allows the realization of almost arbitrary PhC designs, it is possible to introduce defects in a perfectly periodic photonic structure, which cause deterministic localization or guiding of light emitted by a QD. This lays the foundation for making efficient quantum photonic devices, such as deterministic single-photon sources or platforms for studying light-matter interaction [6]. For the realization of a single-photon source, a particular type of defect, a PhC waveguide, is an attractive choice since efficient coupling (> 98%) of a QD to the propagating mode of the waveguide has been demonstrated [31].

A PhC waveguide is a line defect introduced into a PhC slab by removing one row or by evenly shifting in opposite directions two adjacent rows of holes. A typical example of such a structure is shown in Fig. 1.8(a), where a so-called W1 waveguide is formed by removing one row of holes. Three TE guided modes form in the photonic band gap, as illustrated in Fig. 1.8(b), where the primary guided mode is indicated by the red line and the secondary modes are shown in black. Light is allowed to propagate along the waveguide at a given frequency determined by the mode dispersion. The slope of the dispersion defines the group velocity of the guided light $v_g = \frac{\partial \omega}{\partial k}$, where ω is the frequency of the guided mode and k is the corresponding wavevector. At the cutoff

---

[3] Opening a photonic band gap for the transverse-magnetic (TM) modes requires small filling factor r/a, which is hard to achieve in practice for PhC designed to operate in the near-infrared regime.

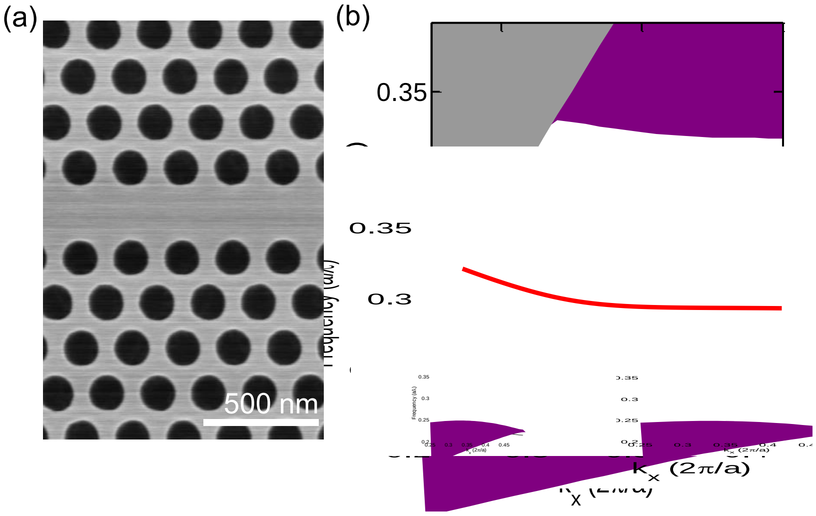

Figure 1.8: A PhC-waveguide structure used in this work. (a) SEM image of a fragment of a W1 waveguide. (b) Band structure of the W1 waveguide illustrating the dispersion of the TE guided modes emerging in the photonic band gap. The primary mode is indicated by the red line and the secondary modes are shown in black. The purple shaded area shows the continuum of modes in the waveguide bands and the radiation modes are shown in gray.

frequency of the guided mode, v_g tends to zero meaning that the group index $n_g = c/v_g$, where c is the speed of light, diverges at that point and allows to achieve a so-called slow-light effect. The change in the decay rate resulting from the slow-light effect can be quantified by the Purcell factor, P_{F}, which is defined as the ratio between the decay rate of an emitter imbedded in a photonic nanostructure and the decay rate of an emitter in a homogeneous medium. For QDs in a PhC waveguide, the Purcell factor is given by [6]:

$$P_{\mathrm{F}}(\omega) = \left(\frac{3}{4\pi n} \frac{\lambda^2/n^2}{V_{\mathrm{eff}}/a} \right) n_g(\omega), \tag{1.6}$$

where V_{eff} is the effective mode volume, and λ/n is the wavelength within the material, where n is the refractive index of the material. Experimentally, n_g up to 300 has been measured in silicon PhC waveguides, whereas in GaAs PhC waveguides group indices up to 120 have been observed [31, 32]. The limiting factor of experimentally achievable values of n_g is the Anderson localization of light at the frequencies around the band edge, which is close to the primary mode at the edge of the Brillouin zone.

1.4 Electric field on quantum-confined structures

In the following, the effect of the electric field applied to quantum-confined semiconductor heterostructures is briefly discussed. An electric field on a bulk semiconductor causes a change in the optical absorption at the band edge. This effect is known as Franz-Keldysh effect [33]. For quantum heterostructures, this effect is even stronger and is called quantum-confined Stark effect [34]. An external direct-current (DC) electric field F applied on the QW structure in the growth direction changes the bound-state energy levels and influences the optical properties of the well, i.e., it results in the exciton energy shift $\delta E = eFd_X$, where e is the electron charge, and d_X is the separation between the electron and the hole. The ability to apply the electric field is provided by the presence of p- and n-doped GaAs layers in our heterostructure. A built-in potential V_{bi} forms across the intrinsic layer of the p-i-n heterostructure as a result of charge-carrier diffusion to the oppositely charged sites. The magnitude of the total electric field is given by:

$$F = \frac{V_{bi} - V}{l_i}, \tag{1.7}$$

where V is the applied voltage and l_i is the thickness of the intrinsic region of the heterostructure. For GaAs, V_{bi} is close to 1.43 V at room temperature and 1.52 V at 10 K. Depending on the polarity of the applied field, the electrons can be pulled towards the anode and the holes towards the cathode or vice versa allowing for a reversible tuning of the transition energy and the recombination rate.

The external field breaks the inversion symmetry of the well in the flat-band condition and relaxes the parity selection rules, allowing the optical transitions between the electronic states of opposite parity, as shown by the dotted arrows in (Fig. 1.3 (b)). Increasing the field also weakens the transitions with $\Delta n = 0$ due to reduced overlap of the distorted wavefunctions.

The Stark shift of the excitons confined in quantum dots is described by $\delta E = pF + \beta F^2$, where the first term is given by the dipole moment of the QD, $p = ed_X$, oriented along the growth direction, and the quadratic term arises from the polarizability, β, which describes how easily the carriers can be pulled apart by the electric field [35]. For a symmetric QD $p = 0$, however, as mentioned before, self-assembled QDs are not perfectly symmetric, therefore, $p \neq 0$, i.e., a finite electron-hole displacement at zero electric field is observed.

Chapter 2

Fabrication of nanophotonic devices

Photonic crystals (PhC) are made by periodic sub-wavelength variation of optical materials with different refractive indexes. Examples of natural PhCs are opals and butterfly wings. The breakthrough in 2D PhC fabrication on semiconductors has been achieved two decades ago when the first PhC operating at the near-infrared regime was demonstrated [36]. Since then planar semiconductor technology has been fruitfully serving for the PhC fabrication. However, this technology was originally developed for silicon, which is so far the most important semiconductor in industry, but has an indirect band gap, and therefore, poses a great challenge in making active photonic devices. Transferring all the fabrication processes onto a platform of III-V semiconductors has not been an easy task and still relies heavily on a technical know-how being developed by many research groups across the world. The main steps of fabrication of nearly any optoelectronic device with PhC structures are summarized in Fig. 2.1. These steps can be grouped into the following processes: lithography, etching, and contact deposition. Each process is described in this chapter with particular emphasis on the technical details developed during the years of this project.

The PhC fabrication in this work relies on a so-called soft-mask process, where the desired pattern is transferred on a layer of resist and then etched directly with an inductively coupled plasma (ICP) etcher. A crucial parameter in this case is the ratio between the etch rates of the resist and the semiconductor, which determines how deep the semiconductor can be etched before the resist mask is removed by the plasma. Robustness of the resist mask is particularly important when etching such small features like holes in a PhC. In order to ensure etching selectivity in III-V semiconductors, an intermediate layer of Si_3N_4, SiO_2, metal oxide or metal is often used, which is known as a hard-mask process [37–39]. However, a hard mask often complicates fabrication on surfaces where oxide layers have been deposited for other purposes, such as fabrication of superconducting single-photon detectors [40]. After the ICP etching, a necessary step needed to release the PhC membrane from the substrate involves wet chemistry with hydrofluoric acid (HF), which, in general, is not a clean process resulting in various debris and contamination of the structures. Therefore, it is important to identify the etching residues and remove them with the appropriate chemicals. In this work, a cleaning procedure used in our fabrication flow is presented, allowing to achieve high-quality residue-free photonic structures [41]. Finally, the deposition of robust ohmic contacts is described. Ohmic contacts integrated onto photonic circuits enable fast

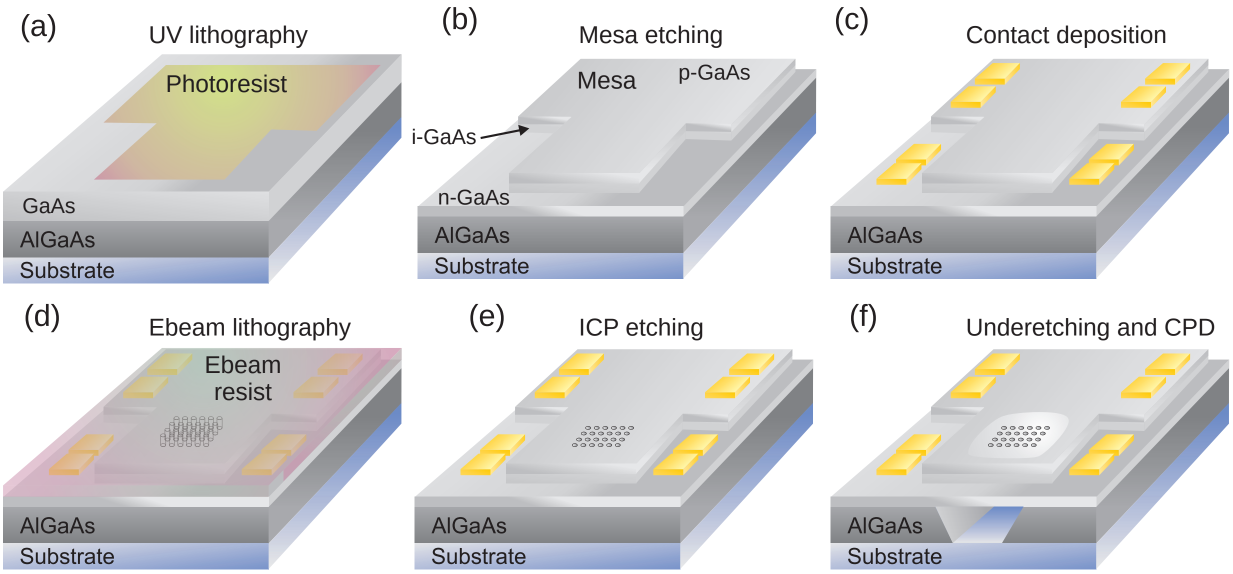

Figure 2.1: Fabrication flow of PhC structures with ohmic contacts. (a) By means of ultra-violet (UV) lithography a mesa structure is defined on a sample. (b) The design of the photoresist mask is transferred on a GaAs membrane by wet chemical etching. The etching is stopped at the surface of n-doped GaAs where the bottom contacts will be deposited. (c) Ohmic contacts are deposited on p-type GaAs and n-type GaAs by electron-beam (e-beam) and thermal evaporation of several metal layers on a double-layer resist mask, which allows to lift-off the metal from the unwanted parts of the sample. (d) The e-beam resist layer is patterned with a PhC design by means of e-beam lithography. (e) The PhC pattern is etched into the GaAs membrane via the ICP process. (f) The PhC membrane is released from the substrate via selective etching of AlGaAs with HF. The sample is dried in a critical point dryer (CPD), which suppresses damaging effects of capillary forces.

and flexible control of optical and electronic properties of the fabricated devices for a variety of applications [42–44].

By employing the developed fabrication process, a variety of photonic nanostructures are fabricated for several experiments conducted in the group. Some of these experiments are briefly overviewed in this chapter. Additionally, results on studies of light localization in bent PhC structures are presented.

2.1 Lithography

Lithography is used to transfer arbitrary structure designs on a layer of a polymer. In the following, two types of lithography employed in this work — photolithography and e-beam lithography — are described in more detail. In the former, a positive (negative)-tone photosensitive resist is used, which upon the illumination with light becomes soluble (insoluble) in basic solvents, referred to as developers. In this thesis, the positive-tone resist is referred to simply as a resist, unless specified otherwise. A metallic mask, where the desired geometry is imprinted, is used in-between the sample surface and the UV light source to cover parts of the sample which should not be removed. As a result a photomask is obtained and further fabrication processes can take place. Similarly, in

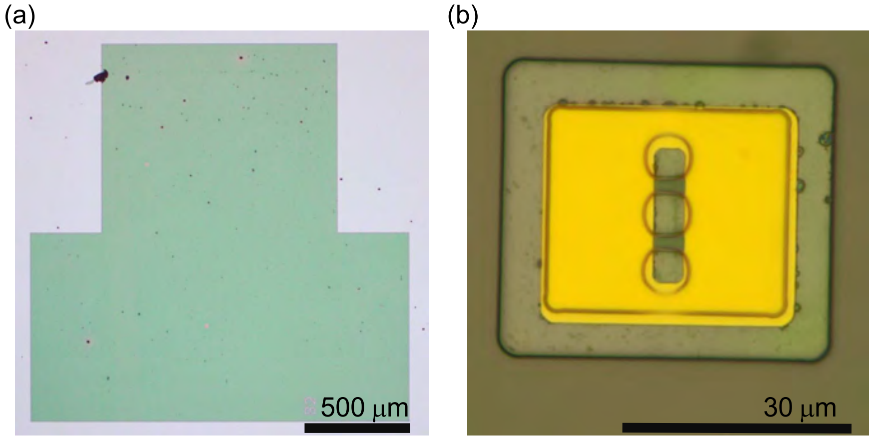

Figure 2.2: Examples of a photoresist mask defined by the UV lithography. (a) Millimeter-size mesa structures are defined on samples where electrical gates are used. (b) Features as small as a couple of micrometers can be transferred into the resist mask. Alignment of $\sim 1\,\mu$m precision is achieved by using a microscope objective with 50x magnification.

e-beam lithography a beam of focused electrons is used to break bonds between polymer chains and increase the solubility of the resist. Since the electrons in the beam have wavelength so small that the diffraction no longer limits the resolution, record-small features of 3 nm sizes can be patterned in e-beam resists with highly accelerated electrons [45]. Sub-5 nm precision is preferred in fabrication of photonic structures of high optical quality.

2.1.1 UV lithography

Classical UV lithography where a sample covered with a layer of a photoresist is exposed with the light of a mercury lamp (365 nm) allows fast and flexible patterning of structures with a feature size of at least 1 µm. This limit is set by the wavelength of the used light, the thickness, and the sensitivity of the photoresist. In this work, positive-tone, negative-tone, and image reversal photoresists are used for various purposes. A positive-tone thin resist AZ1505 is used for the mesa definition and in a double-layer lithography, see Fig. 2.2(a). A double-layer lithography is used in a few cases to define a mask for the electrical contacts: two resists of different photosensitivity are spun sequentially on the sample such that a negative inclined profile is obtained, allowing for a solvent to creep under the deposited metal layer and lift-off the unwanted parts of the metallized resist. A similar re-entrant profile of the resist sidewall is obtained in a negative-tone resist ma-N400, which is used for most of the samples described in this work since it requires a single-step process as opposed to the double-layer lithography. For the fabrication of the GaAs bridges described in Chapter 4, an image-reversal resist AZ5214E is used. An example of a pattern on a layer of AZ5214E used in a positive-tone is shown in Fig. 2.2(b). Depending on the situation, this resist can be used both as a positive- and negative-tone resist. The description of the detailed treatment of each resist is provided in Appendix A.

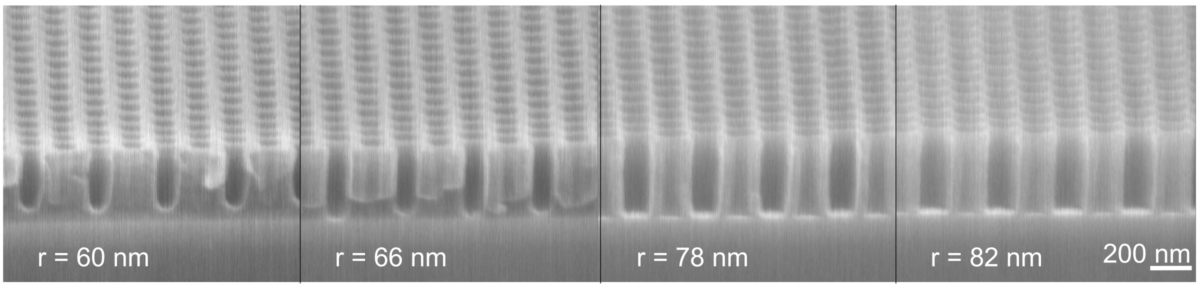

Figure 2.3: Mask profile dependency on the size of the features patterned with the e-beam lithography. SEM images of the cross-sections of the resist masks patterned with PhC structures with a different hole radius *r* indicated for each image. An exposure dose of 408 µC/cm^2 and o-xylene as a developer are used for all the masks.

2.1.2 Electron-beam lithography

E-beam lithography is a corner stone of the whole fabrication process of PhC nanostructures. The resist mask provides a basis to transfer the desired patterns into GaAs membranes. The quality of the mask is translated into the quality of the final structure with additional disorder due to subsequent processes, and therefore, it is of great importance to ensure that the resist mask is patterned properly. Usually, PhC structures have feature sizes of 120 – 170 nm with a periodic spacing of 70 – 150 nm, which set the resolution requirements for the lithographic technique being used. As mentioned before, the e-beam lithographic resolution is not set by diffraction, but is limited by electron optic aberrations and, more importantly, scattering of electrons within the resist and the substrate. These scattering events result in an additional exposure in the surroundings of the spot where the electron beam is impinging and give rise to the so-called proximity effect. The proximity effect is the cause of variations in pattern size with respect to the intended by design. This detrimental effect is less pronounced for electrons of higher initial energy since they travel interacting weakly with the resist molecules throughout the resist layer. Therefore, e-beam lithography machines accelerating electrons with 100 kV voltage are the most common choice for PhC fabrication. The tool used in this work is a modified ELS-7000EX (ELIONIX) with an acceleration voltage of 100 kV. Note that the amount of scattering also depends on the material in which these events occur and the substrate. While there is no freedom in our case to choose the substrate, we work with the state-of-the-art e-beam resist ZEP520A. Apart from high resolution, sensitivity, and contrast, ZEP520A possesses characteristics crucial for the soft-mask process, i.e., robustness against dry etching.

In this work, a 530 nm-thick layer of ZEP520A is used to pattern samples with an adjusted exposure dose, which measures an amount of charge per unit area (in µC/cm^2) needed to degrade the resist. The required exposure dose strongly depends on the feature size: larger doses are needed to fully open smaller patterns, as shown in Fig. 2.3. Here a 408 µC/cm^2 exposure dose is used to pattern periodically spaced holes with a radius $r = 60$, 66, 78, and 82 nm. Clearly, the holes with

$r = 60$ and 66 nm are not fully open and a larger dose is needed to produce a high-quality mask. On the other hand, holes with $r = 78$ nm are open, but the vertical profile of the sidewalls has a small positive inclination, which results in a smaller hole size at the substrate compared to the top of the resist layer. The optimal result is obtained for the largest holes with $r = 82$ nm, where the resist edges are vertical and sharply defined throughout the whole layer thickness. Moreover, it is found that the dose needed to fully open the holes in a PhC strongly depends on the developer used. In the beginning of the e-beam process development, o-xylene is used to develop ZEP520A exposed with a dose of $\sim 400\,\mu C/cm^2$. In the final recipe it is replaced with n-amyl acetate (ZED-N50), which allows to reduce the exposure dose for the same patterns to $\sim 300\,\mu C/cm^2$. The detailed recipes for the e-beam lithography used in this work can be found in Appendix A.

Oftentimes, micrometer-sized openings have to be placed in close proximity to the PhC in order to form other structures for light guiding. Generally, large structures require smaller exposure doses to be opened than finer features. Therefore, patterning large structures and small features on the same mask calls for a local dose adjustment in order to ensure equally high-quality of different-scale features. A similar procedure is used to correct for the proximity effect. Usually, an additional software is employed to calculate a uniform energy profile for a pattern taking into account the scattering processes. The proximity-effect correction is essential when exposing masks with small features with the e-beam systems where the acceleration voltage is below 50 kV. In general, it also improves the quality of the masks patterned with 100 kV machines. In this work, the proximity correction is implemented by exposing large patterns with a smaller dose and using a larger dose for the PhC structures. This procedure allows to obtain close-to-design dimensions of all features in the mask and provides a good starting base for the etching process.

2.2 Etching

Transfer of the e-beam mask onto semiconductor is achieved by removing the exposed parts of the material, i.e., by etching them. Diverse chemical solutions can be used as etchants, with an adjustable material/crystalline direction selectivity and etching rate. The wet etching is inadequate for defining features smaller than $\sim 1\,\mu m$ and is isotropic, which is not desired in certain situations, e.g., when etching holes in a PhC membrane. Therefore, for such purposes dry etching by ion bombardment and gaseous chemistry is used instead. The success of the PhC-device fabrication, however, lies in a synergy of both types of etching. In this section following the chronology of the fabrication process, the dry etching is discussed first, and the subsequent cleaning and undercut procedures are presented.

2.2.1 Inductively coupled plasma etching

In this work, dry etching of GaAs membranes takes place in an ICP etcher, which schematics is shown in Fig. 2.4. Different types of gas are supplied to the vacuum chamber through the pipelines connected to gas bottles. The composition of the gas mixture is controlled by adjusting the flow in each gas pipeline. An oscillating current running in a coil (equivalent to the ICP power) induces dissociation of gas molecules into ions and radicals. If the ICP power is set to zero, the etcher

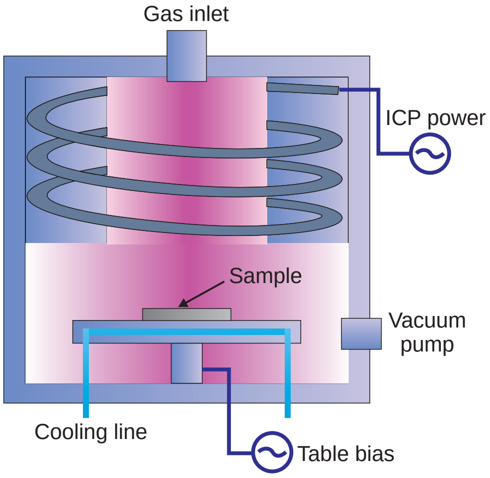

Figure 2.4: Schematics of the ICP etcher used in this work. Gas is introduced from the top of the vacuum chamber and pumped out below the table. A plasma discharge (purple shaded area) is generated between the grounded chamber walls and the table-electrode by the oscillating current running in the coil. The DC bias directs the plasma to the sample mounted on the table, which is constantly cooled by helium gas.

operates in a so-called reactive ion etching (RIE) mode, which is often used for etching at a slower rate. The charged particles get accelerated by the DC bias of the table electrode and contribute to the physical etching by ion sputtering, whereas the ICP power determines the reactivity of the plasma and thus the degree of the chemical etching by reactive radicals. The physical etching is directional and allows to achieve vertical sidewalls, but it might damage the sample surface. Enhancing the chemical part allows to improve the etching selectivity, but the process becomes more isotropic. The composition and pressure of the gas also allow to control the nature of the etching [46].

GaAs/AlGaAs dry etching is based on halogen-gas chemistry. The highest etching rates are achieved by using Cl_2 sources, but at a cost of an increased surface roughness and reduced reproducibility in the etch rates in the longer run. By adding Ar or BCl_3 to the Cl_2 etching, anisotropy can be increased due to increased contribution of the ion sputtering. Moreover, sidewall passivation by addition of BCl_3 and N_2 improves the anisotropy and verticality of the sidewalls [47]. The surface smoothness and anisotropy is improved by adding some H_2 to a Cl_2/Ar mixture. This also reduces the etch rate. In order to speed up the etching process, a chamber pressure can be increased to facilitate a more chemical etching due to a denser plasma, which, however, results in the reduced verticality of the sidewalls. Generally, the dry-etching recipe is developed depending on the type of the mask and the substrate material, and also on the patterns to be etched. In our case, the main requirements for the dry etching are good etching selectivity, verticality of the sidewalls, and smooth surfaces.

In the following, the dry etching recipe used to fabricate the samples used in this project is presented. Patterns defined by the e-beam lithography are etched through the GaAs membrane

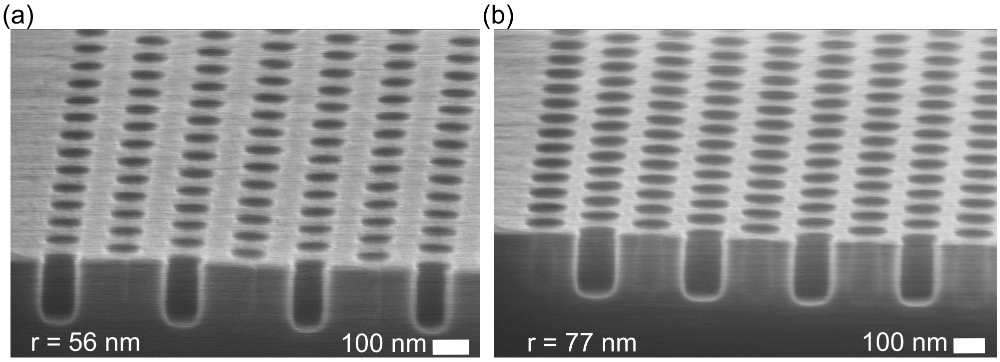

Figure 2.5: PhC membranes dry-etched with the developed recipe. Holes with a radius $r = 56\,\mathrm{nm}$ (a) and $r = 77\,\mathrm{nm}$ (b) etched into a GaAs membrane.

grown on the sacrificial AlGaAs layer (Fig. 2.1(e)) in the ICP etcher PlasmlabSystem 100 ICP65 (Oxford Instruments). A plasma chemistry based on BCl_3, Cl_2, and Ar is used [48]. The nature of the etching process is controlled by balancing the ICP power and the DC bias on the table electrode. The ICP coil power is set to 300 W, since higher values lead to lower selectivity. The DC bias is maintained at 300-320 V. The plasma in the vacuum chamber is ignited at a strike pressure of 25 mTorr and then rapidly lowered to 4 mTorr. The table is cooled to 0 °C to avoid excess heat due to the plasma, which might cause distortions in the resist mask due to a thermal reflow (occurring at around 145 °C for ZEP520A). The sample is mounted on a Si carrier wafer ensuring a thermal contact via thermally conductive Fomblin oil, which can be easily removed after the process. Thermal contact between the carrier wafer and the table is maintained by a constant helium flow. Under such conditions, a gas mixture of $BCl_3/Cl_2/Ar$ with the flow rates of 3/4/25 sccm, respectively, is used to achieve the desired quality structures. In-situ monitoring of the remaining resist thickness by a laser interferometry allows to properly time the etching process. It is found that the resist mask should remain at least 200 nm-thick to prevent erosion of the sidewalls and distortions in the feature size. The resist etch rate in the presented recipe is around $280\,\mathrm{nm\,min^{-1}}$ and the total etching time is 45 – 55 s.

The plasma etching suffers from the so-called depth lag, which means that the small features are etched shallower than the large ones. This sets a minimum requirement on the hole size that can be etched through the full thickness of the GaAs membrane. Holes with the radius as small as 56 nm can be fully etched through a 160 nm-thick membrane with the developed recipe, see Fig. 2.5(a). The corresponding etch rate is $\sim 190\,\mathrm{nm\,min^{-1}}$, which results in a selectivity of GaAs etching over the resist mask of 2:3. Selectivity is improved to 2:1 for etching larger than 1 µm features since the depth lag effect becomes less important. The ICP etcher operating in the RIE mode can be used for deep etching of large features, e.g., mesa structures. The etch depth can be controlled as precisely in the ICP process as in the nonselective wet chemical etching, which allows to simplify the fabrication process by avoiding some steps involving wet chemistry. On the other hand, the dry etching is generally nonselective and not suitable for underetching of the sacrificial AlGaAs layer, which is one of the last steps in the PhC-membrane fabrication.

2.2.2 Wet chemical etching

In order to release the PhC membranes from the substrate, selective etching of the sacrificial AlGaAs layer is employed.[1] Dilute HF dissolves $Al_xGa_{1-x}As$ with $x > 0.5$ while etching very little GaAs [49]. The sacrificial layer of all samples fabricated in this work have had Al content of 0.7 or 0.75. The barrier layers of the p-i-n structures have $x = 0.33$ of Al and are etched with a negligible rate. After the dry etching, the fabrication process is continued by stripping a residual layer of ZEP520A by immersion in n-methyl-2-pyrrolidone (NMP) at 60 °C for 10 min, rinsing in room temperature NMP, IPA, and blow drying with nitrogen gun. A liquid HF solution of 10% is used for selective removal of AlGaAs followed by a thorough rinse in millipore water. The lateral etch rate is estimated by investigating the undercut of the sample and is found to be around $65\,\mathrm{nm\,s^{-1}}$. The GaAs membranes remain intact after the underetching, however, several residues are observed on the fabricated structures. During the wet etching with HF, compounds of Al are formed, most of which are gaseous or highly soluble in water, but some compounds require additional aids to be completely dissolved [50]. Additionally, byproducts of the dry etching may deposit on the inside and the top of the etched features. By inspecting the debris with an optical microscope and an SEM, micrometer-sized crystals with a trigonal lattice are observed and identified as aluminum trifluoride AlF_3, see Fig. 2.6(a) – (b). Amorphous aluminum hydroxide $Al(OH)_3$ residues are observed when underetching in HF vapours and are easily removed with potassium hydroxide (KOH) [51]. Thin films of amorphous residues all around the released GaAs structures are observed after the underetching, see Fig. 2.6(c). We speculate that these residues are of organic nature stemming from the e-beam resist. During the etching with hot plasma carbon-rich films may form and redeposit on the etched structures. Ashing with oxygen (O_2) plasma seems to partially remove these films, however, additional treatment is required to thoroughly clean the etched structures.

A procedure consisting of several steps before and after the HF treatment is implemented in order to clean the fabricated structures of all the observed residues. After resist removal, the sample is immersed in an aqueous solution of KOH (25 g in 100 mL) for 5 min to remove the remnants of the Fomblin oil. After rinsing in water, the sample is undercut in the dilute HF and soaked in fresh water to stop the etching and dissolve AlF_3. To remove the other byproducts of this reaction and the dry etching, the sample is immersed in hydrogen peroxide (H_2O_2 30%) for 1 min followed by a 1 min water rinse and 2 min etching in 20% KOH. H_2O_2 oxidizes the surfaces of the GaAs membrane and the residuals of the sacrificial layer, whereas KOH easily dissolves the produced oxides. Figure 2.6(d) shows an SEM image of a pristine structure obtained after the cleaning procedure. The consecutive steps of oxidation and deoxidation are used in a so-called digital etching, which has inspired the cleaning procedure [52]. Such a process etches GaAs by a few nanometers, which increases the size discrepancy between the fabricated and the designed structures. In our case, a single-cycle digital etching results in 2 – 3 nm larger hole diameter as compared to the design, which is consistent with the literature reported values [52]. Such a discrepancy can be easily compensated by adjusting the initial mask design. Note that the dry

---

[1] In order to avoid the formation of a thick native AlAs oxide, the wet etching should be performed immediately after the dry etching.

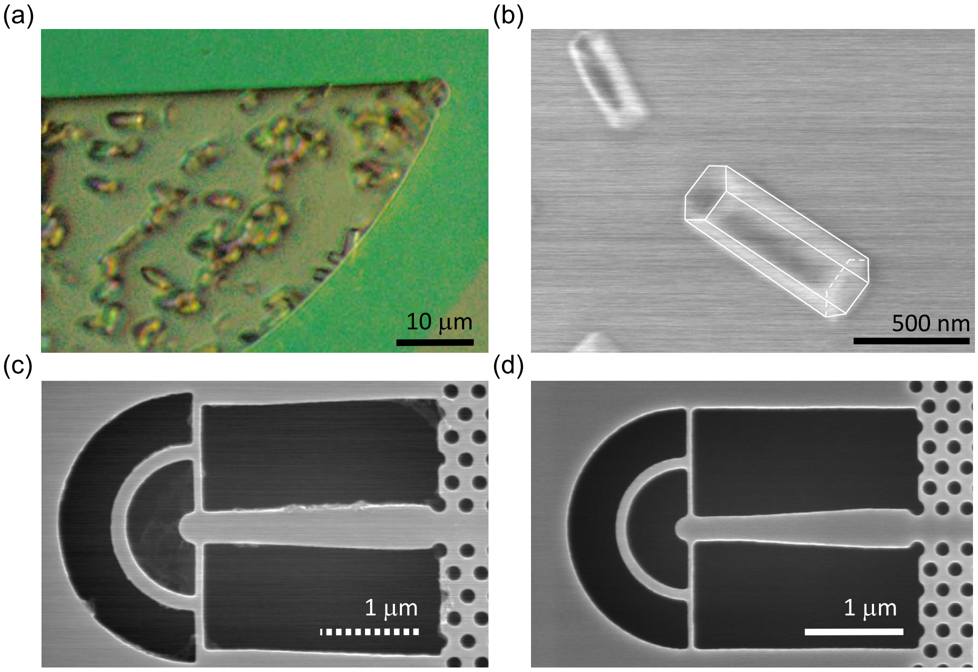

Figure 2.6: Residues of the etching processes and the final structure after the cleaning procedure. AlF_3 crystals forming during the HF etching are observed through an optical microscope (a) and their crystalline structure (emphasized by the white lines) is inspected with an SEM (b). (c) A residual thin film occurring due to the dry etching is attached on a released structure. (d) All the residues are removed with a cleaning procedure described in this work resulting in a high-quality structure.

etching transfers the pattern of the resist mask without observable deviations in size.

The last step in the fabrication process concerns drying of the PhC membranes and other suspended structures. Generally, thin semiconductor membranes are not robust to capillary effects occurring when the sample is taken out of the water or IPA at the end of the process. These effects might cause collapse of the structure or stiction to the substrate [53]. Therefore, care is taken to keep the sample covered with a liquid droplet during all the steps after treatment with HF. Depending on the size of the suspended structures, after rinsing in IPA the sample is dried by letting IPA evaporate in the fume hood or in a critical point dryer (CPD) through an exchange with liquid carbon dioxide. The latter method is necessary for very fragile features, e.g., long ridge waveguides or PhC nanobeams.

Several samples fabricated in this work require deposition of electrical contacts. A mesa structure has to be defined before to expose the n-doped GaAs layers for the bottom contacts. It is defined by the UV lithography and the nonselective etching with a water solution of orthophosphoric acid and hydrogen peroxide H_3PO_4:H_2O_2:H_2O (1:4:45) or the dry etching until the surface of the n-GaAs layer. Afterwards, the UV lithography is used to define a mask for contact deposition. The detailed recipes for these processes can be found in Appendix A.

2.3 Ohmic electrical contacts

An important ingredient of photonic device fabrication is electrical contacts, which allow to externally control the device properties via the application of an electric field. The electric field is changed by applying the voltage through the metal contacts across the intrinsic layer of the semiconductor membrane. There can be two kinds of contacts formed between a metal and a semiconductor: ohmic contacts, which voltamperic characteristic follows Ohm's law, and Schottky contacts, which work as a rectifier, similar to the pn diode. The electrical properties (sheet resistance, etc.) of the ohmic contacts can be measured allowing to evaluate the magnitude of the electric field in the structure. Low-resistance contacts are desired for a high-quality diode without parasitic heating and charging. Nevertheless, Schottky contacts are widely used as electrical gates by research groups in optoelectronics and nanophotonics since they are easier to fabricate on compound semiconductors, such as GaAs [54]. In this section, the most common strategies of making ohmic contacts on GaAs are reviewed, and the recipe for the deposition of the ohmic contacts compatible with the PhC-membrane fabrication and cryogenic environment is presented.

A variety of materials have been tested for making electrical contacts on p- and n-doped GaAs [55, 56]. Achieving the ohmic behavior of the n-type contacts poses no challenge since 1967, when Braslau *et al.* fabricated low-resistance contacts by evaporating layers of Ni, Ge, and Au [57]. Such a combination of metals has been routinely used as an electrode in devices with electrically controllable quantum emitters [43, 58–61]. Alternatively, indium-noble metal alloys (InAg, InAu, InPt) can be used to contact the n-type GaAs [56].[2] Despite an extensive material research for low-resistance ohmic contacts to the n-GaAs, today the most common choice for a variety of applications is the very first proposal of NiGeAu alloy [57]. Quite the opposite is the case for the p-doped GaAs, where there seems to be no unified convention in fabrication of reliable and good quality ohmic contacts. For highly doped ($> 1 \times 10^{19}\mathrm{cm}^{-3}$) p-GaAs, annealed TiPtAu, TiAgPdAu, and NiPdAu alloys have been reported to serve as low-resistance electrodes [62–64]. One of the most common choices is a combination of Au and Zn [42, 65–67]. Here Zn is used to surface-dope GaAs. However, Zn tends to adhere poorly to the surface of GaAs, which reduces sample endurance during further fabrication processes and might complicate the wire bonding process. Moreover, the vapour pressure of Zn is much higher than of the other metals, therefore, it is often regarded as a contaminant in the vacuum processes, such as an e-beam evaporation. Oftentimes, for highly doped ($> 2 \times 10^{18}\mathrm{cm}^{-3}$) p-GaAs a simple to fabricate, but worse in electrical performance, solution is preferred by depositing layer of Ti and Au or an optically transparent layer of titanium indium oxide (ITO) [68, 69].

In this work, the ohmic contacts to the n-GaAs are prepared in an e-beam evaporator, where a source of a metal is heated by the bombardment with energetic electrons, and metal atoms are deposited layer by layer. Right before the metallization, the sample is ashed in the O_2 plasma to remove the organic residues and deoxidized in a solution of H_3PO_4 for 2 min to expose a pristine GaAs surface. The following sequence of metal layers is used: 5 nm of Ni, 40 nm of Ge, 60 nm of

---

[2] As a poor man's solution, indium alone can be annealed to n-GaAs to obtain ohmic contacts of a reasonable quality.

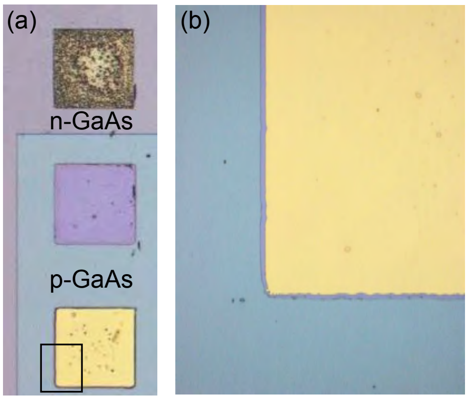

Figure 2.7: (a) Optical micrograph of a corroded area in the p-GaAs layer where one of the p-type contact pads has detached from the surface. (b) A magnified view of the area around the p-contact defined by the black rectangle. The etching takes place before the p-type contact deposition, therefore, the p-GaAs layer is etched underneath the metal as well.

Au, 27 nm of Ni and at least 100 nm of Au. The bottom layer of Ni is mainly meant to prevent the so-called balling-up effect of AuGe alloy. During the annealing process the sample is heated such that the metals melt and AuGe tends to form droplets, which deteriorates the morphology of the contacts, which is particularly important for small contacts and traces. A layer of Ni serves also as a wetting agent and has been found to improve the electrical quality of the contacts by consuming the native oxides and forming compounds with GaAs [70]. The superior electrical properties of this type of contacts are mainly due to Ge used as a dopant that diffuses into the GaAs region near the metal interface. By evaporating a layer of gold, Ni and Ge are protected from the ambient environment, whereas a subsequent layer of Ni improves surface morphology and serves as a barrier preventing the penetration of Au into the heterostructure (spiking) during the annealing. The top layer of gold is needed for the wire bonding, which is done easier on a thick coating. After the metallization, the unwanted parts of the coating are removed during a lift-off process. The deposited contacts are annealed in a rapid thermal annealer (RTA) for 20 s at 420 °C in the forming gas (N_2–H_2) atmosphere, see Appendix A.

The p-type contacts to GaAs are formed by a sequential deposition in a thermal chamber of 20 nm of Au, 50 nm of Zn, and at least 100 nm of Au for the wire bonding. The first Au layer is evaporated to improve adhesion of the Zn layer. The Zn layer is used as a dopant, which diffuses into GaAs during the annealing process. In order not to block the Zn penetration, the first Au layer is thus only 20 nm thick. Zn is capped with a thick Au film that prevents vaporization of Zn during the annealing in a thermal furnace and also forms a robust contact pad.

The deposition of both p- and n-type contacts with the described procedure necessitates the UV lithography step involving sample immersion into aqueous solutions before the metallization with AuZn. In some cases the presence of the n-type contacts with an extensive immersion in water solutions during the development of the exposed photoresist is found to facilitate the etching of the p-GaAs, as shown in Fig. 2.7. Depending on the sample and the treatment conditions

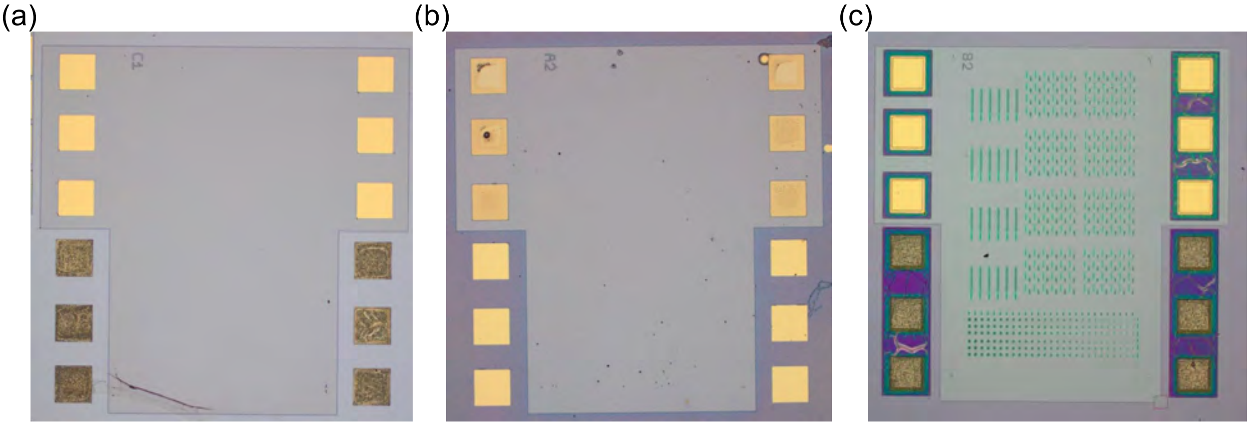

Figure 2.8: Electrical contacts deposited by following the recipes described in this work. (a) Ni/Ge/Au contacts are evaporated on the n-GaAs and annealed in the RTA, and the p-type contacts are made by depositing layers of Au and Zn followed by annealing in a thermal furnace. (b) The contact metals are deposited in an inverse manner compared to (a) and annealed in a thermal furnace. (c) Optical micrograph of the final sample where the PhC structures are fabricated on a mesa with ohmic contacts. The metal pads are covered with a hard-baked photoresist mask in order to protect them from damage of the hot plasma.

(time spent in the solution, illumination), the p-doped layer can be etched to a certain depth. Since the total p-layer thickness in our samples is only 40 nm, etching even ten nanometers can significantly deteriorate the electric behaviour of the deposited contacts. In the worst case, the p-GaAs layer can be etched completely resulting in metal pads contacted to the intrinsic GaAs through a Schottky barrier. We experienced that this etching occurs only for the p-GaAs and only when the n-type contacts are already deposited on the sample. Therefore, it is suggested that this is the case of galvanic corrosion, where the developer acts as an electrolytic solution and the p-GaAs surface undergoes the anodic oxidation. The oxidation products are then immediately dissolved in the aqueous electrolytic solution. This phenomenon is well known in GaAs wafer processing, and a strategy of slowing down or inhibiting the reaction, by processing the sample in the dark at all times when the metals have been deposited, has been proposed [71]. This strategy is implemented to prepare several samples during this work and well-behaved ohmic contacts are obtained. Figure 2.8(a) shows an optical micrograph of the sample referred to as WG1 with the ohmic contacts prepared in the dark. The six bottom n-electrodes are annealed in the RTA and are distinguished by their rough surface. Alternatively, an inverse contact deposition procedure is implemented for the sample called CQW1, which is shown in Fig. 2.8(b). Since only the p-doped GaAs is etched due to the galvanic corrosion and the n-GaAs stays intact at the presence of the p-type metals, the sequence of the metal evaporation is swapped and all contacts are annealed once in the thermal furnace. The surface of the n-contacts looks much smoother due to a different annealing method.

After deposition of ohmic contacts, the sample might undergo subsequent steps of PhC membrane fabrication, which generally results in wearing out of the contact pads and lowered electrical

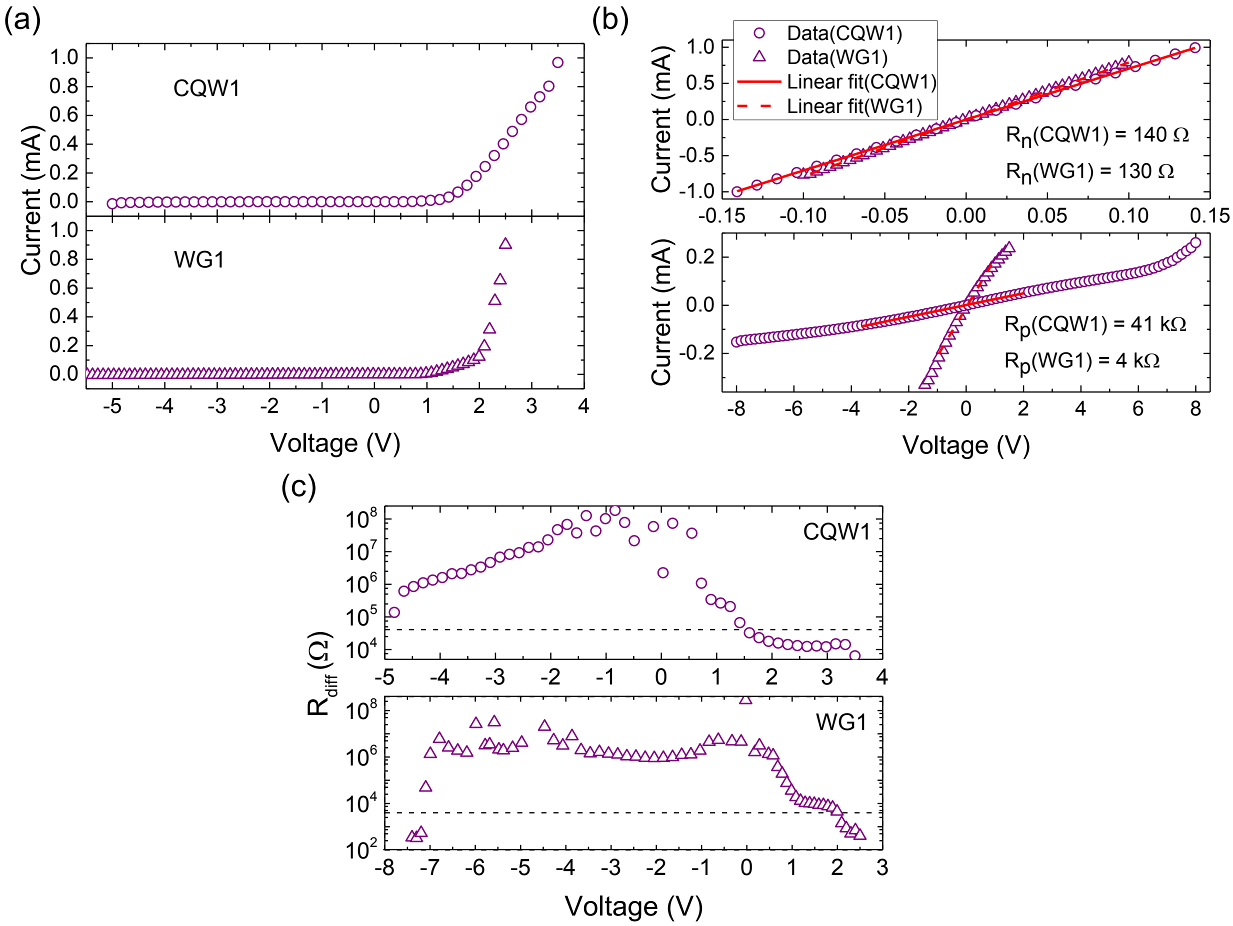

Figure 2.9: Current-voltage characteristics of the fabricated electrical contacts. (a) Diode IV curves of the WG1 and CQW1 samples. There is a negligible leakage current in reverse bias for both samples, whereas the diode turns on at a slightly higher forward bias for WG1. (b) Upper (lower) panel shows ohmic curves of the n-(p-)type contacts fabricated on the two samples. Purple circles (triangles) show the data points and red solid (dashed) line shows a linear fit for CQW1 (WG1). (c) Differential resistance of the p-i-n diode for WG1 (a) and CQW1 (b). The total p-contact resistance is indicated by the black dashed line for each sample.

performance. To protect the contacts from the destructive effects of the plasma and HF treatment, an additional hard-baked photoresist coating is formed around the frame of each electrode, as shown in Fig. 2.8(c). The small features distributed across the mesa are the fabricated PhC nanostructures.

The quality of the ohmic contacts and the p-i-n diode is assessed by measuring the current-voltage (IV) characteristics at 10 K under no illumination. A source meter (Keithley 2636A) is used to apply bias (with an accuracy of few hundred of µV) and measure the current (with few tens of nA accuracy).[3] The diode IV curves for the samples WG1 and CQW1 are shown in Fig. 2.9(a). The diode of WG1 turns on at a slightly higher voltage than the diode of CQW1, which can be due to

---

[3] The accuracy of the source meter depends on the reading value, i.e., for voltage it is 0.02% ± 350 µV, for current 0.025% ± 1.5 nA.

several reasons, e.g., different quality contacts, heterostructure, and doping concentrations of the p- and n-GaAs layers. For both samples a negligible leakage current flows in the reverse bias regime and under the forward bias before the diode turn-on.[4] The absence of the leakage current indicates the absence of charge transfer and within a certain voltage range allows to modify the electronic band structure of the sample. The IV characteristics measured between two n-electrodes of the discussed samples expose an excellent ohmic behavior of the n-contacts in cryogenic temperatures. The respective data for CQW1 (WG1) shown by the purple circles (triangles) is fitted well with a linear model indicated by the red solid (dashed) line in the upper panel of Fig. 2.9(b). The total n-contact resistance extracted from the linear fit is around 150 Ω for both samples. The lower panel of Fig. 2.9(b) shows results of the analogous measurements on the p-type contacts, where the ohmic behavior is maintained with the total contact resistance of around 4 kΩ for WG1 and 10 times larger for CQW1. The differential diode resistance defined as $R_{\text{diff}} = \Delta U/\Delta I$, where ΔU (ΔI) is the voltage (current) difference between two consecutive data points, is much larger than the contact resistance until the diode turn-on, see Fig. 2.9(c). This ensures that the bias drops mainly on the diode, but not on the contacts, and allows to efficiently control the electric field across the intrinsic layer of the sample.

Despite the challenges in making the ohmic contacts on the p-GaAs, reliable electrical gates are deposited on the samples allowing to build sophisticated devices consisting of high-quality PhC structures and embedded quantum light emitters. These achievements contribute to the development of GaAs technology and provide a flexible platform for quantum photonics experiments.

2.4 Experimental setup

Optical properties of the fabricated nanostructures are investigated by means of photoluminescence spectroscopy. Experiments with quantum emitters, such as QDs and QWs, are also carried out by measuring their emission spectra under optical excitation at low temperatures. A cryogenic environment is needed to reduce the nonradiative recombination and the phonon-assisted dephasing processes. In the following, optical setups around the cryostats used in this work are described. A wavelength-tunable Ti:sapphire laser (Coherent Mira 900) operated in a continuous-wave mode is used to excite the sample for the spectral measurements. The same laser can generate 3 ps-long pulses at a fixed repetition rate of 76 MHz when mode-locked. Alternatively, a picosecond-pulsed diode laser (PicoQuant PDL 800-B) with a repetition rate tunable from 2.5 to 40 MHz can be used. Light from both sources is conveniently coupled to a polarization-maintaining single-mode optical fiber and can be sent to any available optical setup. A mirror on a magnetic mount is used to switch between the two lasers, see Fig. 2.10(a). Before coupling to the optical fiber the laser beam is guided through a half-waveplate and a polarizing beam splitter for power control. Part of the Mira beam is sent to a photodiode (PicoQuant TDA200) that generates a trigger signal for the time-resolved measurements. The trigger signal serves as the timing reference for the repetitive registration of single photons on a silicon avalanche photodiode. The photoluminescence decay curve is then

---

[4] The term "turn-on" is used following the operational definition in electrical engineering, however, for our devices, the turn-on voltage is not well-defined and depends on many parameters, e.g., the contact quality.

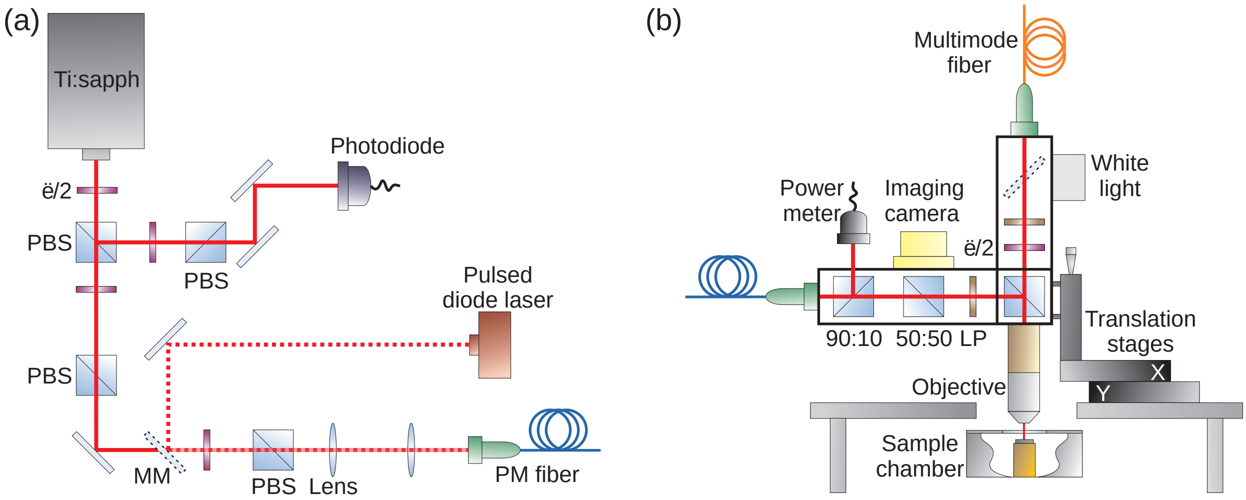

Figure 2.10: Schematics of the optical setups on the laser table and around the closed-cycle cryostat. (a) A continuous-wave laser light is coupled to a polarization-maintaining (PM) fiber and can be brought to any other optical setup. A pulsed beam from the laser diode can be coupled to the same fiber by inserting a movable mirror (MM) into the path. The laser power in each arm is controlled by a PBS and a half-waveplate ($\lambda/2$). Part of the Ti:sapphire laser light is guided to a photodiode to generate trigger pulses for time-resolved measurements. (b) An optical head around the closed-cycle cryostat is mounted on the translation stages and can be moved relative to the sample. Polarization of the laser light is cleaned with a linear polarizer (LP). The excitation beam is guided to the sample through a 90:10 beam splitter. The emission from the sample is cleaned from the laser light by a $\lambda/2$ plate and another LP. For sample imaging, a mirror (shown as the dashed contour) can be inserted to guide the white light for illumination.

reconstructed by building a histogram of single-photon events detected over a multitude of cycles of excitation and emission. It is done by a time tagging module (PicoQuant PicoHarp300) with 4 ps resolution.

Optical measurements are conducted on the sample placed either in a CS210SF-GMX-20-OM closed-cycle helium cryostat (Advanced Research Systems, Inc) or in a Microstat HiRes II (Oxford Instruments) liquid-helium flow cryostat. The sample space allows for optical and electrical access via a wedged optical window and thermally anchored copper leads. An adjustable-height copper cold finger is used for mounting the sample holder in the closed-cycle cryostat. The flow cryostat is equipped with a custom-made sample holder, described in Appendix B. The temperature is measured by a calibrated silicon diode sensor (accuracy of ± 12 mK) and controlled by a 50 Ω thermofoil heater anchored on a cold finger. In the experiments conducted in the closed-cycle cryostat the CQW1 sample is cooled to 4.2 K.

Schematics of an optical setup around the closed-cycle cryostat is shown in Fig. 2.10(b). A cage-based optical head is mounted on the two-axes micropositioning stages (Newport M-VP-25XL) and a translation stage with a micrometer drive for positioning in the *z*-direction. In this configuration, the sample is static, whereas the excitation/collection spot is moved in the sample plane with a

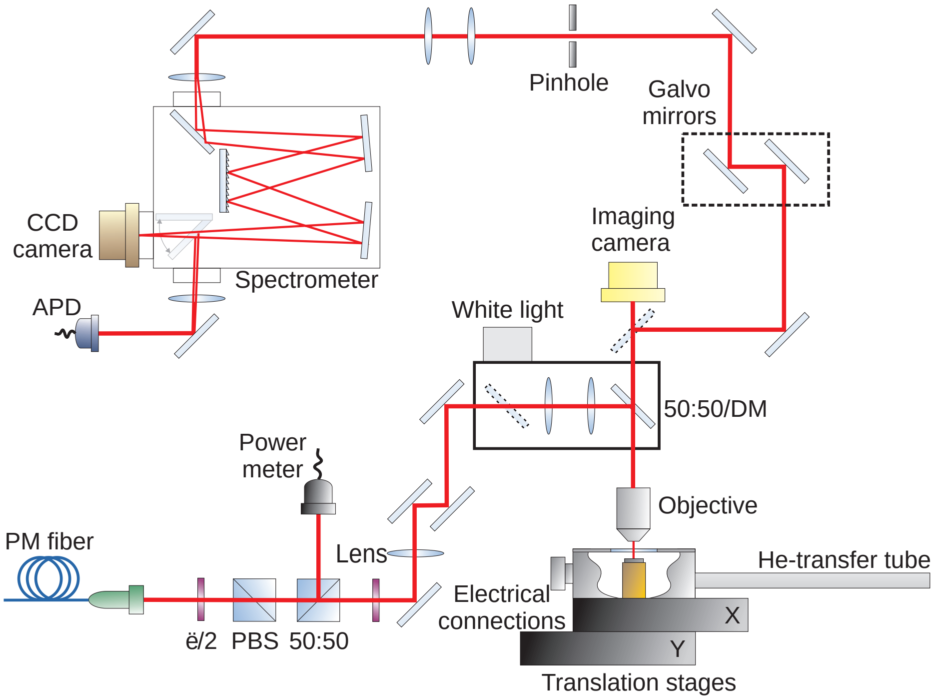

Figure 2.11: Schematics of the optical setup around the liquid-helium flow cryostat. The excitation laser light is brought by a PM fiber to a power control line (a $\lambda/2$ plate and a PBS). It is directed to a power meter though one port and to a microscope setup through the other port of a 50:50 beam splitter. The laser beam is reflected to the sample by a dichroic mirror (DM) or a 50:50 beam splitter. The photoluminescence from the sample is collected with an objective and directed to a free space collection path with a flip mirror shown as a dashed contour. An optional pinhole can be inserted into the collection path for spatial filtering of the signal. The photoluminescence is analyzed in a spectrometer and subsequently detected by a CCD camera or an avalanche photodiode for spectral and temporal measurements, respectively. A dashed box encasing two mirrors illustrates a galvanometer mirror system that can be introduced for a spatial scanning of the sample.

precision of 10 nm, and the focus is adjusted with a micrometer stage. A laser beam is brought from the laser table to a power control line consisting of a half-waveplate and a polarizing beam splitter, and fiber-coupled to the excitation arm of the optical head. Ten per cent of the power in this arm is guided to a power meter for control. Further, a 50:50 beam splitter is placed for the sample imaging on the imaging CCD camera. The sample is illuminated with a white light guided by an aluminum mirror mounted on a rail, which allows to insert the mirror into the collection path without disturbing the alignment of the optical head. A linear polarizer is inserted in the excitation path to clean the polarization of the incoming laser light. The sample is excited from the top through a microscope objective (Nikon CFI Plan Fluor ELWD 40x C) of NA = 0.6 with an adjustable working distance of 3.6–2.7 mm. The photoluminescence from the sample is collected through the same objective and filtered from the laser light by a half-wave plate and another linear polarizer. The emission signal is focused to an optical fiber and sent to a spectrometer

(Princeton Instruments Acton SP2500) with a resolution of 50 pm, and subsequently detected by a thermoelectrically cooled charge-coupled (CCD) camera (Princeton Instruments Pixis 100).

The optical setup accompanying the liquid-helium flow cryostat is sketched in Fig. 2.11. A laser beam is guided through a half-waveplate and a polarizing beam splitter, which compose a power control line. Part of the laser power is sent to a power meter via a 50:50 beam splitter to monitor the intensity incident on the sample. An additional half-waveplate is inserted after the beam splitter to set the polarization of the laser light. The laser beam is guided to an optical microscope setup (Olympus BXFM), where either a 90:10 beam splitter or a dichroic mirror (cutoff at 875 nm) is used to guide the light to a microscope objective (Nikon CFI E Plan Achromat 10x) of NA = 0.25 and focus on the sample. Additionally, an objective (Nikon CFI Plan Fluor ELWD 40x C) of NA = 0.6 has been used for some measurements. The microscope setup and the objective can be moved in the z-direction with a coarse and fine focus knob. In contrast to the optical setup around the closed-cycle cryostat, here the sample is not static and can be moved in the xy-plane within 100 nm accuracy by translation stages (Newport PM500-4L.100). The translation stages offer a long-range positioning allowing to image and measure at any position on the sample. The sample is imaged via a CCD camera by illuminating with a white light source. The setup can be easily switched between the imaging and measurement modes via flip mirrors, shown by the dashed lines in Fig. 2.11. The photoluminescence from the sample is guided to the free-space collection path and dispersed by a spectrometer (McPherson Model 207) with a resolution of 50 pm, where it is either detected as a spectrum by a CCD camera (Princeton Instruments TEA/CCD-1024-EM/1UV) or as a time-trace at a single frequency by a silicon avalanche photodiode. The collection path of the optical setup can be supplemented with a high-speed scanning galvanometer-mirror positioning system (Cambridge Technology 6240H/8340K). It consists of two optical mirrors mounted on galvanometer-controlled motors with sensors that detect the position of the mirrors. A servo loop is created by feeding the output signal of the sensor back to the drive electronics, allowing a very fast and precise mirror positioning. By scanning the two mirrors the collection spot is moved along two orthogonal axes, x' and y'. In such a way, while keeping the excitation spot fixed, a spatial map of the photoluminescence stemming from the sample can be acquired.

2.5 Effects of fabrication imperfections in a glide-plane ring cavity

Designing a PhC circuitry requires not only resonant photonic nanostructures, such as cavities or waveguides, but also low-loss optical interconnects or beam splitters, which can be based on ridge or PhC structures [32, 72, 73]. Introducing engineered structural defects or alterations of a PhC lattice of a waveguide allows to route photonic channels. Owing to symmetry of a triangular lattice, the PhC structures are bent by angles maintaining this symmetry, e.g., 60° [74, 75]. Bending a PhC waveguide by a random angle violates the symmetry of the slab and results in significant propagation losses of light. In principle, if the curvature of the waveguide is small, light can be adiabatically guided to propagate in an arbitrary direction. In practice, detrimental effects on the optical properties of the photonic nanostructures can be introduced due to the limited precision of the fabrication process.

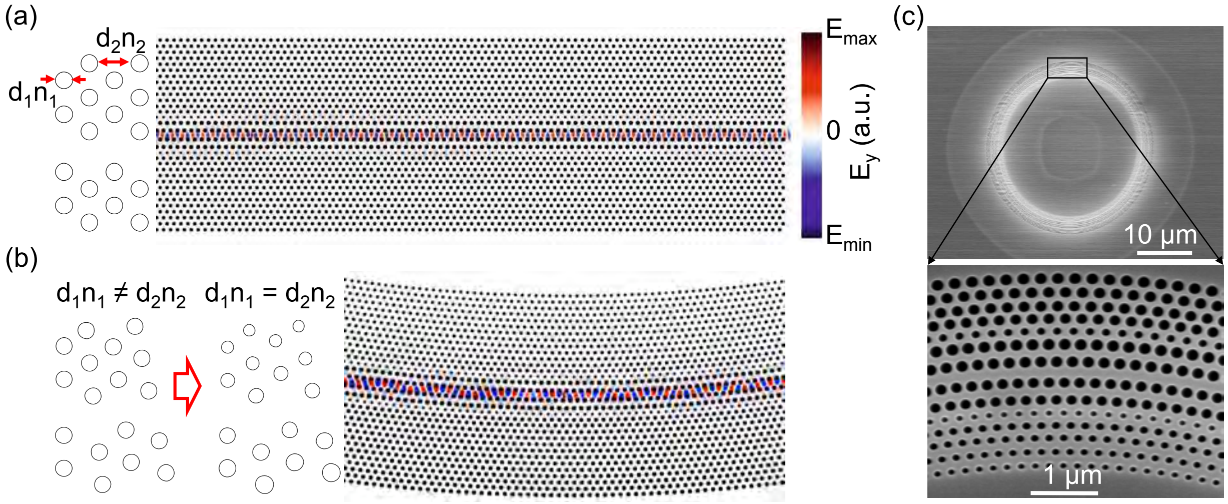

Figure 2.12: Design of the glide-plane ring cavity. Sketch and 2D finite-difference time-domain calculation of the electromagnetic-field intensity in a perfect glide-plane waveguide (a) and a section of a glide-plane ring cavity (b). Light propagates along the bent waveguide without significant leakage into the PhC. SEM image of the fabricated cavity and a magnified view of its segment (c).

PhC structures are very sensitive to disorder as they are mainly fabricated to operate at near-infrared wavelengths, meaning that their feature size and periodicity ranges from tens to few hundred of nanometers in GaAs. Size deviations of only several nanometers result in disorder and lower the reproducibility of the spectral properties of photonic structures [76]. Undesired disorder accommodates multiple scattering of photons resulting in localization of light, called Anderson localization [29, 77, 78].

In the following, localization in ring cavities obtained by an adiabatic rotation of a so-called glide-plane PhC waveguide is investigated. In such a structure, the line defect is introduced by a separation between two adjacent rows of holes, thus the glide-plane symmetry, see Fig. 2.12(a). The hole size in the first three rows around the defect is adjusted to optimize the mode dispersion for the slow-light effect. The most important feature of this structure, stemming from the glide-plane symmetry, is the emergence of two guided modes, an even and an odd one, which are frequency-degenerate at $k = \pi/a$. The coupling of these modes results in a high degree of circular polarization at the electric field maxima. The interaction of a single QD with the fundamental mode of the glide-plane waveguide results in a highly directional emission of single photons, as briefly discussed in Sec 2.6.

Figure 2.12(a) shows a sketch and a 2D finite-difference time-domain (FDTD) calculation of the electromagnetic-field intensity in a perfect glide-plane waveguide.[5] Light is propagating along the waveguide without significant leakage into the PhC, due to a wide photonic band gap. It is known that the band gap of a PhC is maximized when the optical paths of light in the air holes, $d_1 n_1$, and in the PhC slab, $d_2 n_2$, are equal [79]. Here d_1 (d_2) and n_1 (n_2) are the length of the unit cell

---

[5] The 2D finite-difference time-domain calculations were performed by Dr. David García.

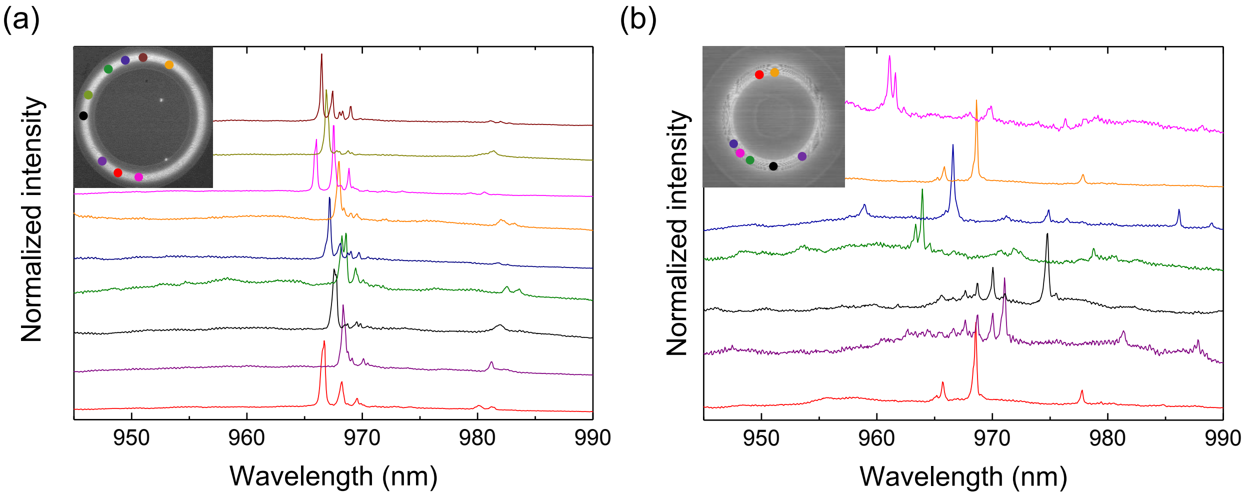

Figure 2.13: Light localization in glide-plane ring cavities. High power photoluminescence spectra acquired at different positions indicated by color coding on the ring structures with the radius $R = 60\,\mu\text{m}$ (a) and $R = 15\,\mu\text{m}$ (b). Localized modes are observed in a narrower wavelength interval for a smaller curvature cavity (a).

and the refractive index in air (GaAs), respectively. Rotating the glide-plane waveguide effectively stretches the PhC lattice and violates the equality of the optical paths, as shown in Fig. 2.12(b). Therefore, in the ring cavity design, the size of the air holes is scaled accordingly to restore this requirement and maintain the light confinement within the waveguide mode (Fig. 2.12(b)). Note that no further optimization of the structure design based on numerical simulations has been done. The structures are fabricated on a 160 nm-thick GaAs membrane with a layer of QDs embedded in the middle (the details on the wafer structure can be found in Appendix A). SEM images of the resulting structures are shown in Fig. 2.12(c).

Time-integrated photoluminescence spectroscopy is carried out on the fabricated sample placed in the liquid-helium flow cryostat, see Fig. 2.11. For all optical measurements the sample is cooled to 10 K. The sample is excited from the top with a continuous-wave laser tuned to 800 nm corresponding to pumping above the GaAs band. Light localization is found to occur in the ring cavities. By recording high-power photoluminescence spectra at several spatial positions, information about the distribution of the localized modes is obtained for the ring structures with the radius $R = 60\,\mu\text{m}$ and $R = 15\,\mu\text{m}$, shown in Fig. 2.13(a) and (b), respectively. Figure 2.14 summarizes the photoluminescence measurement results on four cavities with different radius of curvature: 15 µm, 20 µm, 29 µm and 60 µm. The mode quality factor $Q = \omega_c/\Delta\omega$ is evaluated from a Lorentzian fit of each mode. Correlations between Q and the radius of curvature, R, are not clearly resolved, however, Q factors larger than 6500 are obtained only for modes localized in the largest resonators with $R = 60\,\mu\text{m}$ and 29 µm, as seen in Fig. 2.14(a). On the other hand, the bandwidth of the localized modes depends strongly on R, see the inset of Fig. 2.14(b). For the cavity with $R = 60\,\mu\text{m}$, the localized modes are observed distributed within an interval of less than 5 nm, whereas modes spectrally separated by almost 30 nm localize in the cavity with 4 times larger

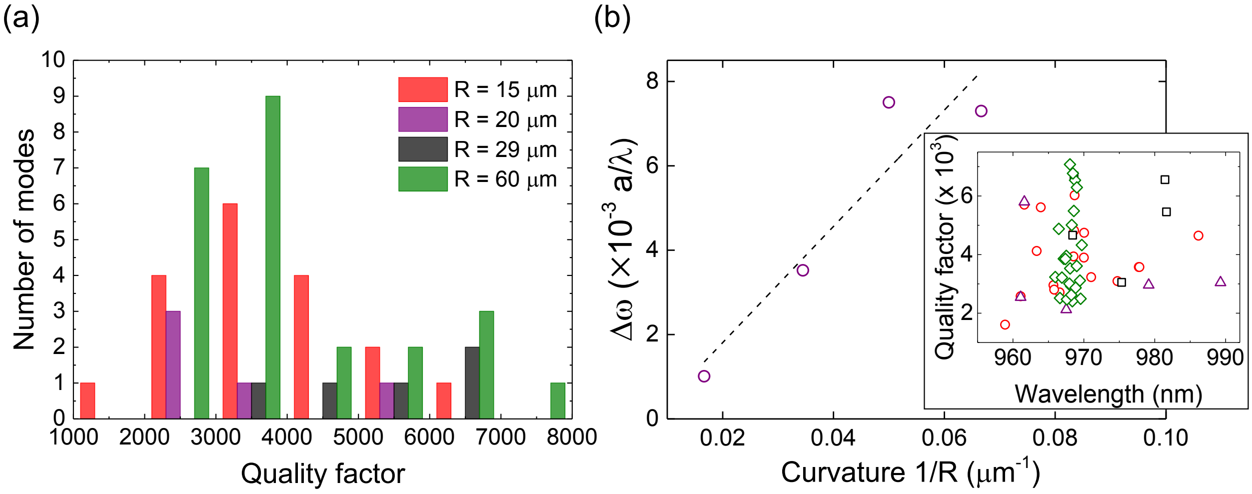

Figure 2.14: Quality factor distribution for the localized modes in ring cavities of different curvature. Statistical distribution of the quality factor (a) and its dependence on a central mode wavelength (inset in (b)) for the ring cavities with the radius $R = 15\,\mu\text{m}$, $20\,\mu\text{m}$, $29\,\mu\text{m}$ and $60\,\mu\text{m}$, indicated in red(circle), purple(triangle), black(square) and green(diamond), respectively. (b) The measured bandwidth of the localized mode distribution as a function of the resonator curvature $1/R$. The black dashed line is the guide to the eye.

curvature ($R = 15\,\mu\text{m}$). The curvature of the resonator, $1/R$, reflects by how much the waveguide unit cell is distorted — the larger the curvature, the more pronounced distortion of the triangular lattice. It is found that the spectral distribution of the localized modes becomes broader with the increasing ring curvature, see Fig. 2.14(b).

The observed effect resembles the Anderson localization, occurring in PhC structures due to an extrinsic disorder (added deliberately), e.g., variation in a hole size or position. These types of disorder have been extensively studied in PhC waveguides, and methods for quantifying it have been proposed [80–83]. It has been demonstrated that in PhC waveguides with small extrinsic disorder, that the bandwidth of the localized modes increases linearly with the amount of disorder [83]. In the case of the ring cavities with an intrinsic disorder, the bandwidth of the modal dispersion seems to correlate with the bending radius of the cavity. It suggests an independent effect caused by the distortion of the PhC lattice symmetry. The Anderson localization in PhC waveguides is studied in more detail in the next chapter.

2.6 Other experiments on the fabricated nanostructures

A brief overview of experiments conducted by other group members on several fabricated PhC devices is presented. The first work reported in Ref. [84] concerns optical nonlinearity at a single-photon level, which is one of the most desirable features for quantum information processing. Various scenarios employing the nonlinear interaction between photons and an emitter have been proposed for quantum gates implemented in cavity quantum electrodynamics (cavity-QED) or waveguide-based setups [85, 86]. Moreover, strong optical nonlinearity enables the experimen-

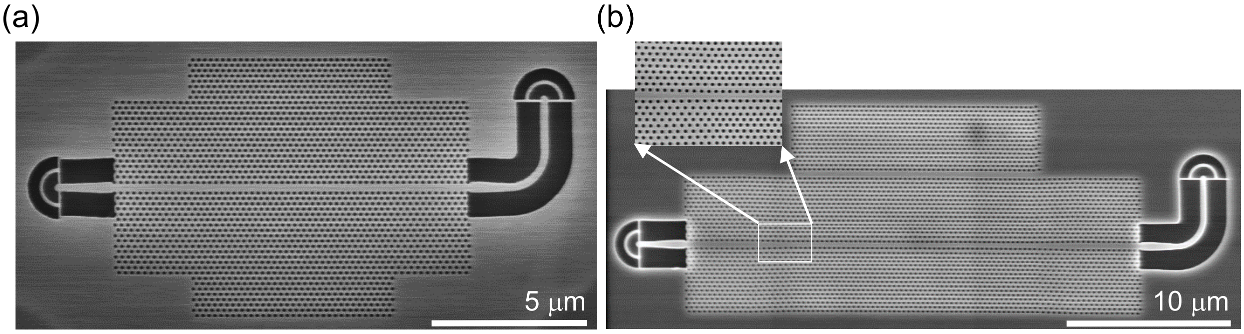

Figure 2.15: SEM images of the PhC devices fabricated for experiments on single-photon nonlinearity (a) and directional single-photon emission (b). Inset: magnified view of an intersection of the PhC waveguide sections with a horizontal-mirror (left) and glide-plane (right) symmetry.

tal realization of a single-photon transistor and a photodetector operating in a nondemolition fashion [87, 88].

It has been demonstrated that a QD embedded in a PhC waveguide can couple solely (> 98 %) to a guided mode, and thus facilitate a single-photon nonlinearity [31]. An SEM image of such a PhC waveguide used in Ref. [84] is shown in Fig. 2.15(a). More details on the sample structure are discussed in the next chapter. The excitation light is launched into a circular grating on the left and the transmitted light through the waveguide is collected via an outcoupler on the right. The latter grating is connected to the PhC slab via a ridge waveguide bent at a 90° angle, which allows to further reduce signal pollution with the laser light. Transmission measurements are conducted under resonant excitation of a QD sitting in a slow-light section in the middle of a waveguide. The QD modifies transmission spectrum of the PhC waveguide by preferentially reflecting the single-photon component while multi-photon components are transmitted. The power dependence of the transmission reveals the nonlinear effect at a level of less than one photon.

Another experiment on a PhC device fabricated using the recipes discussed in this chapter reveals directional emission of single photons generated by a QD sitting in a PhC waveguide with a glide-plane symmetry [89]. The sample design is analogous to the one used in the previously presented work, except that here the middle section is composed of a PhC waveguide with a glide-plane symmetry, see Fig. 2.15(b). As discussed above, the glide-plane symmetry supports the formation of a waveguide mode that is circularly polarized at the electric field maxima. When a QD, subjected to a strong magnetic field in the growth direction, interacts with such a mode, a so-called chiral behavior is induced. The two excitonic states of the opposite circular polarization created by the magnetic field couple to the counter-propagating modes of matching polarization, resulting to a directional single-photon emission. The sample is excited in the middle of the structure and the emission from the two spectrally split QD dipoles is collected via the outcoupling gratings on each side of the waveguide. The single-photon emission into a PhC waveguide with a directionality of 90 % is measured. This property can be exploited in constructing nonreciprocal elements of photonic circuits with highly directional photon routing.

2.7 Conclusions

To summarize, the processes for high-quality PhC device fabrication are described, including e-beam lithography, plasma etching, and deposition of robust ohmic contacts. We believe that the provided technical know-how will contribute to further development of GaAs processing for photonics and optoelectronics applications. By using the described recipes several types of photonic nanostructures are fabricated. The impact of the fabrication disorder on the bent PhC structures is investigated. Light localization is observed in the ring cavities formed by the angular rotation of a unit cell of a PhC waveguide. The bandwidth of the localized mode distribution is found to scale linearly with the cavity curvature. Finally, experiments on two different devices fabricated using the developed process and performed by other members of the Quantum Photonics group are overviewed.

Chapter 3

Electrical tuning of quantum dots across the photonic band edge

Electric-field-induced manipulation of quantized energy states of self-assembled QDs is a powerful tool for a number of quantum photonics experiments, e.g., cavity-QED, entangled photon pair generation, and Stark effect QD spectroscopy. The latter technique has been employed to obtain experimental information on the internal charge distribution within InGaAs QDs, which allowed to relate it with the material composition and the shape of the QD, and provided valuable guidelines to the theory [35]. Electric-field tuning of the fine-structure splitting below the QD linewidth has been demonstrated, leading to a biexciton-to-exciton-to-empty cascade proposed to emit polarization-entangled photon pairs [90, 91]. Moreover, deterministic control of the charge state of single QDs by means of the electric field, where an additional electron or a hole can be trapped by the QD potential, has been reported [92]. An electron spin in an optically active QD can be used as a qubit for quantum information processing [93]. Such qubits have to be initialized, manipulated, and read out before they are affected by decoherence processes, such as QD-transition energy jitter due to local electric or magnetic field fluctuations or phonon-induced dephasing. It has been recently shown that the application of the electric field can eliminate decoherence due to the electromagnetic noise [5]. Additionally, by tuning the properties of the QDs and their solid-state environment, the qubit operations can be performed at time scales preceding decoherence. The electric field allows reversible manipulation of the electrostatic environment, the charge state and the radiative dynamics of the QDs. A typical example of an implementation of these two concepts, serving for the cavity-QED experiments, is a QD tuned into resonance with a PhC cavity. Additionally, a number of interesting effects, e.g., modified Lamb shifts and the fractional emitter decay, are theoretically predicted to occur when the emitter is positioned in a region of a sharply varying LDOS [7, 94]. The possibility to probe such phenomena experimentally motivated the work presented in this chapter.

The theoretical model of the fractional decay relies on the existence of a sharp photonic band edge, as sketched in Fig. 3.1(a). An emitter placed within such a region interacts strongly with the electromagnetic field of the cutoff frequency. Such interaction leads to the formation of a superposition state, where the emitter neither fully decays nor remains in the excited state. A QD

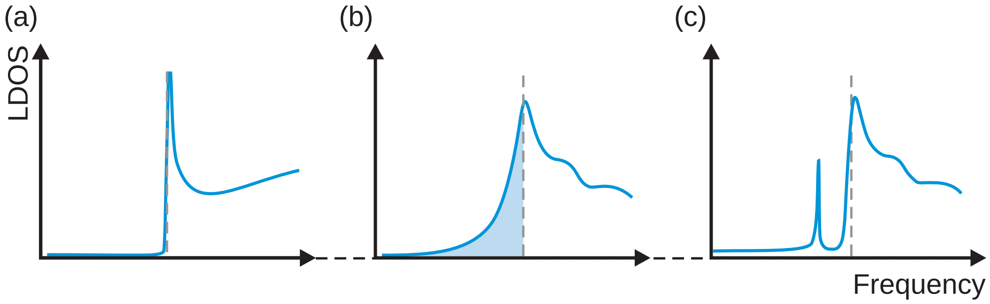

Figure 3.1: The LDOS dispersion in an ideal photonic structure (a), in a realistic structure, where the ensemble-average of the disorder-induced localized modes forms the Lifshitz tail, indicated by the blue shading (b), and in the case probed by a single measurement, where the individual Anderson-localized modes are resolved, as illustrated by the peak in the band gap (c). The gray dashed line is the guide to the eye for the cutoff frequency.

electrically tuned across the band edge of a PhC waveguide seems to be a perfect realization of the discussed physical system. In practice, however, the picture looks different due to the occurrence of light localization. In the PhC waveguides, the Anderson-localized modes distribute over a narrow spectral range around the cutoff frequency and form an optical equivalent of the Lifshitz tail, a characteristic DOS feature of the band gap in a disordered system, see Fig. 3.1(b) [82, 95, 96]. The Lifshitz tail is an ensemble property, whereas in a single measurement, the individual Anderson-localized modes occurring within the bandwidth of the Lifshitz tail are observed, as illustrated in Fig. 3.1(c). The ensemble average of such modes decays exponentially within the spatial extent of a sample with a characteristic length called the localization length, ξ. In the case of a 1D system, ξ is directly proportional to the mean free path l_e, which is defined as the distance between two scattering events [97]. Light localization in 1D occurs in the presence of disorder for the sample length L longer than l_e, or can be approximated to the condition of $L >> \xi$ [98]. The localization length of around 6 µm has been measured in 100 µm-long PhC waveguides with the intrinsic fabrication disorder [99]. This hints that in the samples shorter than ξ the probability of the Anderson localization should be low. Therefore, for the measurements of this work, 5 µm-long samples have been fabricated, where a significantly reduced probability of the light localization is expected. The very first measurements, however, have revealed that even in such short waveguides the photon multiple scattering leads to the light trapping in the random modes. These findings indicate a significant challenge in probing the fractional decay in real PhC waveguides and pinpoint to the intriguing effect of the Anderson localization in short 1D structures.

This chapter reports on the electrical QD tuning across the LDOS variations in a short PhC waveguide, where the LDOS landscape includes the Anderson-localized modes. First, the sample structure is presented along with the results on the initial optical characterization of the quantum-confined Stark effect on QDs. Time-resolved photoluminescence measurements are used to extract the radiative and nonradiative decay rates allowing to map out the LDOS dispersion within the spectral tuning range of several meV. Finally, the Anderson localization is studied at the band edge

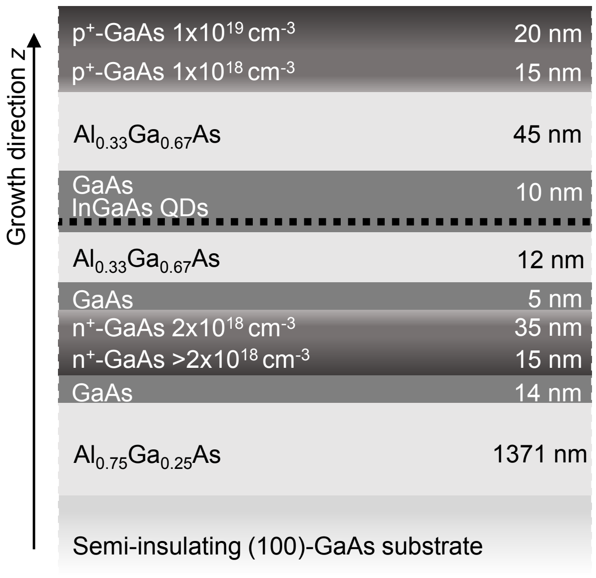

Figure 3.2: A layer structure of the wafer used for fabricating the PhC devices, where the intrinsic layer of a p-i-n diode encases InGaAs QDs.

of the photonic mode.

3.1 Quantum-confined Stark effect on quantum dots

In this section, the photoluminescence spectroscopy is employed to investigate the quantum-confined Stark effect. The measurements are conducted on a sample fabricated on a wafer that was grown at Ruhr University Bochum, Germany. The wafer consists of a 72 nm-thick intrinsic GaAs layer with QDs embedded two nanometers above the interface with the bottom AlGaAs barrier, see Fig. 3.2. The QD layer is isolated from the p- and n-type layers by the AlGaAs barriers to prevent charge-carrier escape from the QD at non-zero electric fields and tunnelling from the doped layers at forward bias. Such heterostructure design has been demonstrated to increase the tuning range dramatically compared to the case without barriers [100]. A mesa structure is defined by standard optical lithography and wet etching, and connected through the bottom n-type and top p-type ohmic contacts. The PhC nanostructures are etched into the mesa using the recipes described in Appendix A.

The sample under study consists of a photonic structure illustrated in Fig. 3.3. The waveguide contains a slow-light section (indicated by the blue shaded area) designed to have high group index n_g allowing for efficient light-matter interaction, surrounded by a fast-light section with low n_g. The fast-light section (red shading) is needed to efficiently extract light from the slow-section out through a circular Bragg grating [101], which is designed to couple the in-plane propagating mode perpendicularly out of plane. The dispersion curves of the main modes for each section are shown in Fig. 3.3(e). At the opposite side the waveguide is terminated by a PhC block, which is effectively a mirror and together with the grating forms a weak cavity giving rise to Fabry-Pérot resonances. All the waveguides studied in this section have a 5 µm-long slow-light section, a lattice constant

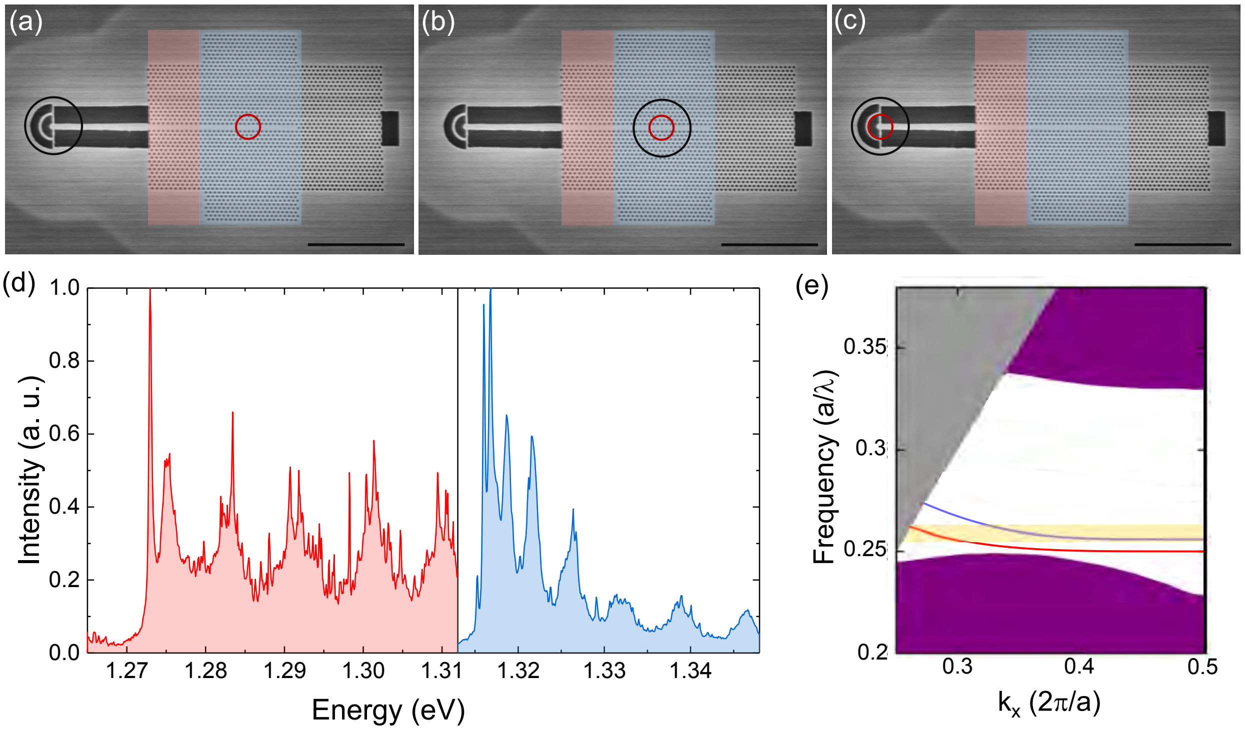

Figure 3.3: (a)–(c) Experimental configurations used in this work: the PhC waveguide is excited (red circle) into the slow-light section (blue shaded area), photoluminescence is collected from the circular grating (black circle) (a); the excitation and collection spot is focused on the slow-light section (b); the sample is excited in the grating outcoupler and the signal is collected from the same spot (c). The fast-light section is indicated by the red shaded area. The scale bar on the SEM images is 5 µm. (d) High-power photoluminescence spectrum from a PhC waveguide with two sections of different dispersion, shown in (e). The spectral region of the slow-light section is shown by the blue shading. The light within this region is allowed to propagate in both sections, whereas the longer wavelengths (red shading) couple only to the fast-light section and are reflected at the interface of the slow-fast regions. Clear Fabry-Pérot resonances are observed within the spectral range of the guided light. (e) Band structure of the sample, where the main band of the slow-light (fast-light) section is shown in blue (red). The yellow shaded region corresponds to the spectral region guided in both sections. The continuum of the guided modes is marked in purple, and the radiation modes are shown in gray.

$a = 252\,\text{nm}$, and a hole radius r varied from 70 to 74 nm.

The sample is placed into the liquid-helium flow cryostat and cooled to 10 K, as described in Chapter 2. Three experimental configurations used in this work are shown in Fig. 3.3. For the experiments discussed in this section, a picosecond-pulsed Ti:sapphire laser tuned to the wetting layer (844 nm) and focused to a 1.5 µm spot through a microscope objective of NA = 0.6 is used to excite the QDs. A dichroic mirror (cutoff at 875 nm) and polarization extinction is used to filter excitation laser. The photoluminescence is collected through a single-mode fiber, sent to a spectrometer with a resolution of 50 pm, and detected by a CCD camera or an avalanche photodiode. Figure 3.3(d) shows a high-power photoluminescence spectrum acquired from a waveguide with $a = 252\,\text{nm}$ and $r = 70\,\text{nm}$, when exciting the two sections of different dispersion. The cutoff for the slow-light section is around 1.315 eV (943 nm), and for the fast-light section around 1.272 eV (975 nm). In the following, only the band of the slow-light section is considered.

By varying the applied voltage the QD emission energy is tuned by the DC Stark effect, as given by [102]:

$$E = E_0 + pF + \beta F^2, \tag{3.1}$$

where E_0 is the exciton energy at $F = 0$, p is the dipole moment of the QD, and β is the polarizability, as defined in Chapter 1. Photoluminescence spectra of several QDs embedded in the unpatterned GaAs membrane versus the electric field are shown in Fig. 3.4(a). The QD emission is inhibited at small field values since the p-i-n diode turns on and the current starts running, thus the carriers are swept out of the QD. As the electric field is increased, the single QD lines shift according to Eq. (3.1). The photoluminescence stemming from the QDs is tuned by more than 4 meV before quenching due to tunnelling of the charge carriers at $F > 300\,\text{kV}\,\text{cm}^{-1}$. The tunnelling is the limiting factor of the QD tuning range and is determined mainly by the height of the potential barriers, as discussed later in this section.

By analysing the electric-field dependence of the QD emission energy, the polarity and polarizability of the QD can be determined. The central positions of two QD lines denoted as QD1 and QD2 are extracted from the measurements in Fig. 3.4(a) and accurately fitted with Eq. (3.1), see Fig. 3.4(b). The values of the permanent dipole moment $p = 4.6\,\mu\text{eV}\,\text{cm}\,\text{kV}^{-1}$ and $12.8\,\mu\text{eV}\,\text{cm}\,\text{kV}^{-1}$ corresponding to the electron-hole separation of $d_X = 0.5\,\text{Å}$ and 1.3 Å are obtained for QD1 and QD2, respectively. Accordingly, the polarizability $\beta = -0.08\,\mu\text{eVcm}^2/\text{kV}^2$ and $-0.092\,\mu\text{eVcm}^2/\text{kV}^2$ (or $-8\,\text{nm}^2/\text{V}$ and $-9.2\,\text{nm}^2/\text{V}$) is deduced for QD1 and QD2. The sign of the permanent dipole conveys information about the interdot charge distribution. In the convention adopted in this work, where the electric field is positive along the growth direction (oriented from the base to the apex of the QD), the positive p implies that the electron wavefunction is localized at the QD base, below the wavefunction of the hole at zero electric field. Such an electron-hole alignment is characteristic for the QDs with a gradient of In content increasing towards the apex [102]. The magnitude of the polarizability provides information about the QD shape, and particularly about its height [103, 104]. The extracted dipole moments and the values of β deduced from our measurements agree well with the values reported for similar QDs [100].

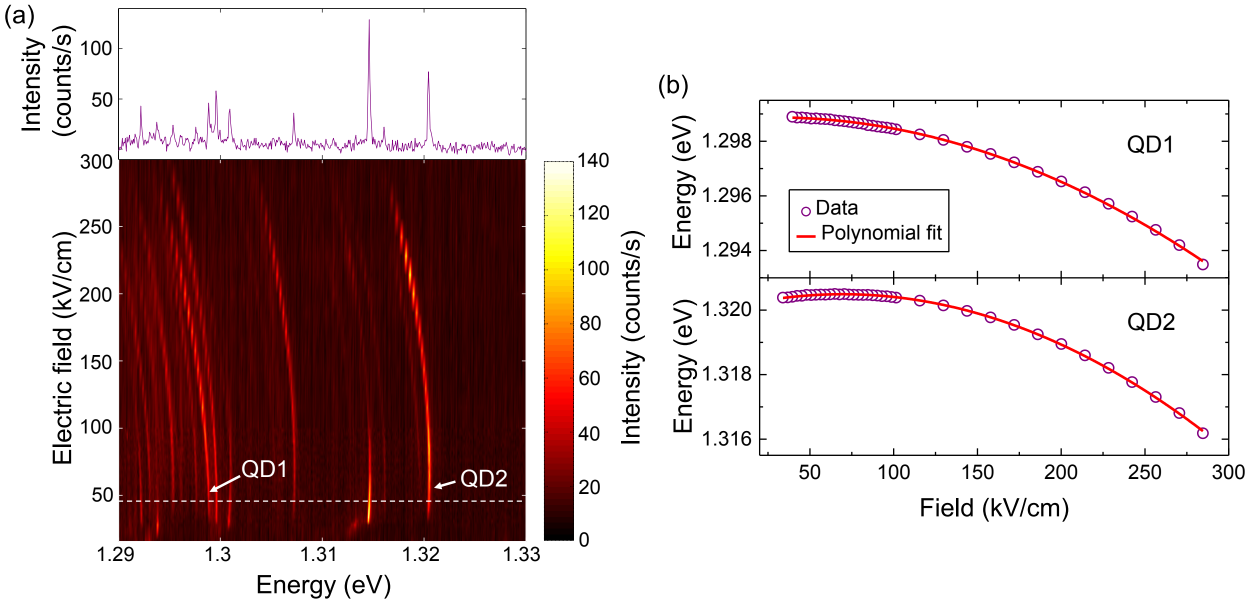

Figure 3.4: Electric-field tuning of the QD emission energy. (a) Typical photoluminescence map of single QD lines versus electric field is shown in the lower panel. The QDs are excited by pumping into the wetting layer with an excitation power of 50 nW. Upper panel: photoluminescence spectrum acquired at the electric field of around 45 kV cm^{-1} (indicated by the white dashed line) where the Stark shift is small. (b) Transition energies as a function of electric field for QD1 (upper panel) and QD2 (lower panel). The data is accurately fitted by Eq. (3.1) (red curves).

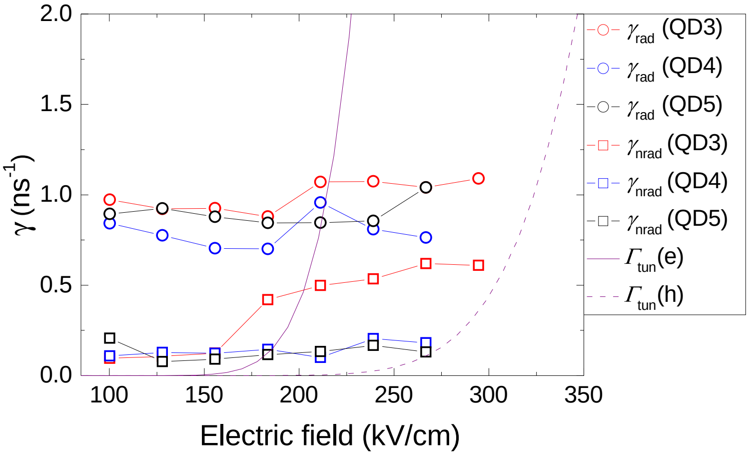

Figure 3.5: Electric-field dependence of the radiative (open circles) and nonradiative (open squares) decay rates extracted from the decay curves of the reference QDs, QD3 (red markers), QD4 (blue markers), and QD5 (black markers). Tunnelling rate of electrons (solid purple line) and holes (dashed purple line) are calculated using Eq. (3.2).

In the following, the influence of the electric field on the decay dynamics of QDs embedded in the circular grating is evaluated. Such a structure can be approximately treated as a homogeneous medium and allows to probe the QD decay not influenced by the LDOS effect in the waveguide. Transient photoluminescence of three reference QDs is measured in the configuration illustrated in Fig. 3.3(c). The data is fitted with a biexponential decay model. A measured background is accounted for in the fitting routine. The radiative and nonradiative decay rates are extracted for three QDs as a function of electric field, see Fig. 3.5. For the field values below 200 kV cm^{-1}, γ_{rad} stays roughly constant with an average of 0.9 ns^{-1} for all three QDs. For larger fields, the radiative decay rate of QD3 increases by 15 %, implying that the Purcell enhancement in the circular grating cannot be completely discounted. The nonradiative decay rate, on the other hand, is not influenced by the Purcell effect, but takes into account such effects like charge-carrier tunnelling or trapping at the surface states or defects. A significant increase of γ_{nrad} is found for QD3 as F exceeds 170 kV cm^{-1}, whereas for the other two QDs the nonradiative processes occur at a stable rate of around 0.13 ns^{-1} until 235 kV cm^{-1}. Similar values of γ_{nrad} have been measured in QDs away from the surfaces and without the electric field [105]. For the QDs subjected to large electric fields, the dominant nonradiative process is the tunnelling of the charge carriers. The tunnelling probability can be modelled using a 1D Wentzel-Kramers-Brillouin (WKB) approximation [33]. For a 1D confining potential of an effective width L, the carrier tunnelling rate Γ_{tun} through a triangular barrier with a height W is given by:

$$\Gamma_{\text{tun}} = \frac{\hbar\pi}{2m_{\text{eff}}L^2}\exp\left[\frac{-4\sqrt{2m_{\text{eff}}W^3}}{3\hbar eF}\right], \tag{3.2}$$

where m_{eff} is the effective mass of the particle in the tunnel barrier, and F is the electric field [102]. The tunnelling rates for the electron and the hole are calculated using the vertical confinement of the QD equal to $L = 3$ nm, see Fig. 3.5.[1] The electron escape occurs earlier owing to their lower effective mass. The calculated electron tunnelling rate exceeds 1 ns^{-1} just above 200 kV cm^{-1}, and points out to the nonradiative depopulation of QD3, consistent with the measurement of γ_{nrad}. Our data on the decay dynamics indicates that the QDs outside the PhC structures decay with a constant radiative rate while varying the applied bias. Therefore, the influence of the electric field can be neglected when interpreting γ_{rad}, measured in the PhC structures.

3.2 Quantum dots tuned in a photonic-crystal waveguide

In this section, the photoluminescence spectroscopy is performed on the QDs in the slow-light section of a PhC waveguide. The results on a single-QD tuning across the cutoff of the waveguide are discussed.

First, the saturation properties of the QDs are characterized by acquiring photoluminescence spectra as a function of excitation power. A single QD line indicated as QD6 is resolved in the spectrum acquired at an excitation power below a QD saturation, see Fig. 3.6. A high level of

---

[1] The height of the $Al_{0.33}Ga_{0.67}As$ potential barrier W for the electron and the hole of 0.255 eV and 0.160 eV, respectively, is calculated using a 1D Poisson solver [106].

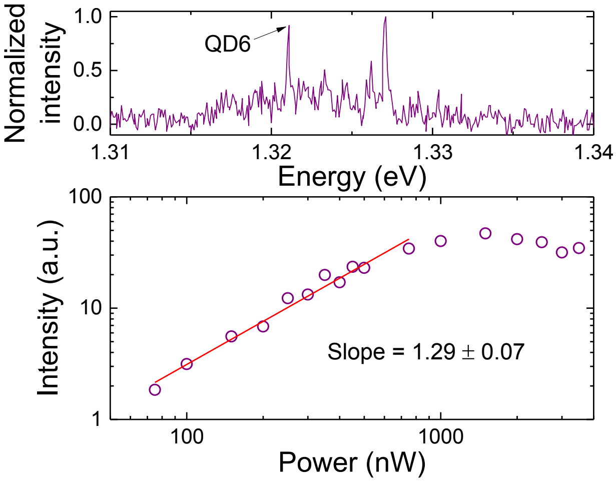

Figure 3.6: Power series on QD6 under the wetting-layer excitation at an electric field of 100 kV cm^{-1} (lower panel). The data is fitted with a power-law (red line) and a slope of 1.29 is obtained. The emission peak stemming from QD6 is indicated in the photoluminescence spectrum recorded at an excitation power of 100 nW (upper panel).

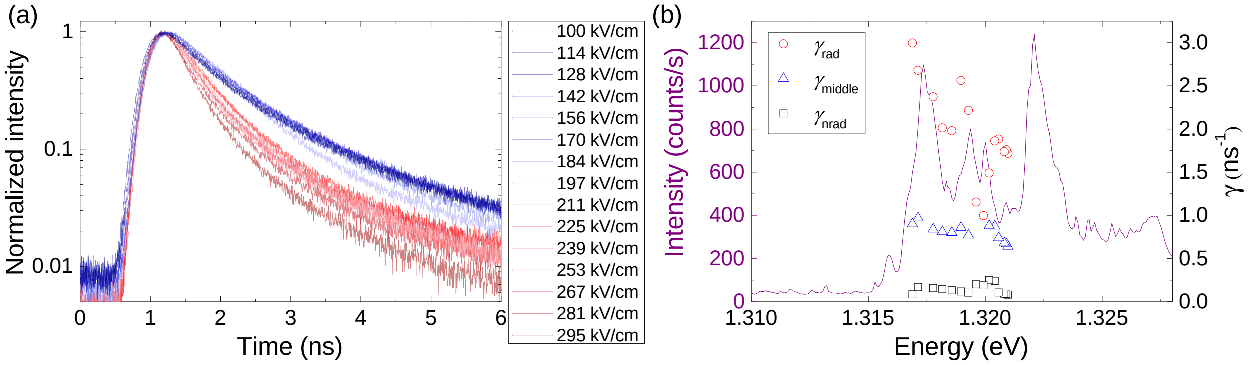

Figure 3.7: Electric-field dependence of the decay dynamics of QD6. (a) Time-resolved photoluminescence traces versus electric field, where increasing the electric field corresponds to redshifting of the QD energy. (b) The extracted radiative (γ_{rad} shown as red circles and γ_{middle} as blue triangles) and nonradiative (γ_{nrad} shown as black squares) decay rates and a photoluminescence spectrum of the PhC waveguide ($r = 72$ nm).

background photoluminescence indicates a rather high density of QDs within the focal spot. The sharp feature at 1.327 eV stems from the band edge of the waveguide mode, which is determined from the high-power photoluminescence spectrum. A saturation power of 750 nW is estimated for QD6 from the power series measurement, shown in the lower panel of Fig. 3.6. The data is fitted with a power-law dependence $\sim P^s$, and a slope of $s = 1.29$ is obtained, indicating that QD6 is populated by a neutral exciton X_0 or a trion (X^- or X^+). Time-resolved studies are performed at 20–30 % of the exciton saturation power and reveal a biexponential decay of the QD lines, therefore, QD6 is attributed to X_0 (trions decay single-exponentially due to the absence of the fine structure splitting). Similar characterization is conducted on all the measured QDs.

Further, the decay dynamics of QD6 are investigated when the QD is tuned towards the photonic band edge. At an electric field of $100\,\mathrm{kV\,cm^{-1}}$, the QD6 energy is around 6 meV below the band edge of the waveguide mode. By varying the applied voltage, the exciton energy is tuned closer to the band edge, and the photoluminescence decay is recorded as QD6 is shifted in energy, see Fig. 3.7(a). The acquired decay curves are fitted with a multiple-exponential decay model, accounting for a measured background. Figure 3.7(b) shows the extracted decay rates and a high-power spectrum of the PhC waveguide. The radiative rate γ_{rad} increases when moving to lower energies, thus mapping out the increasing LDOS towards the band edge. The spontaneous emission of QD6 occurs with a constant of $3.00 \pm 0.03\,\mathrm{ns^{-1}}$ at the mode maximum, corresponding to a Purcell enhancement of around 3 ($\gamma_0 = 0.9\,\mathrm{ns^{-1}}$ is used as a reference). The nonradiative decay does not change significantly within the tuning range (4.6 meV) and is around $0.13\,\mathrm{ns^{-1}}$, consistent with the data reported in Sec. 3.1.

As discussed in Chapter 1, the neutral exciton decay in a homogeneous medium is well described by the biexponential model. In a PhC waveguide the X_0 decay dynamics is altered since the two bright states of the QD couple to the waveguide mode at different rates. Consequently, the neutral exciton decay into the waveguide mode can be reproduced by a triple-exponential model: $\rho(t) = A_{\mathrm{f}}^{\mathrm{X}} \mathrm{e}^{-\gamma_{\mathrm{f}}^{\mathrm{X}} t} + A_{\mathrm{f}}^{\mathrm{Y}} \mathrm{e}^{-\gamma_{\mathrm{f}}^{\mathrm{Y}} t} + A_{\mathrm{s}} \mathrm{e}^{-\gamma_{\mathrm{s}} t}$. Assuming the same nonradiative rate $\gamma_{\mathrm{nrad}} = \gamma_{\mathrm{s}}$ for the two dipoles, the radiative rate γ_{rad} is determined for the dominant transition, whereas the decay constant of the other dipole is denoted as γ_{middle}. Note that at certain energies, the biexponential model suffices to reproduce the transient photoluminescence signal of the QD in Fig. 3.7(b). This could be explained by the suppression of one of the bright transitions of the QD, which couples weakly to the Fabry-Pérot cavities.

The photoluminescence of QD6 is strongly quenched due to carrier tunnelling at high electric fields before tuning it beyond the photonic band edge. With a view to investigate this spectral interval, other QDs are investigated which emit at energies closer to the cutoff frequency and can be tuned further into the band gap. Figure 3.8 shows time-resolved photoluminescence measurements on these QDs (QD7 and QD8). The radiative decay rate reduces more than two times for the measured QDs as their energy is shifted into the band gap. Interestingly, the Purcell enhancement of γ_{rad} persists even when the QDs emit at the energies 10 meV below the band edge. This is inferred from $\gamma_{\mathrm{rad}} = 1.42 \pm 0.02\,\mathrm{ns^{-1}}$ as measured for QD8, see Fig. 3.8(d). Since the expected suppression of the spontaneous emission below the cutoff is not observed, it indicates that the QD does not see a sharp band edge, where the LDOS would reduce dramatically within the spectral range smaller than the electrical tuning interval. As discussed in the introduction of this chapter, these findings advocate for the localized modes occurring below the cutoff, and to which the QDs couple. Even though in short samples the condition for the light localization should be not satisfied, our observations allow to investigate spatially small Anderson-localized modes, which have been predicted to occur near the photonic band edges [107]. The following section is dedicated to this study.

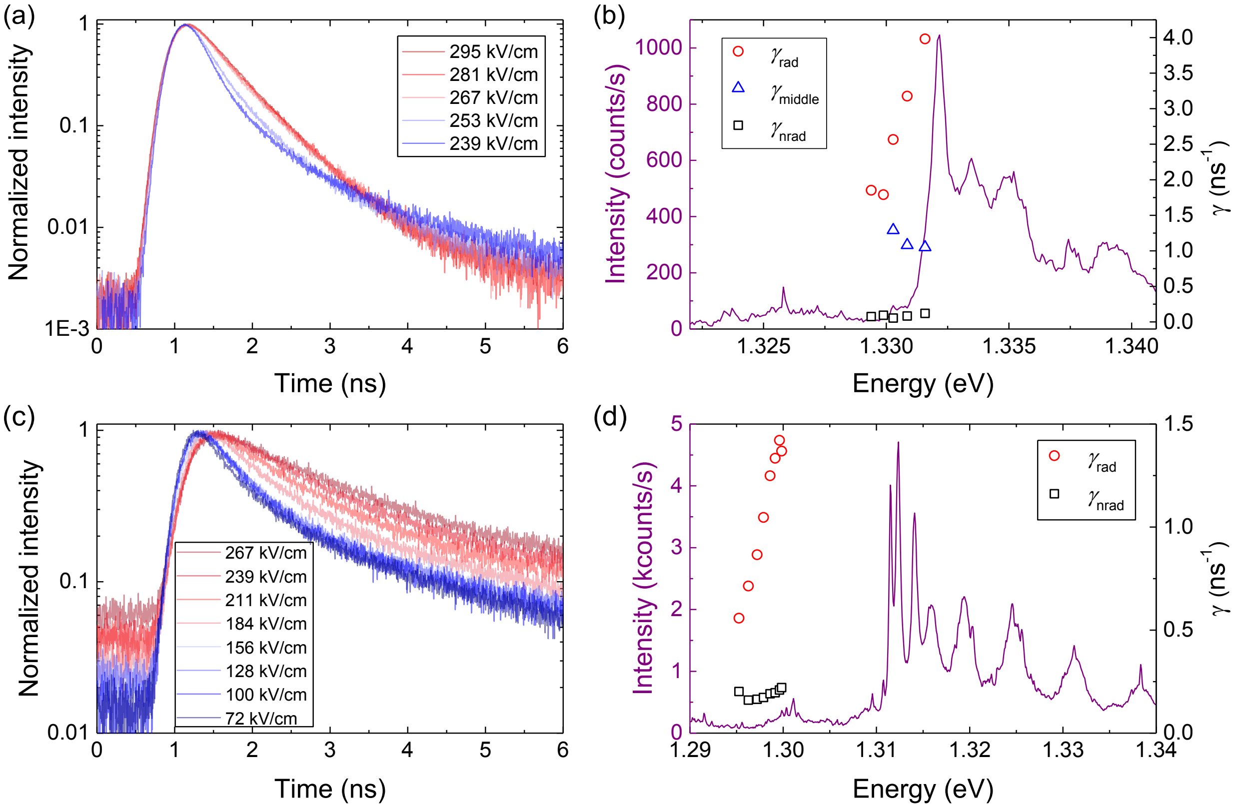

Figure 3.8: Electric-field dependence of the decay dynamics of QD7 (a, b) and QD8 (c, d). (a), (c) Decay curves as a function of electric field. (b), (d) The extracted radiative (γ_{rad} and γ_{middle}) and nonradiative (γ_{nrad}) rates, indicated by red circles, blue triangles, and black squares, respectively. A high-power spectrum of the PhC waveguide with $r = 74\,\mathrm{nm}$ in (b) and $r = 70\,\mathrm{nm}$ in (d) is shown in purple.

3.3 Light localization in short photonic-crystal waveguides

Disorder-induced light localization in PhC waveguides has been experimentally researched by several groups and has provided information on spatial and spectral extent of the localized modes [78, 80, 82, 83, 99, 108, 109]. Theoretical work on this phenomenon in 1D photonic systems has provided methods for quantifying the intrinsic and extrinsic disorder and investigating the properties of the localized modes [81, 96, 98, 110, 111]. Dispersive behavior of the localization length ξ has been demonstrated in a disordered PhC waveguide by measuring the ensemble-averaged extinction length, which is controlled by the dispersion of the PhC waveguide [112].

In a perfect waveguide, the DOS diverges at frequencies near the band edge. The group velocity of light depends on the DOS as $v_g \propto 1/\mathrm{DOS}$, and the slow-light effect is obtained at the high-DOS regime, which enhances light interaction with imperfections [114]. It has been shown that in the low-DOS regime, the localization length ξ scales as $1/\mathrm{DOS}^2$ [112]. Recently, it has been reported that the scaling law of $1/\mathrm{DOS}^2$ breaks down deep in the slow-light regime in the structures with

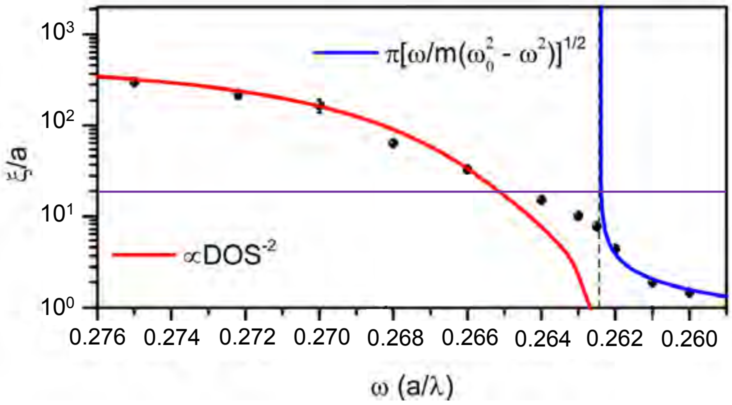

Figure 3.9: Dispersion of the localization length, ξ, in a PhC waveguide with $\sigma = 0.01a$ and $a = 260\,\mathrm{nm}$. The black dashed line indicates the band edge position of a perfect structure. Below this band edge in the low-DOS regime, the localization length ξ follows the scaling law of $1/\mathrm{DOS}^2$, whereas in the gap it depends on the effective mass of the photon. The length of the slow-light section (in $[a]$) in the investigated waveguides is indicated by the thin purple line. The black dots are the results of numerical simulations. The figure is the courtesy of Dr. David Garcia [113].

a flat dispersion, whereas the light localization in the band is governed by the DOS [107, 113]. It has been suggested that the formation of the localized modes at the band edge is governed by the effective mass of a photon. Figure 3.9 shows a modelled dispersion of ξ in a disordered PhC waveguide[2] illustrating the two discussed regimes [113]. The scaling with $1/\mathrm{DOS}^2$ is shown by the red solid curve and the blue solid curve depicts the frequency dependence of ξ, obtained from the effective-mass approximation applied to photonic lattices [115]. The obtained attenuation coefficient normalized to the lattice constant is expressed as $\xi/a = \pi[\omega/m(\omega_0^2 - \omega^2)]^{1/2}$, where a is the lattice constant, m is the photon effective mass, and ω_0 and ω is the frequency of the ideal and the disordered mode, respectively. This indicates that structures with a flat dispersion curve (large effective mass) have a very short localization length, and therefore, support the formation of spatially small localized modes. Additionally, this implies that the localized modes in the band are larger than the ones in the gap.

The sample investigated in this chapter contains PhC waveguides with a dispersion curve engineered to have essentially a flat band (the slow-light effect, see Fig. 3.3), and allows to experimentally probe the prediction that the localization length ξ is shorter for less dispersive waveguide modes. We note that the dispersion curve of the waveguide discussed in Fig. 3.9 is slightly different. The length of the slow-light section (5 µm) determines the upper limit for the localization length ξ, as depicted by the thin purple line in Fig. 3.9. An interesting frequency regime of the ξ dispersion can be probed in our sample, where, according to theory, it deviates from the $1/\mathrm{DOS}^2$ dependence.

To investigate the spatial and spectral extent of the localized modes, photoluminescence mea-

---

[2] A PhC waveguide with a triangular lattice of air holes with a radius $r = 0.29a$, where $a = 260\,\mathrm{nm}$ is a lattice constant, is considered. Disorder of $0.01a$ is introduced by displacing the holes in the first three rows around the waveguide defect by a random amount $\Delta\mathbf{r}$, where a standard deviation from the ideal position is $\sigma = \sqrt{\langle\Delta\mathbf{r}^2\rangle - \langle\Delta\mathbf{r}\rangle^2}$.

surements are conducted on PhC waveguides with no extrinsic disorder. During the optical measurements, a total electric field of around 100 kV/cm is applied on the sample. A continuous-wave Ti:sapphire laser beam tuned to a wavelength of 883 nm is used to excite the QDs in the slow-section of the waveguide, as illustrated in Fig. 3.10(a). The QDs distributed within the structure excite the Anderson-localized modes embedded deeply in the waveguide. For the position scans the sample is moved along the long axis of the waveguide by translation stages with a step size of 200 nm.

First, the band edge of four waveguides with different r/a is identified from the high-power spectra collected through the grating (the black line in Fig 3.10(c)–(f)). By keeping fixed a and increasing the hole radius r, a flatter dispersion relation can be engineered. Tightly localized modes present in each waveguide (the red line in Fig 3.10(c)–(f)) and located at frequencies just above the band edge are revealed in the photoluminescence spectra collected from the slow-light section. By measuring the intensity of the localized modes as a function of position along the slow-light section, see Fig. 3.10(g)–(j), a spatial extent, L_e, is estimated for each mode. It is defined as twice the distance over which the normalized photoluminescence intensity is reduced to 1/e, and is 1.4 µm, 1.7 µm, 2.4 µm, and 1.6 µm for waveguides with r/a equal to 0.286, 0. 278, 0.27, and 0.272, respectively. Although L_e does not correspond strictly to ξ, it represents a fair estimation, which indicates a stronger light confinement in 1D structures with a reduced dispersion curvature, as inferred from a systematic decrease of L_e with increasing r/a, see Fig. 3.10(c)–(e). The spatial extent of all the localized modes is 2–3 times smaller than the length of the slow-light section.

In order to link the results on the localized modes with the time-resolved measurements presented in Sec. 3.2, the decay dynamics of the QDs is probed in the experimental configuration shown in Fig. 3.3(b). In this way, the QDs, which do not couple well to the waveguide mode and their emission leaks out of plane, are investigated. The QD might instead couple to the localized mode, and this coupling can be inferred from the radiative decay rate. A high-power photoluminescence spectrum of the PhC waveguide reveals a localized mode 1 meV below the cutoff. For the time-resolved measurements the laser is operated in the pulsed regime and the excitation power is attenuated to 100 nW (around 20% of the saturation power for the measured QDs). The electric field is varied from 100 to 267 $\mathrm{kV\,cm^{-1}}$ to tune the QDs to lower energies. The measurements are performed on three QDs embedded in the slow-light section of the PhC waveguide and electrically tuned within different spectral regions. All three spectrally isolated QD lines are detected during the same time-integrated measurement, thus the alignment conditions are identical for all the measured QDs, i.e., the QDs are located within the same focal spot.

Figure 3.11 shows the measurement results on the three QDs. The spontaneous emission of the QD redshifted from the localized mode by 5 meV (QD9) is strongly suppressed by the photonic band gap, since γ_{rad} of only $0.12 \pm 0.001\,\mathrm{ns^{-1}}$ is measured. A single-exponential decay indicates a trion state of the QD. For the QD emitting just below the cutoff frequency (QD10), the decay dynamics is likely to be altered by the presence of the localized mode. The localized mode acts like a weak cavity and enhances the spontaneous emission rate of QD10, which should otherwise be suppressed by the photonic band gap. The radiative decay rate of QD10 is varied five times from

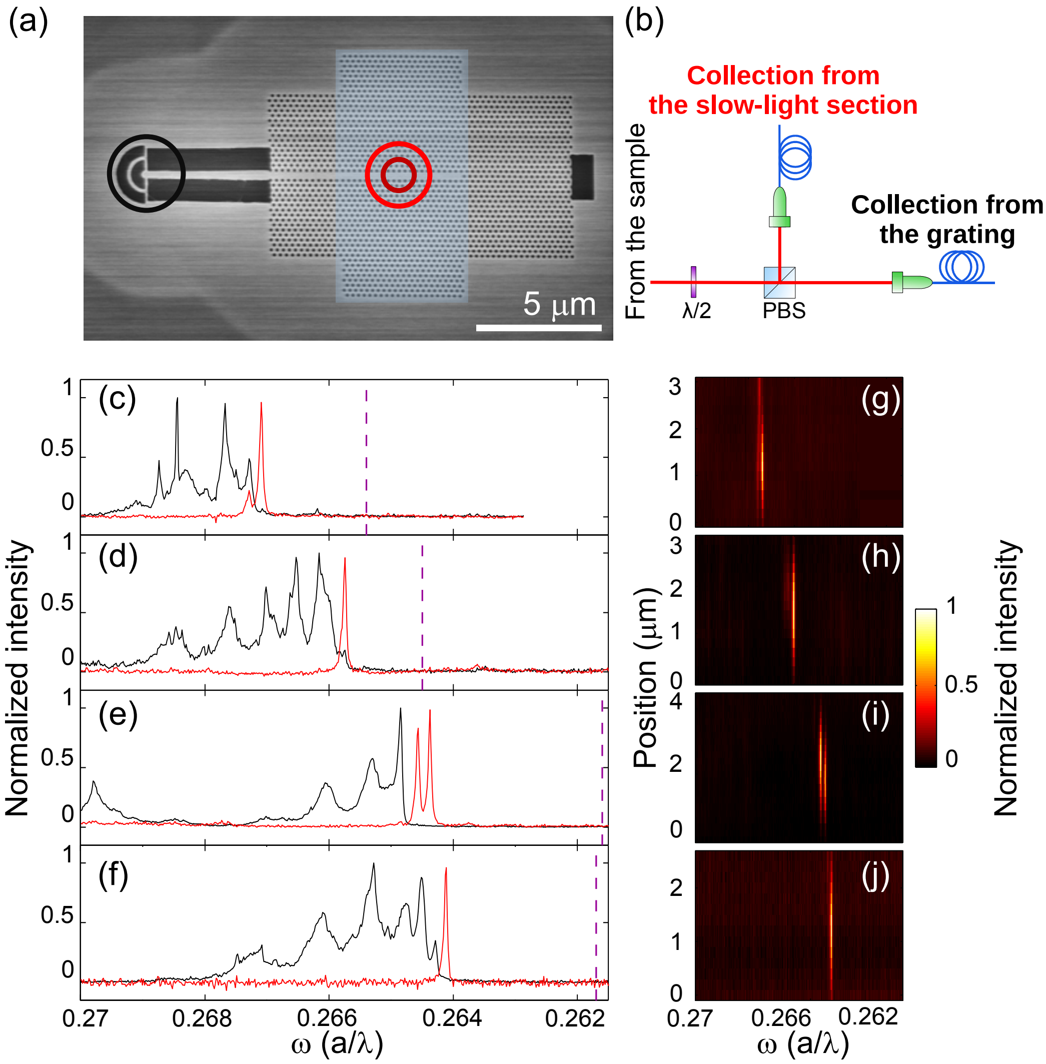

Figure 3.10: Localization of light measured in PhC waveguides with fabrication disorder. (a) SEM image of a PhC waveguide with a 5 μm-long slow-light section and parameters $r = 68$ nm and $a = 252$ nm. The sample is excited into the slow-light section (dark red circle), photoluminescence is collected either from the same spot (light red circle) or from the circular grating (black circle) with a setup shown in (b). High-power photoluminescence spectra of light coupled to a waveguide mode or localized in the slow-light section are shown by the black and red lines respectively for four waveguides with the following r and a: 72 nm and 252 nm (c), 70 nm and 252 nm (d), 68 nm and 252 nm (e), 68 nm and 250 nm (f). The cutoff frequency calculated with the parameters extracted from the SEM images is marked for each waveguide (purple dashed line). (g)–(j) Normalized photoluminescence intensity of the localized modes as a function of position along the slow-light section, corresponding to the data in (c)–(f).

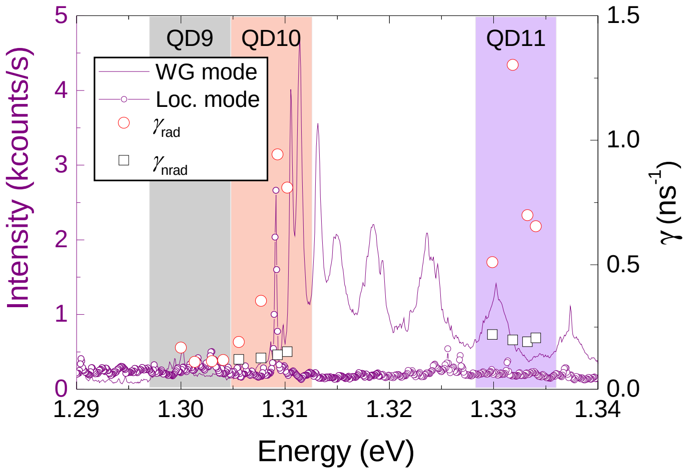

Figure 3.11: Photoluminescence decay rates of three QDs electrically tuned within different energy intervals (indicated by the color shaded areas) with respect to the photonic band edge. A high-power spectrum (solid purple line) of a PhC waveguide with $r = 70\,\text{nm}$ is acquired in the experimental configuration shown in Fig. 3.3(a). A localized mode (small purple circles) is observed just below the photonic band edge when using the experimental configuration illustrated in Fig. 3.3(b).

$0.94 \pm 0.03\,\text{ns}^{-1}$ just below the band edge to $0.19 \pm 0.02\,\text{ns}^{-1}$, as the QD is tuned away from the mode into the band gap. Another QD emitting at frequencies deep in the waveguide band (QD11) is observed, which seems to couple to the Fabry-Pérot cavities and decays with an enhanced radiative rate $\gamma_{\text{rad}} = 1.3 \pm 0.2\,\text{ns}^{-1}$. The detailed account of the measurement results on the reference QDs and all the QDs in the PhC waveguide is presented in Table 3.1.

Our findings on the decay dynamics of the QDs and the light localization in the PhC waveguides with a flat dispersion have important implications for the possibility to study the fractional emitter decay. In particular, the light localization occurring just below the cutoff frequency complicates the distinction of the waveguide band edge and is detrimental for the effects where a sharp band edge is required. It could be argued that using even shorter samples would further diminish the probability of the light localization, as ξ is reduced in the waveguides with a flat dispersion. In this work, for example, in the sample composed of 20 periods of the photonic crystal, the individual localized modes extending over 5–9 crystal periods are observed. Making such a short PhC might be challenging since at least a few crystal periods are required to build up the photonic band gap and the waveguide mode. Alternatively, in order to avoid the light localization, PhC waveguides with a large dispersion curvature where ξ is much longer could be used, but it is not desired due to a reduced Purcell enhancement at the mode edge. Completely eliminating the fabrication disorder, which gives rise to the localized modes, is unrealistic. The latter discussion and the results presented in this chapter pinpoint to the limitations of probing the extraordinary band-edge effects predicted assuming a perfect band edge in the theory, while it is not realized in practice. On the other hand, availability of strongly-confined localized modes could be of interest for experiments

Quantum dot	$\gamma_{\mathrm{rad}}^{\mathrm{max}}(\mathrm{ns}^{-1})$	$\gamma_{\mathrm{rad}}^{\mathrm{min}}(\mathrm{ns}^{-1})$	$\gamma_{\mathrm{nrad}}(\mathrm{ns}^{-1})$	$P_{\mathrm{F}}^{\mathrm{max}}$	P	$\Delta E(\mathrm{meV})$
	Reference quantum dots					
QD3	1.09 ± 0.02	0.88 ± 0.01	0.37 ± 0.01	–	–	3.8
QD4	1.00 ± 0.009	0.70 ± 0.004	0.14 ± 0.003	–	–	3.3
QD5	1.04 ± 0.007	0.85 ± 0.003	0.13 ± 0.004	–	–	2.7
	Collection from the grating					
QD6	3.00 ± 0.03	1.00 ± 0.005	0.14 ± 0.005	3.3	–	4.6
QD7	3.98 ± 0.01	1.79 ± 0.004	0.08 ± 0.003	4.4	2.2	2.7†
QD8	1.42 ± 0.02	0.56 ± 0.02	0.19 ± 0.002	1.6	2.5	4.6
	Collection from the slow-light section					
QD9	0.12 ± 0.001	0.11 ± 0.001	–	–	–	4.0
QD10	0.94 ± 0.03	0.19 ± 0.02	0.13 ± 0.01	–	4.9	4.6
QD11	1.3 ± 0.2	0.51 ± 0.04	0.2 ± 0.001	1.4	–	4.2

Table 3.1: Summary of data from photoluminescence measurements for the reference QDs and all the QDs electrically tuned in the PhC waveguide. The following parameters are extracted: maximum radiative decay rate $\gamma_{\mathrm{rad}}^{\mathrm{max}}$, minimum radiative decay rate $\gamma_{\mathrm{rad}}^{\mathrm{min}}$, nonradiative decay rate γ_{nrad}, maximum Purcell factor $P_{\mathrm{F}}^{\mathrm{max}} = \gamma_{\mathrm{rad}}^{\mathrm{max}}/\gamma_{\mathrm{rad}}^{\mathrm{ref}}$ with $\gamma_{\mathrm{rad}}^{\mathrm{ref}} = 0.9\,\mathrm{ns}^{-1}$, and electrical tuning range ΔE. The errors for the decay rates are extracted from the fitting. QD3–QD5 have been measured in the experimental configuration shown in Fig. 3.3(c), QD6–QD8 as shown in Fig. 3.3(a), and QD9–QD10 as shown in Fig. 3.3(b). A figure of merit, $P = \gamma_{\mathrm{rad}}^{\mathrm{max}}/\gamma_{\mathrm{rad}}^{\mathrm{min}}$, defining how much the spontaneous emission of the QD is suppressed by tuning it into the band gap, is extracted for QD7, QD8, and QD10. † QD7 has been tuned by the electric field within the interval of 239–295 kV cm^{-1}, which is three times smaller than for the other QDs.

on random lasing or cavity-QED [78, 81, 116].

3.4 Conclusions

To sum up, the photoluminescence results on the DC Stark tuning of self-assembled QDs embedded in PhC waveguides are presented. The electrical tuning range of around 4.6 meV is achieved. The time-resolved photoluminescence data of the emitters tuned across the LDOS variations in the waveguide is discussed. A three-fold reduction of the radiative decay rate is measured when shifting the QD from the waveguide mode into the photonic band gap. Nevertheless, the inhibition of the spontaneous emission of the QDs below the rate in a homogeneous medium is not observed even for the QDs tuned 1–2 meV into the band gap. The light localization is found to occur at the frequencies below the cutoff. The spatial extent of the individual Anderson-localized modes in PhC waveguides with a small dispersion curvature is investigated. Tightly localized modes are observed in waveguides with a flat dispersion, where the theory predicts the localization length ξ to scale inversely with a photon mass. A complex landscape of the localized modes around the cutoff pertains a challenge for studying subtle effects predicted to occur at the photonic band edge.

Chapter 4

Control of quantum-dot photoluminescence via electroelastic fields

The work presented in this chapter is motivated by the possibility of having quantum dots (QDs) with highly tunable optical properties in suspended semiconductor nanostructures. The optical properties of QDs can be efficiently tailored by applying external stress. Over the past decade, precise control of QD emission energy, fine structure splitting, and polarization of the emitted photons has been demonstrated by application of uniaxial and biaxial stress [117, 118]. Strain-induced tuning of QDs offers several advantages over other tuning techniques, which are briefly reviewed in the following. Rapid thermal annealing after QD growth, which induces a blueshift of the band gap up to a few hundred meV due to material intermixing (In and Ga), is nonreversible, unidirectional and hard to control precisely [119]. Wide-range tuning of the exciton energy can be achieved by temperature variation, however, such a method is slow and results in broadening of emission linewidth and photoluminescence quenching due to phonon-mediated nonradiative channels. Reversible and accurate control can be obtained by applying magnetic [23] and electric fields [120, 121]. Most of these techniques offer a tuning range restricted to several meV, whereas larger tuning bandwidth allowing to avoid cherry-picking of QDs is preferred for many experiments, such as generation of polarization-entangled photon pairs from biexcitonic cascade or tuning the QD resonance to a photonic channel [122–124]. An alternative heterostructure design has been proposed to enhance the electrical tuning range by embedding the QDs between AlGaAs barriers [90]. However, this approach is incompatible with the fabrication of PhC membranes, discussed in Chapter 2.

Strain-induced tailoring of QD properties does not pose stringent requirements on the material composition and is comparatively broadband (more than 20 meV). Importantly, it preserves the quality of QD emission and allows to recover the exciton spin degeneracy. Exciting results have already been demonstrated on entanglement of photon pairs emitted by optically and electrically excited single QDs [125, 126]. Recently, suppression of the fine structure splitting below the linewidth of the QD has been demonstrated for QDs in a GaAs membrane integrated onto a silicon chip with strain-inducing substrate [127]. It has been demonstrated that the strain transfer technique can be integrated with PhC nanostructures [128].

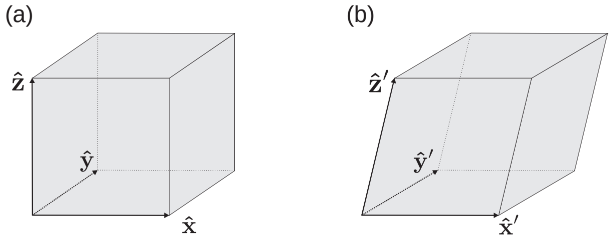

Figure 4.1: Schematics of a unit cell of an unstrained (a) and strained (b) crystal.

The goal of the present chapter is to examine geometrical anisotropy effects on strain induced in suspended semiconductor structures. In this work, for the first time the conventional techniques of nanofabrication of semiconductor substrates and flip-chip wafer transfer via a gold layer are combined to fabricate suspended microstructures that can be manipulated by means of external stress. The photoluminescence study of the QDs embedded in the fabricated structure reveals a bidirectional band-gap shift upon the application of compressive biaxial stress. Spatial distribution of strain in the structure is investigated numerically, and a uniaxial strain is found to dominate in particular regions of the sample. It has been suggested that the uniaxial strain is responsible for the bidirectional energy shift of QDs of a certain material composition [129]. Strain engineering by designing sample geometry is proposed for even more efficient tailoring of QD optical properties embedded in arbitrary photonic nanostructures.

The work presented in this chapter has been conducted during an external stay at the Institute for Integrative Nanosciences at the Leibniz Institute for Solid State and Materials Research in Dresden.

4.1 Introduction to the theory of continuum elasticity

A brief introduction of the theory of continuum elasticity and the strain Hamiltonian known as the Pikus-Bir Hamiltonian is given in this section [130, 131]. These concepts are used to describe the strain effects on the semiconductor band structure.

4.1.1 Stress and strain relation

In order to understand how a semiconductor is affected by external stress, it is important to learn the relation between stress and strain. Strain (ϵ) is a dimensionless parameter defining the relative deformation of a physical object. Stress (σ) is defined as force per unit area. Strain and stress are symmetric second-rank tensors, i.e., $\epsilon_{ij} = \epsilon_{ji}$ and $\sigma_{ij} = \sigma_{ji}$, where $i, j \in \{x, y, z\}$. Stress can be applied externally or it can be induced by interfacing lattice mismatched crystalline layers.

Figure 4.1(a) shows a 3D lattice defined by three unit vectors $\mathbf{\hat{x}}$, $\mathbf{\hat{y}}$, and $\mathbf{\hat{z}}$, which coincide with the lattice basis vectors in a cubic lattice. Under a small uniform deformation, both the orientation and length of the lattice vectors get distorted as shown in Fig. 4.1(b), which can be expressed in terms of the initial vectors as follows:

$$\hat{\mathbf{x}}' = (1+\epsilon_{xx})\hat{\mathbf{x}} + \epsilon_{xy}\hat{\mathbf{y}} + \epsilon_{xz}\hat{\mathbf{z}}, \tag{4.1a}$$

$$\hat{\mathbf{y}}' = \epsilon_{yx}\hat{\mathbf{x}} + (1+\epsilon_{yy})\hat{\mathbf{y}} + \epsilon_{yz}\hat{\mathbf{z}}, \tag{4.1b}$$

$$\hat{\mathbf{z}}' = \epsilon_{zx}\hat{\mathbf{x}} + \epsilon_{zy}\hat{\mathbf{y}} + (1+\epsilon_{zz})\hat{\mathbf{z}}. \tag{4.1c}$$

A set of strain coefficients ϵ_{ij} compose the strain tensor:

$$\bar{\bar{\epsilon}} = \begin{bmatrix} \epsilon_{xx} & \epsilon_{xy} & \epsilon_{xz} \\ \epsilon_{yx} & \epsilon_{yy} & \epsilon_{yz} \\ \epsilon_{zx} & \epsilon_{zy} & \epsilon_{zz} \end{bmatrix} \tag{4.2}$$

In the case of strain due to a lattice-mismatched growth, $\epsilon_{xx} = \epsilon_{yy} = \frac{a'-a_0}{a_0}$, were a_0 is the initial lattice constant of the crystal, a' is the lattice constant after the deformation.

Since the strain and the stress tensors are symmetric, six components are enough to define the strain in the linear-elastic regime. For small relative deformations, Hooke's law holds and the stress-strain relation for a cubic crystal can be expressed as follows:

$$\begin{bmatrix} \sigma_{xx} \\ \sigma_{yy} \\ \sigma_{zz} \\ \sigma_{xy} \\ \sigma_{yz} \\ \sigma_{zx} \end{bmatrix} = \begin{bmatrix} c_{11} & c_{12} & c_{12} & 0 & 0 & 0 \\ c_{12} & c_{11} & c_{12} & 0 & 0 & 0 \\ c_{12} & c_{12} & c_{11} & 0 & 0 & 0 \\ 0 & 0 & 0 & c_{44} & 0 & 0 \\ 0 & 0 & 0 & 0 & c_{44} & 0 \\ 0 & 0 & 0 & 0 & 0 & c_{44} \end{bmatrix} \begin{bmatrix} \epsilon_{xx} \\ \epsilon_{yy} \\ \epsilon_{zz} \\ 2\epsilon_{xy} \\ 2\epsilon_{yz} \\ 2\epsilon_{zx} \end{bmatrix} \tag{4.3}$$

The coefficients c_{ij} are the elements of the elastic stiffness tensor of a cubic crystal. The inverse Hooke's law can be written:

$$\begin{bmatrix} \epsilon_{xx} \\ \epsilon_{yy} \\ \epsilon_{zz} \\ 2\epsilon_{xy} \\ 2\epsilon_{yz} \\ 2\epsilon_{zx} \end{bmatrix} = \begin{bmatrix} s_{11} & s_{12} & s_{12} & 0 & 0 & 0 \\ s_{12} & s_{11} & s_{12} & 0 & 0 & 0 \\ s_{12} & s_{12} & s_{11} & 0 & 0 & 0 \\ 0 & 0 & 0 & s_{44} & 0 & 0 \\ 0 & 0 & 0 & 0 & s_{44} & 0 \\ 0 & 0 & 0 & 0 & 0 & s_{44} \end{bmatrix} \begin{bmatrix} \sigma_{xx} \\ \sigma_{yy} \\ \sigma_{zz} \\ \sigma_{xy} \\ \sigma_{yz} \\ \sigma_{zx} \end{bmatrix} \tag{4.4}$$

Here the coefficients s_{ij} compose the elastic compliance tensor of a cubic crystal. The coefficients of compliance and stiffness tensors are well known for many of diamond- and zinc-blende-type semiconductors [19].

In Eqs. (4.3) and (4.4) the stiffness and compliance tensors are evaluated for the stress applied along the [100], [010], and [001] directions. In order to correctly account for the elastic properties of an arbitrarily aligned crystal structure the stiffness tensor has to be evaluated along an arbitrary direction. For example, the stiffness tensor along the [110] direction is found by rotating the stiffness tensor defined in [100], [010], and [001] system by 45° about [001]:

$$C^{[110]} = \begin{bmatrix} \frac{c_{11}+c_{12}}{2}+c_{44} & \frac{c_{11}+c_{12}}{2}-c_{44} & c_{12} & 0 & 0 & 0 \\ \frac{c_{11}+c_{12}}{2}-c_{44} & \frac{c_{11}+c_{12}}{2}+c_{44} & c_{12} & 0 & 0 & 0 \\ c_{12} & c_{12} & c_{11} & 0 & 0 & 0 \\ 0 & 0 & 0 & c_{44} & 0 & 0 \\ 0 & 0 & 0 & 0 & c_{44} & 0 \\ 0 & 0 & 0 & 0 & 0 & \frac{c_{11}-c_{12}}{2} \end{bmatrix} \tag{4.5}$$

4.1.2 Deformation potentials and Pikus-Bir Hamiltonian

For a known strain tensor, the strain-induced energy shift can be calculated for the conduction and valence bands. The strain tensor can be decomposed into a diagonal matrix, which represents hydrostatic strain, and the shear-strain components. Hydrostatic strain corresponds to a fractional volume change, and shear strain is responsible for the symmetry distortion of the lattice. For crystals of cubic symmetry, hydrostatic strain does not break the symmetry, and thus energy levels are only shifted without breaking the band degeneracy. Shear strain reduces the unit-cell symmetry and lifts the degeneracy of the valence band, and leads to band mixing in particular cases. The conduction-band minimum of InAs occurs at the Γ point and is nondegenerate. It is only subjected to the hydrostatic strain shifts, defined by the respective deformation potential:

$$a_c^\Gamma = \frac{\mathrm{d}E_c^\Gamma}{\mathrm{d}\ln V}. \tag{4.6}$$

Here $\mathrm{d}\ln V$ accounts for the relative crystal volume change:

$$\mathrm{d}\ln V = \frac{\mathrm{d}V}{V} = \mathrm{Tr}(\epsilon) = \epsilon_{xx} + \epsilon_{yy} + \epsilon_{zz}. \tag{4.7}$$

The shift of the mean energy of the conduction band edge for small finite volume changes is given by:

$$\Delta E_c^\Gamma = a_c^\Gamma \,\mathrm{Tr}(\epsilon). \tag{4.8}$$

Similarly, the hydrostatic deformation potential for the valence band is defined as:

$$a_v = \frac{\mathrm{d}E_v}{\mathrm{d}\ln V}. \tag{4.9}$$

The valence band structure is more complicated than the conduction band because it has lower symmetry and is therefore affected by the shear strain. As a result, previously degenerate heavy-hole and light-hole bands split, and each band acquires energy shift with shear strain. The valence-band splitting is calculated by finding the eigenvalues of the Pikus-Bir Hamiltonian [132]. The latter is based on the $\mathbf{k}\cdot\mathbf{p}$ theory with the perturbation terms obtained via coordinate transformation, as shown in Ref. [130]. The total 6×6 strain Hamiltonian at the Brillouin zone center presented in the basis of six eigenstates of angular momentum $\left(|\frac{3}{2},\frac{3}{2}\rangle, |\frac{3}{2},\frac{1}{2}\rangle, |\frac{3}{2},-\frac{1}{2}\rangle, |\frac{3}{2},-\frac{3}{2}\rangle, |\frac{1}{2},\frac{1}{2}\rangle, |\frac{1}{2},-\frac{1}{2}\rangle\right)$ (see

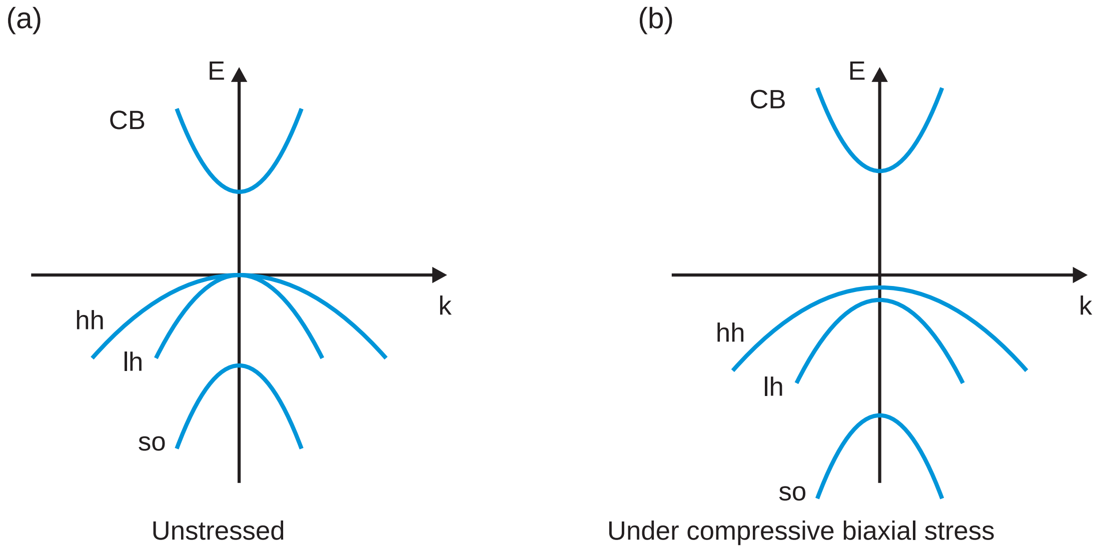

Figure 4.2: Sketch of the band diagram of a cubic semiconductor without strain (a) and under biaxial compressive strain (b). Biaxial strain lifts the degeneracy of the valence and widens the band gap as shown in (b).

Chapter 1) is given by:

$$H(k=0) = \begin{bmatrix} -P_\epsilon - Q_\epsilon & S_\epsilon & -R_\epsilon & 0 & \frac{1}{\sqrt{2}}S_\epsilon & \sqrt{2}R_\epsilon \\ S_\epsilon^* & -P_\epsilon + Q_\epsilon & 0 & -R_\epsilon & \sqrt{2}Q_\epsilon & -\sqrt{\frac{3}{2}}S_\epsilon \\ -R_\epsilon^* & 0 & -P_\epsilon + Q_\epsilon & -S_\epsilon & -\sqrt{\frac{3}{2}}S_\epsilon^* & -\sqrt{2}Q_\epsilon \\ 0 & -R_\epsilon^* & -S_\epsilon^* & -P_\epsilon - Q_\epsilon & \sqrt{2}R_\epsilon^* & \frac{1}{\sqrt{2}}S_\epsilon^* \\ \frac{1}{\sqrt{2}}S_\epsilon^* & \sqrt{2}Q_\epsilon & -\sqrt{\frac{3}{2}}S_\epsilon & \sqrt{2}R_\epsilon & -P_\epsilon - \Delta & 0 \\ -\sqrt{2}R_\epsilon^* & -\sqrt{\frac{3}{2}}S_\epsilon^* & -\sqrt{2}Q_\epsilon & \frac{1}{\sqrt{2}}S_\epsilon & 0 & -P_\epsilon - \Delta \end{bmatrix}, \tag{4.10}$$

where the elements of the matrix are given by:

$$P_\epsilon = a_v(\epsilon_{xx} + \epsilon_{yy} + \epsilon_{zz}), \tag{4.11a}$$

$$Q_\epsilon = -\frac{b}{2}(\epsilon_{xx} + \epsilon_{yy} - 2\epsilon_{zz}), \tag{4.11b}$$

$$R_\epsilon = \frac{\sqrt{3}}{2}b(\epsilon_{xx} - \epsilon_{yy}) - id\epsilon_{xy}, \tag{4.11c}$$

$$S_\epsilon = -d(\epsilon_{xz} - i\epsilon_{yz}). \tag{4.11d}$$

In Eqs. (4.11), b and d are the valence-band shear deformation potentials and Δ is the energy splitting due to the spin-orbit interaction, $\Delta = 0.38\,\mathrm{eV}$ for InAs [19].

In the particular case of equibiaxial strain ($\epsilon_{xx} = \epsilon_{yy}$) on the (001)-plane without shear strain ($\epsilon_{xy} = \epsilon_{yz} = \epsilon_{xz} = 0$), the Pikus-Bir Hamiltonian can be simplified. We get that $R_\epsilon = S_\epsilon = 0$, and the Pikus-Bir Hamiltonian can be easily diagonalized. The total energy shift of each doubly degenerate valence band are given by the following eigenvalues:

$$E_{v,hh} = -P_\epsilon - Q_\epsilon, \tag{4.12a}$$

$$E_{v,lh} = -P_\epsilon + \frac{1}{2}\left(Q_\epsilon - \Delta + \sqrt{\Delta^2 + 2\Delta Q_\epsilon + 9{Q_\epsilon}^2}\right), \tag{4.12b}$$

$$E_{v,so} = -P_\epsilon + \frac{1}{2}\left(Q_\epsilon - \Delta - \sqrt{\Delta^2 + 2\Delta Q_\epsilon + 9{Q_\epsilon}^2}\right). \tag{4.12c}$$

The relative energy shifts are defined with respect to the valence-band edge without strain.

Simplified schematics of the semiconductor band structure at the Γ point without stress and under compressive biaxial stress is shown in Fig. 4.2. When stress is applied, the conduction band is lifted up and the three valence bands are shifted down with respect to the valence band in the unstressed case. Consequently, the band gap is blueshifted. This convention will be used in the following sections where the results on strain tuning are discussed.

4.2 Fabrication of a suspended GaAs bridge sample

In this section, the fabrication steps of a sample with suspended GaAs bridges are discussed followed by a brief presentation of the piezoelectric crystal, which is used to induce strain on the GaAs sample.

4.2.1 Sample preparation

The structures are fabricated on a wafer grown at the Institute for Integrative Nanosciences, Dresden, Germany. The wafer consists of a sacrificial AlAs layer (100 nm), followed by a 200 nm-thick GaAs cap with a layer of QDs embedded in the middle. The sample is designed as several GaAs beam bridges integrated onto a piezoelectric crystal. The fabrication procedure consists of several steps, which are illustrated in Fig. 4.3. Firstly, a 200 nm-thick gold pattern is transferred on a gold-coated piezoelectric substrate (Fig. 4.3(a)) by means of UV lithography and electron-beam metal evaporation (the detailed recipe is presented in Appendix A). The gold pattern serves as abutment for the GaAs bridges. The same pattern is transferred on the GaAs wafer, see Fig. 4.3(b). The bridge design is imprinted on the wafer using UV lithography and dry plasma etching (Fig. 4.3(c)). These GaAs membranes are completely released from the wafer substrate via wet etching of the sacrificial AlAs layer with diluted hydrofluoric acid (Fig. 4.3(d)). After rinse in water and isopropyl alcohol the membranes fall loosely on the GaAs substrate. Next, the sample is flipped upside down and the gold patterns on the sample and the piezoelectric substrate are aligned onto each other with micrometer precision. By means of pressure and heating the GaAs membranes are detached from the semiconductor substrate and transferred onto the piezoelectric crystal, as illustrated in Fig. 4.3(e). Figure 4.4 shows an optical micrograph and SEM image of the final sample. The GaAs membrane with free-hanging bridges rests on the gold supports. This gold layer also serves as a top contact for the piezoelectric crystal, which is the strain-inducing substrate and is discussed in more detail next.

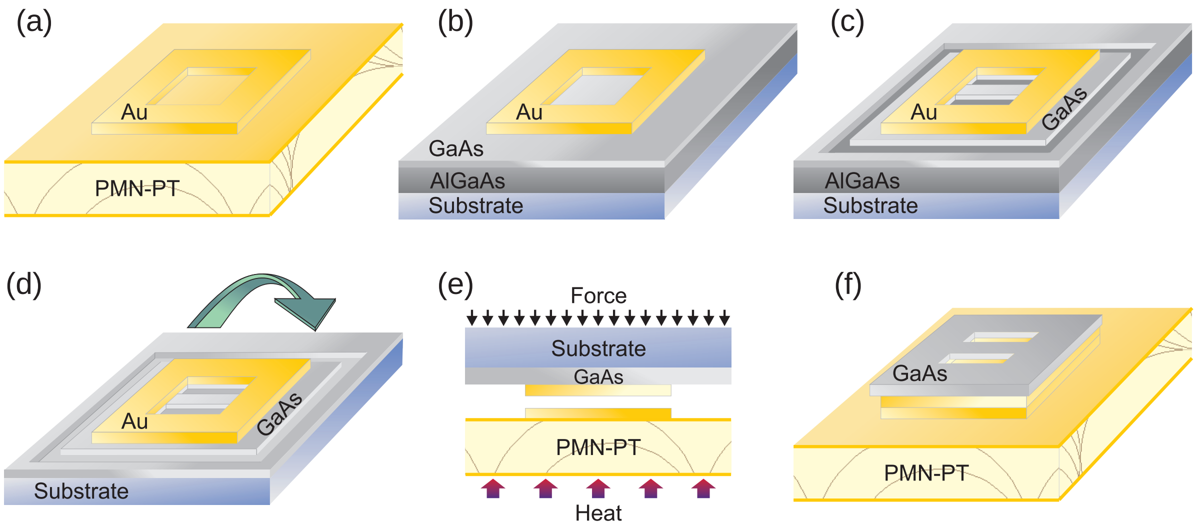

Figure 4.3: Illustration of the fabrication process of suspended GaAs bridges on a piezoelectric substrate. (a) A window-shaped pattern is transferred by depositing 200 nm of gold on a gold-coated PMN-PT slab. (b) The matching pattern is transferred on a GaAs wafer. (c) By means of UV lithography and dry plasma etching the bridge is fabricated on GaAs. (d) The sacrificial AlAs layer is removed with dilute HF and the GaAs membranes fall freely on the substrate. (e) The sample is flipped upside down and aligned to the patterned PMN-PT slab for thermal transfer. (f) Finally, the GaAs bridges suspended above the window-shaped pattern on the piezoelectric crystal are obtained.

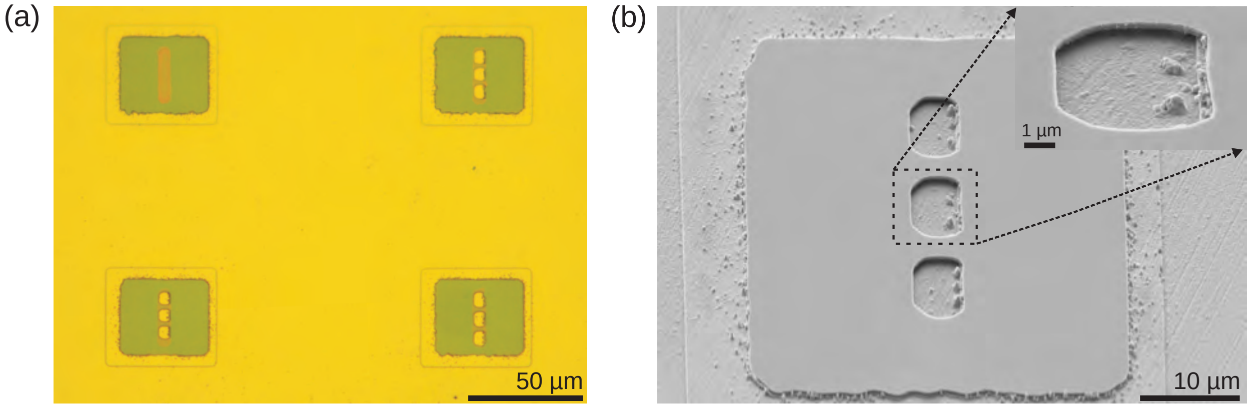

Figure 4.4: (a) Optical micrograph of the sample transferred onto the patterned PMN-PT crystal. (b) SEM image of the same sample indicating the air gap between the GaAs bridge and the piezoelectric substrate.

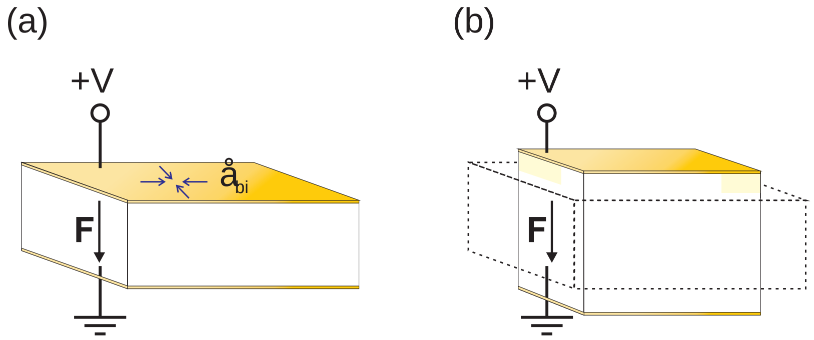

Figure 4.5: Illustration of the piezoelectric effect in the PMN-PT crystal. The sign convention is such that a positive electric field **F**, applied to the crystal, as shown in (a), induces an expansion of the PMN-PT along the field direction, as illustrated in (b). Applying the electric field in the opposite direction reverses the process and the induced biaxial strain.

4.2.2 Piezoelectric crystal (PMN-PT)

Lead magnesium niobate-lead titanate (PMN-PT, $\mathrm{Pb(Mg_{1/3}Nb_{2/3})O_3]_{1-x} - [PbTiO_3]_x}$, where x is the relative amount of lead titanate) is used as a substrate to transfer strain to semiconductor membranes with embedded QDs. This piezoelectric material possesses superior piezoelectric properties compared to conventional piezoceramics such as PZT (lead zinc titanate) [133]. This is because PMN-PT is a monocrystalline material allowing for nearly perfect domain alignment in an electric field.

At room temperature, the PMN-PT crystal has no net polarization. The temperature at which the domains form is called the Curie temperature and depends on the fraction of lead titanate x, but is always below 130 °C [134, 135]. Therefore, before the first use the PMN-PT crystal has to be poled along a certain crystal direction with an electric field larger than the coercive field above which the domains polarize in a reverse direction. The domains align along the direction of the electric field and remain polarized until the temperature exceeds the Curie temperature. During the operation, it is important to apply the electric fields not exceeding the value at which the polarization reverses. Above this point the crystal might crack because of strain approaching the physical limit. Moreover, applying too strong electric fields leads to undesirable hysteresis effects. The coercive field in the PMN-PT crystal decreases exponentially with increasing temperature [134]. It is particularly convenient for low-temperature applications since it widens the interval of applicable voltage, and thus the induced strain.

The PMN-PT substrates used in this experiment are poled along the [001] direction by a positive electric field of around 15 kV/cm, as shown in Fig. 4.5. In principle, the direction of the poling does not matter due to the symmetry of the crystal along [001]. The poling field is kept on during the cool-down process to ensure the domain alignment at low temperature.

The strain transfer from the piezoelectric substrate to the semiconductor membrane depends on the quality of the mechanical contact between them. Ideally, the strain should relax solely into the

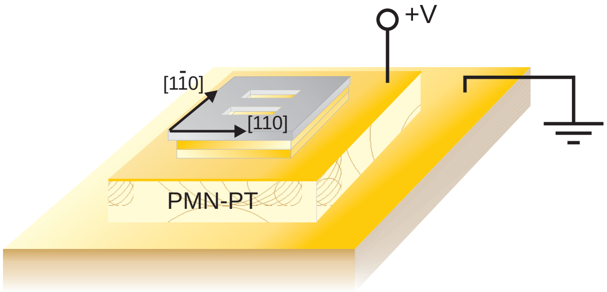

Figure 4.6: Sketch of the GaAs bridge orientation with respect to the crystallographic axes and the PMN-PT crystal. The bridge is aligned either along [110], as shown in the figure, or [1$\bar{1}$0].

semiconductor membrane, but not into the transfer material. Therefore, it is preferred to use hard materials such as a layer of gold. The orientation of the semiconductor sample with respect to the crystallographic axes of the piezoelectric crystal is important for correctly evaluating the behavior of the semiconductor under applied stress. For this purpose, the GaAs membranes fabricated in this work are mounted on the piezoelectric substrate such that the [110] and [1$\bar{1}$0] directions of GaAs are roughly aligned to the cut axes of the PMN-PT crystal, see Fig. 4.6.

The prepared sample is mounted with the silver glue on a leadless chip carrier (LCC), which has a gold-coated surface. This gold layer serves as the back contact for the PMN-PT crystal. The top surface of the PMN-PT substrate is wedge bonded with an aluminum wire to one of the contact pads on the LCC in order to be able to apply a bias. The sample is fixed on the chip carrier and mounted on a copper cold finger. To ensure good thermal contact the back side of the LCC is greased with n-grease and fastened to the cold finger with a couple of screws.

4.3 Strain tuning of quantum dots in suspended GaAs bridges

In this section, the results on strain tuning of self-assembled InAs/GaAs QDs are presented. A total of 29 QDs are measured by means of time-integrated photoluminescence spectroscopy.

4.3.1 Experimental conditions

Optical measurements are performed on the sample in a liquid-helium flow cryostat cooled to the temperature of several Kelvin. The experimental setup is similar to the one described in Chapter 2. A continuous-wave laser beam tuned to 515 nm (corresponding to excitation above the GaAs band gap) is focused on the sample through an objective of NA = 0.65 resulting into a spot of around 1.5 µm. The same objective is used to collect the photoluminescence from the sample, which is then guided to the spectrometer equipped with a 1200 Grooves/mm grating. A long-pass (850 nm) filter is placed in the collection path to filter the excitation laser. The objective and part of the collection optics are mounted on two stacked computer-controlled nanopositioning stages allowing for the movement in the xy-plane.

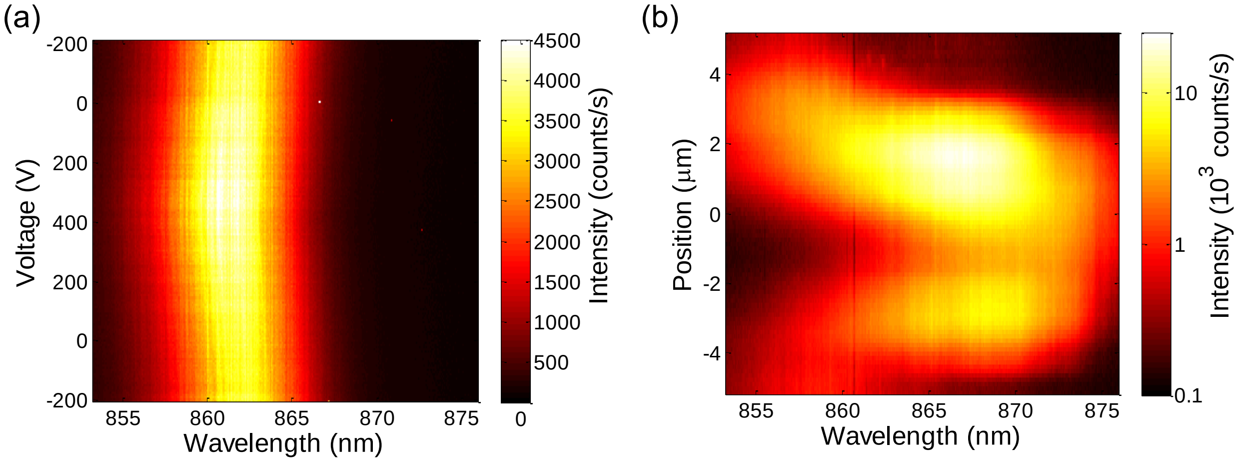

Figure 4.7: Strain-tuning of the wetting layer photoluminescence. (a) A colormap of the wetting layer signal as a function of voltage applied on the strain-inducing layer. (b) Photoluminescence of the wetting layer recorded at different spatial positions with respect to the center of the suspended bridge (position at 0 μm).

4.3.2 Photoluminescence of the wetting layer

Observing the photoluminescence of bulk GaAs or wetting layer is usually a convenient test of the optical setup and of the electrical connections to the piezoelectric substrate. In our experiment, the wetting-layer emission is centered roughly at 862 nm in the unstrained case. The spectral tuning range of the wetting-layer emission is a rough measure of the amount of strain induced in the GaAs sample. In order to estimate the quality of strain transfer, the photoluminescence from the wetting layer is recorded as a function of voltage applied to the PMN-PT crystal, see Fig. 4.7(a). According to the convention presented in Sec. 4.2.2, the emission from the wetting layer is blueshifted for voltages from -200 to 400 V in steps of 7.5 V. The tuning is reversible as illustrated by a flip of the tuning direction at 400 V. The spectral shift experiences little hysteresis as is shown later for QDs. The broad wetting-layer signal hides such detailed features. It can be estimated that within the applied voltage window the spectral position of the wetting-layer emission can be tuned by one nanometer.

The emission energy of the wetting layer depends on position, see Fig. 4.7(b). When the excitation spot is ±4 μm away from the bridge the wetting-layer signal is centered around 857 nm, and is redshifted to 866 nm at the center of the bridge. This indicates that there is a strain gradient along the bridge. This means that the spatial strain profile is strongly influenced by the geometry of the suspended structure. It is clear from Fig. 4.7 that the geometry-induced strain is several times larger than that of the piezoelectric substrate. Combining the two mechanisms could be used to significantly enhance the tuning range of quantum emitters.

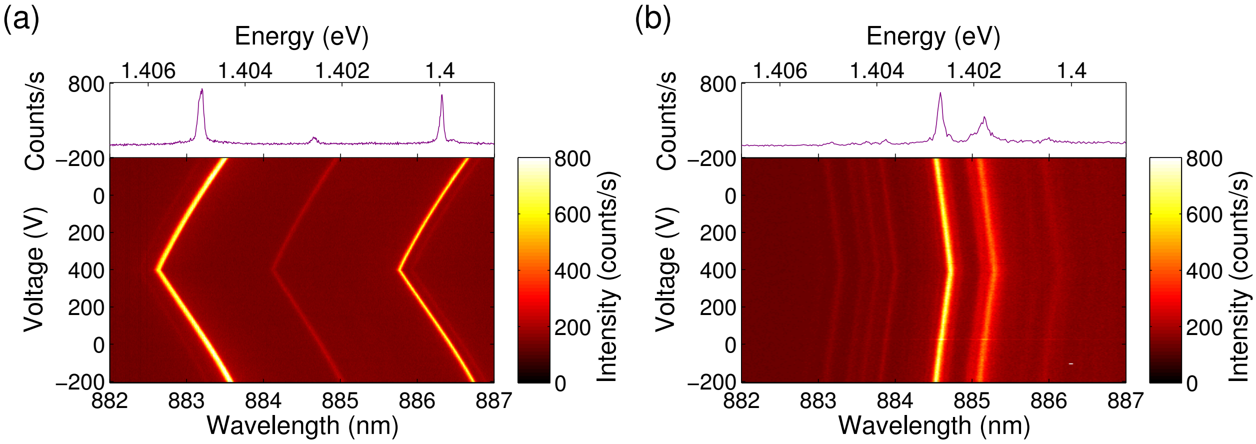

Figure 4.8: Strain-tuning of the emission energy of the QDs located at different positions on the sample. (a) Photoluminescence map of QD1 located on the membrane as a function of voltage. The QD emission blueshifts due to compressive strain. (b) Photoluminescence map of QD2 located on the suspended GaAs bridge. The QD emission redshifts with compressive strain. The spectra shown in the upper panels of (a) and (b) are taken at 0 V.

4.3.3 Photoluminescence of quantum dots

It has been shown that the suspended structure attached to the strain-inducing substrate possesses an inhomogeneous strain distribution with an enhancement of strain in the middle of the structure. In the following it is shown how strain influences the QD emission.

The photoluminescence measurements are taken first in the prestrained situation, where the tensile strain (negative piezovoltage) is exerted on the sample. As the voltage across the substrate is increased, the prestrain is relaxed and the sample is compressively strained. Two bright QD lines are observed in the emission spectra positioned at 882.7 nm and 885.8 nm at 0 V, see Fig. 4.8. A dim line centered at 884.1 nm is a QD further away from the collection spot. The QD1 transition energy is blueshifted by 1.48 meV (0.95 nm), which is expected from the band edge behavior discussed in Sec. 4.1.2. Similar results are obtained for other QDs.

Photoluminescence measurements on the QDs located on the suspended GaAs bridge reveals an unusual behavior, i.e., some QDs are found to blueshift and others to redshift with the compressive biaxial stress, see Fig. 4.8. Figure 4.9 illustrates the opposite spectral behavior of QD1 and QD2. The QD1 with a slope of 2.47 µeV/V is almost five times more tunable than the QD2 with a slope of −0.52 µeV/V.

In total, 29 QDs are strain-tuned during the experiment. Figure 4.10 presents a histogram of the tuning slopes and their distribution as a function of transition wavelength. The absolute tuning range distributes over an interval of 2.5 µeV/V, which could be due to the variations in the local strain profile caused by the imperfections in the strain-transfer and semiconductor layers. The majority of the QDs can be bluetuned with a slope of around 1.5 µeV/V. There is no correlation

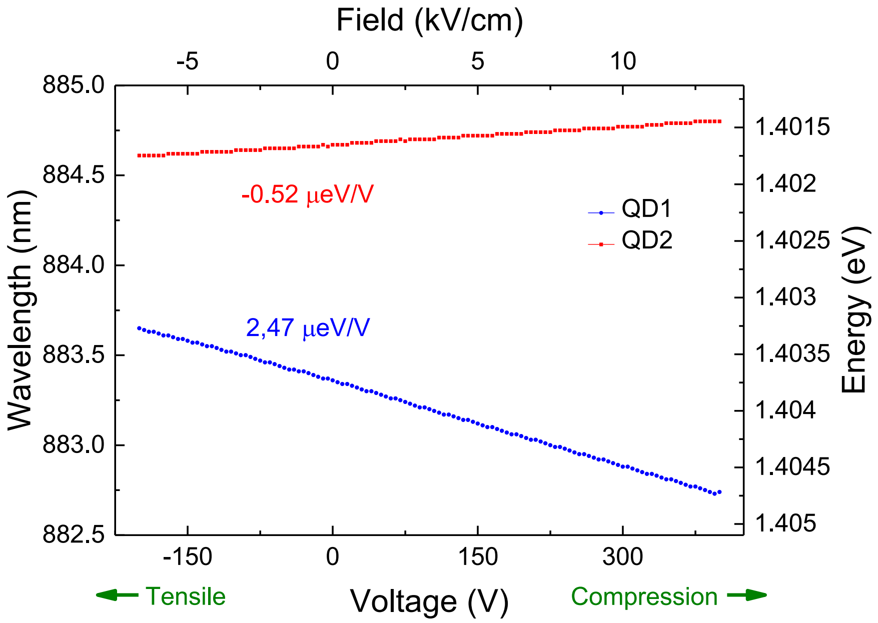

Figure 4.9: Plot of the emission peak versus voltage for QD1 (blue) and QD2 (red). QD1 blueshifts with compressive biaxial stress, whereas QD2 tunes in the opposite direction.

between the QD transition energy and the tuning direction or magnitude.

The energy tuning slope is a rather universal measure of the quality of strain transfer onto the sample. Comparing our result with the reported values of the tuning slopes measured for the QDs in similar heterostructures allows a rough estimate of the amount of stress induced on the semiconductor layer. Jöns *et al.* reported values of more than 4 µeV/V in Ref. [129], where the GaAs membrane was transferred onto the uniaxial PMN-PT crystal via a layer of polymethylmethacrylate (PMMA), which rigidifies at low temperatures. They estimated a lower bound of the maximum applied stress of ±23 MPa. From this the stress induced in our sample can be estimated to be around two times smaller, i.e., on the order of 10-15 MPa.

The QD energy tuning slopes reported in the present work are unusually low for samples, where a gold layer is used to transfer strain. The QDs have been demonstrated to tune with slopes as large as 10 µeV/V [136] with the same strain transfer method. The reasons causing a significant relaxation of strain in the transfer layer could be an imperfect contact between the metal layers deposited on the piezoelectric substrate and the GaAs sample, and a four times thicker layer of the transfer metal (400 nm instead of the usual 100 nm). The reduced amount of the induced strain could also be caused by a lower performance of the PMN-PT crystal.

Despite the moderate strain-induced QD energy shifts achieved in this work, the opposite sign of the shift direction for different QDs is an unexpected outcome. Such observations triggered an idea that the QD energy tuning direction could be related to the spatial position of the QD on the bridge, which is elaborated in the following section.

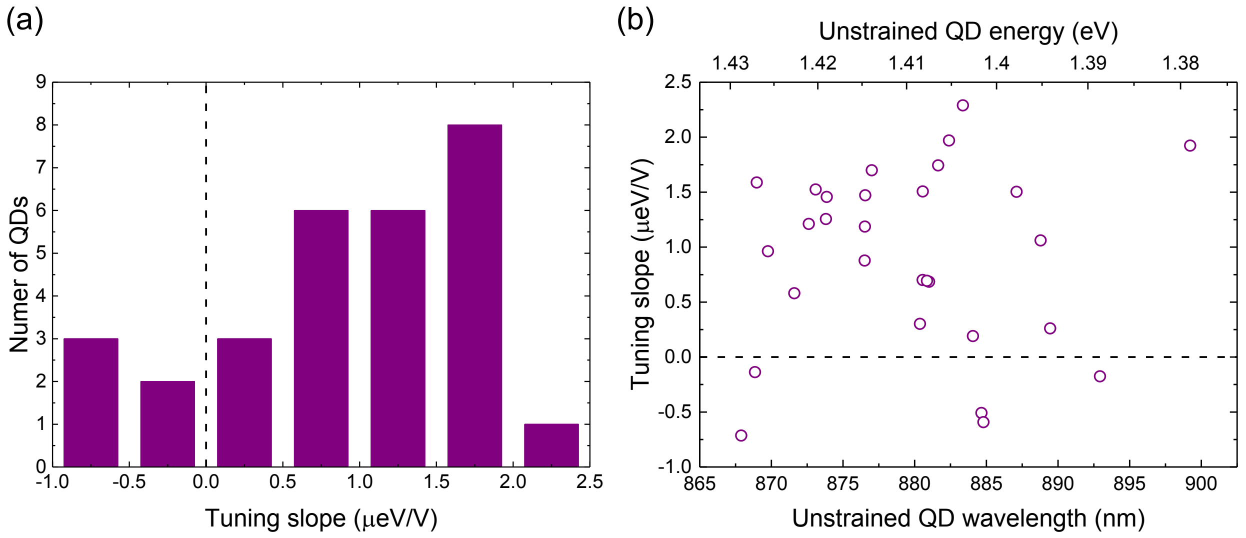

Figure 4.10: Distribution of tuning slopes of all measured QDs. (a) Histogram of the QD energy tuning slopes. (b) Energy tuning slopes as a function of the unstrained QD emission wavelength. The dashed line visually separates the two regimes of opposite QD tuning directions.

4.4 Spatial map of the strain-induced band-gap shift

The strain profile depends on the geometry of the sample and the material parameters. In this work, the sample has a rather complicated shape of a narrow suspended bridge attached to a pair of large rectangular membranes. The more accurate dimensions can be extracted from the SEM images of the sample (Fig. 4.11) and the material composition of the sample is well known. This allows to calculate the spatial strain profile induced by an arbitrary external stress acting on the sample. Subsequently, it is possible to calculate the spatial profile of the strain-induced band-gap energy shift using the Pikus-Bir Hamiltonian, presented in Sec. 4.1.2. By knowing the spatial position of the measured QDs on the sample, it is convenient to map them on the calculated energy shift map and search for the dependencies of the QD energy change on its spatial position.

In the following, a procedure used to obtain the spatial map of the band-gap shift is discussed. In order to obtain the strain tensor as a function of position, finite element method simulations are performed using Comsol Multiphysics 4.3b. Linear elasticity is assumed, which is justified since stresses significantly below the material threshold have been applied. Initial compressive biaxial stress σ_{bi} of 5 MPa and roller conditions are applied to the sample surfaces framing the structure. Fixed constraint of zero displacement is set to one of the surfaces perpendicular to the frame. InAs is chosen as the QD material.[1] In order to match the experimental conditions, the material stiffness tensor aligned to the [110], [1$\bar{1}$0], [001] crystallographic directions (Eq. (4.5)) is used for InAs with c_{11} = 83.4 GPa, c_{12} = 45.4 GPa, and c_{44} = 39.5 GPa [137]. The full strain tensor is obtained from the

---

[1] Note, that due to an intermixing of the QD material and the capping layer material during the growth process, the QDs can have a finite content of gallium. As a result, the size and the shape of the QD can change, which strongly influences the key parameters of the QD like the carrier confinement and the emission energy.

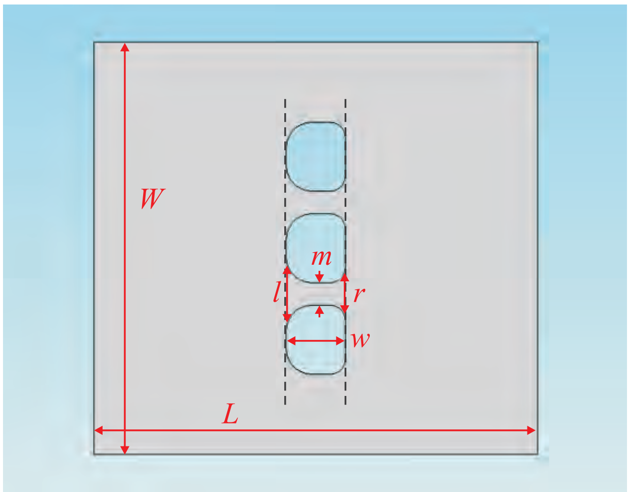

Figure 4.11: Geometry of the sample used in the numerical simulations. The extracted values from the SEM images are the following, $L = 34.8\,\mu\text{m}$, $W = 32.3\,\mu\text{m}$, $l = 4.65\,\mu\text{m}$, $w = 5.5\,\mu\text{m}$, $k = 3.98\,\mu\text{m}$, $r = 3.15\,\mu\text{m}$, $m = 1.77\,\mu\text{m}$. The values of l and r are the vertical distances between the two points, where the bridge intersects with the black dashes lines on the left and on the right, respectively.

simulations on InAs under equibiaxial stress.

The material parameters used in the calculations are dilatation and shear deformation potentials $a_c = -5.08\,\text{eV}$, $a_v = -1\,\text{eV}$, $b = -1.8\,\text{eV}$, $d = -3.6\,\text{eV}$, and a spin-orbit coupling constant $\Delta = 0.38$, see Eq. (4.10) [19, 130]. Figure 4.12(a) shows the spatial map of the InAs band-gap shift. As before, a positive energy shift refers to an increase of the band gap due to compressive strain. The colored dots illustrate the spatial distribution of the measured QDs, and the relative amount of the energy shift is shown by the color of the dot. The QD position with respect to the middle point of the GaAs bridge is determined as follows. The laser spot is positioned at the center of the GaAs bridge as judged from the CCD camera image. By stepping with nanopositioning stages from the center of the bridge to the point where the photoluminescence intensity of the QD is maximal, the QD position in the xy-plane is found with an uncertainty of half the laser spot. The white dashed circles in Fig. 4.12(b) show a position error of 1 µm.

The map reveals a strong band-gap-shift dependence on position. Not only the magnitude, but also the sign of the shift follows the inhomogeneity of strain on the sample. In homogeneously strained regions (far away from the bridge) the InAs band gap blueshifts as expected for compressive strain. The presence of the bridge alters the strain profile greatly, and, as a result, the change of the band gap varies spatially. The sign of the shift is even inverted at certain positions, i.e., it redshifts. The absolute magnitude of the energy change is strongly enhanced on the bridge structure, which reflects the influence of structure geometry on the strain profile, compare with Fig. 4.7.

In order to relate the calculation with the experiment, a region of the suspended structure is analyzed in more detail in Fig. 4.12(b). The energy of most of the QDs increases with compressive strain, which is in consensus with theory. However, several QDs located in the corners or close to

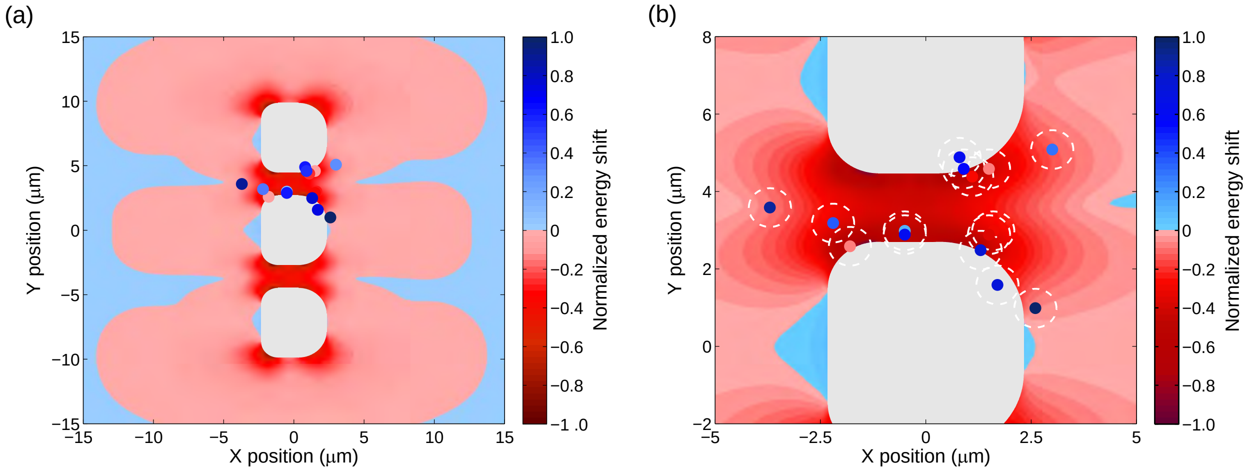

Figure 4.12: InAs band-gap energy shift as a function of spatial position on a GaAs bridge sample. (a) Normalized spatial color-coded map of the InAs band-gap shift induced by equibiaxial stress. Realistic sample dimensions extracted from the SEM images are used for calculations. The measured QD positions are shown as dots while the dot color represents the magnitude of the QD energy shift normalized to the maximum measured QD shift. (b) Magnified view of the energy-shift map. The dashed lines show the accuracy of the QD position (around 1 μm).

the edges of the bridge redshift in energy. Such behavior can be explained as a combination of two factors. First, the QDs can be subjected to uniaxial stress due to the asymmetric shape of the bridge, which has a different impact on the band-gap shift than biaxial stress. Second, the material content of different QDs can vary due to the probabilistic nature of their growth [138]. Self-assembled QDs are composed of an $In_{1-x}Ga_xAs$ alloy with a varying content of gallium, x. It has been reported that the emission energy of QDs subjected to uniaxial strain aligned to [110] crystallographic axis can shift either direction depending on x [129].

The band-gap shift versus the gallium content x in $In_{1-x}Ga_xAs$ is calculated for the uniaxial stress of 5 MPa applied along the [100] and [110] directions, see Fig. 4.13. The band gap redshifts when the tensile stress parallel to the [100] direction is applied. A very similar redshift is induced by the tensile stress along [110]. The band-gap behavior under the compressive stress along [100] depends on the content of gallium. In particular, the gap energy blueshifts as expected, but only until the gallium content x is above 0.39. For InAs and In-rich alloys, the band-gap energy reduces with both the tensile and the compressive stress along the [100] direction. Such behavior for InAs has been previously reported [139]. The compressive stress along [110] induces an increase in the band-gap energy, although the shift is small for InAs. These findings indicate that the observed bidirectional shift of the QDs might be related to their material composition, provided the uniaxial strain.

To check the uniaxial character of the strain tensor, the finite-element-method simulations are analyzed. The strain tensor components ϵ_{xx} (black), ϵ_{yy} (red), ϵ_{zz} (blue) and ϵ_{xy} (purple) are shown in Fig. 4.14. The cross terms ϵ_{xz} and ϵ_{yz} are negligible and are not discussed further. Most

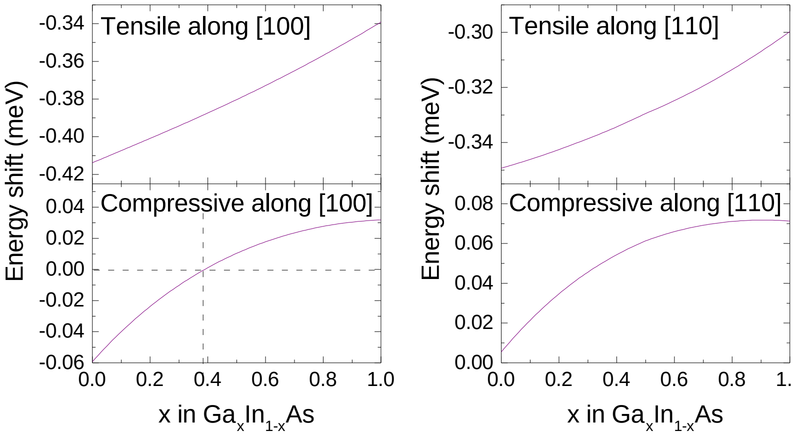

Figure 4.13: Band-gap shift of $\mathrm{In}_{1-x}\mathrm{Ga}_x\mathrm{As}$ under pure uniaxial stress of 5 MPa along the [100] and [110] direction as a function of the gallium content x. Under the tensile stress along [100] the band-gap energy decreases for all values of x. The same is the case for the tensile stress along [110]. If the uniaxial stress along [100] is compressive, the energy shift reverses from the red to the blueshift as the fraction of gallium reaches 0.39. Above this concentration the band-gap energy is increased with respect to the unstrained case. This point is indicated by the intersection of the black dashed lines. Under the compressive stress along [110], for all x values the band-gap energy increases. Note that for pure InAs the predicted shift is small.

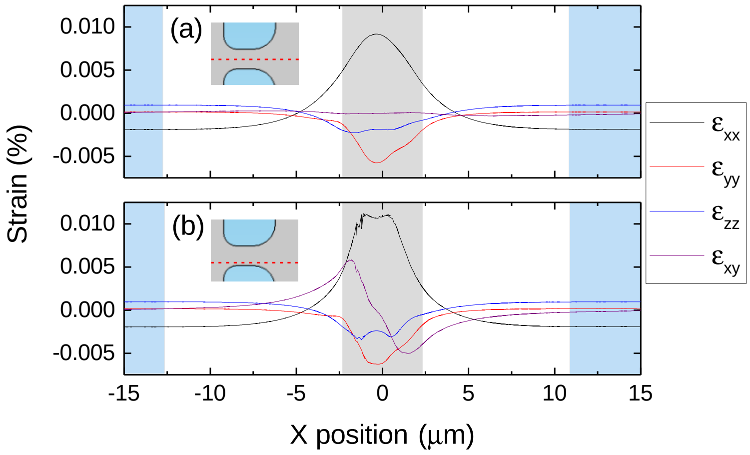

Figure 4.14: Strain tensor obtained from the finite-element-method simulations. (a) and (b) Strain tensor components along the [110] (ϵ_{xx}), [1$\bar{1}$0] (ϵ_{yy}), and [001] (ϵ_{zz}) direction as a function of the position along the x-axis indicated by the red dashed line in the insets. The biaxially stressed part of the membrane is indicated by the blue shaded area, and the suspended bridge is shown in gray.

of the strain tensor elements are nearly uniform along the short axis of the bridge as can be seen by comparing the line scans in Fig. 4.14(a) and (b). Only the off-diagonal tensor element ϵ_{xy} changes significantly across the bridge. This term is responsible for reducing the redshift of the band gap under the tensile stress and the blueshift under the compressive stress. All the strain components, on the other hand, vary significantly as a function of the position on the long axis of the bridge. The center of the bridge is strained the most, while the strain relaxes towards the sides of the sample. Under a crude approximation, a compressive biaxial stress induces the tensile uniaxial strain on the bridge, as inferred from the sign flip of the term ϵ_{xx}. Effectively, the QDs embedded in that region are subjected to the tensile uniaxial strain either along the [110] or $[1\bar{1}0]$ direction and are expected to redshift in energy. Such behavior is observed only for several QDs embedded in the corners of the bridge. The reasons for the blueshift of the other emitters are not exposed by the crude analysis assuming the tensile uniaxial stress. Evidently, the spatial strain profile on our sample is more complex and cannot be treated approximately. The material content of the QDs might play a role in the direction of the exciton energy shift, whereas in the calculations for Fig. 4.12 the parameters for pure InAs have been used.

4.5 Outlook: Enhancement of the exciton energy shift in a suspended bridge geometry

The ability to strain-tune the energy of the excitons in a QD allows to conduct a variety of experiments where optical properties of individual QDs and interaction between the QDs need to be controlled. Studies of QDs embedded in PhC structures also benefit significantly from having such a “tuning knob”, which allows to tune the properties of the QDs. For example, cavity-QED experiments rely on the strong interaction between QDs and a PhC cavity. This regime can be entered when the QD is very close in energy with the cavity mode. In practice, there is a rather small chance that the QD will be in resonance with the fabricated cavity without external adjustments by the electric field, temperature or stress. While the temperature tuning is detrimental to the optical yield and quality of the QDs [124], changing the exciton energy by the electric field preserves the optical quality, but at a cost of a limited spectral tuning range of a few meV, or otherwise, incompatibility with the PhC fabrication [104]. Manipulating the energy of the excitons by strain is desired when maintaining a good optical quality within a wide range of the accessible energies is needed.

It is shown in the previous section that the amount of strain induced on the sample varies spatially and this distribution is dictated by the geometry of the structure. In a bridge geometry, the suspended parts under external stress are free to relax in one axis, which results in a redistribution of the total induced strain in and around the bridge. An increase of an order of magnitude is observed for the absolute value of ϵ_{xx} in the geometry considered in this work, see Fig. 4.14. In principle, the suspended bridge can be patterned with PhC structures, and in this way, the strain enhancement would be achieved only for the QDs located in the photonic nanostructure. It is known that the photonic modes are barely affected by the induced strain [128]. Therefore, a small amount of stress applied on the piezoelectric substrate would result in a significant energy shift of

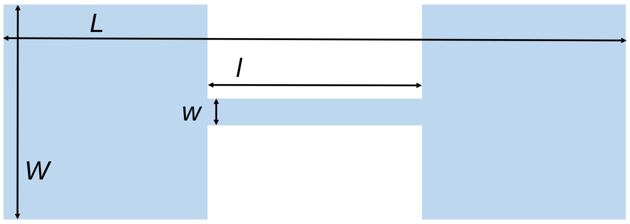

Figure 4.15: A sketch of a dumbbell-shaped bridge for which Eq. (4.13) is derived. The dimensions L, W, l and w refer to the overall bridge length, bridge width, central length, and central width, respectively.

the QDs, but a small alteration of the structure itself.

Similar approach of strain enhancement but in a slightly different context has been proposed for optoelectronics applications on germanium, silicon, and silicon-on-insulator-based platforms [140–142]. In Ref. [140] it has been reported that light emission from a tensile-strained germanium-on-insulator device layers is enhanced by a factor of 260 over bulk germanium owing to stressor deposition and sample geometry. A germanium-on-insulator film is deposited on a silicon substrate, where some parts of the substrate are selectively removed leaving a suspended germanium-on-insulator structure. Silicon nitride stressors are deposited to induce a tensile stress on the germanium layer. The resulting strain alters the band structure of germanium such that the band gap becomes direct and can emit light efficiently. Carefully engineering the structural geometry allows to achieve a 20-times enhancement of strain induced by thermal mismatch of germanium layers grown on silicon or silicon-on-insulator substrates in Ref. [141]. Finally, similar suspended structures fabricated on silicon-on-insulator are characterized in Ref. [142], where stress is used to increase charge-carrier mobility for nanoelectronics devices. In the latter work, an analytical formula allowing to calculate the amount of strain enhancement relative to the initial strain is derived:

$$\epsilon_{xx}^{\text{bridge}}/\epsilon_{\text{in}} = \frac{1+\frac{l}{l+L}}{\frac{w}{W}+\frac{l}{l+L}}, \tag{4.13}$$

where $\epsilon_{xx}^{\text{bridge}}$ is strain along the bridge, ϵ_{in} is the initial strain. The formula is derived for a simple geometry of a suspended dumbbell-shaped bridge with the following dimensions: central length l, central width w, overall bridge length L, overall width W. A sketch of the structure is shown in Fig. 4.15. Only geometrical factors are taken into account, whereas material anisotropy, crystal orientation and thickness of the structure are neglected. Nevertheless, this simple formula allows to roughly estimate the enhancement of strain for a simple shape. It tells that by properly designing the size ratio of the central bridge and the surrounding structures the effect of the initial strain can be enlarged significantly. Apart from the fillets in the corners and a slight asymmetry, there are no substantial differences between the geometry of the sample used in the present work and the one shown in Fig. 4.15. Therefore, Eq. (4.13) is a good approximation for the stain induced in the bridge investigated in the present work. However, since we possess no quantitative information about the magnitude of the strain induced in the sample, further analysis is not conducted.

4.6 Conclusions

In this chapter, strain-tuning of self-assembled InAs/GaAs QDs embedded in suspended GaAs bridges is demonstrated. The fabrication procedure of GaAs membranes elevated above the piezoelectric substrate is developed. Such a method in principle allows the creation of different-geometry strain-tunable devices, such as PhC membranes or even more complex photonic networks. In total 29 QDs are characterized by means of time-integrated photoluminescence spectroscopy. Each dot is located with respect to the middle point of the bridge, which enables to investigate possible correlations of the QD tuning-behavior and its spatial position. It is found that several QDs blueshift under compressive biaxial stress, whereas a few tune to lower energies in contrast to the expected behavior. Such observations are explained by the effect of the tensile uniaxial strain induces along [110]. From the analysis of the strain-tensor as a function of spatial position it is found that the initial biaxial stress induces dominantly a uniaxial strain on the bridge structure. The effect of the uniaxial strain along the [110] direction on QDs of different material content has been investigated before [129]. Additionally, our observations yield yet another important conclusion, namely that the strain effects can be deliberately controlled by engineering the sample geometry. This concept is already applied in optoelectronics and nanoelectronics research, nevertheless, further technical development is required if such a technique is to be used for photonic applications.

Chapter 5

The exciton Mott transition in coupled quantum wells

The Mott transition is a phase transition from an electrically insulating to a conducting state of matter, and was first predicted to occur in a system of correlated electrons [143]. Over the past decades, this metal-insulator transition has been studied in different physical platforms such as semimetals, transition metal compounds, doped semiconductors, organic salts, cold atom gases, and recently, superconductors [144–151]. As Mott pointed out, the transition may also happen in a population of interacting electrons and holes, in which insulating excitons are ionized to a metallic phase of free carriers [11]. The exciton Mott transition has been investigated in 2D semiconductor nanostructures and found to occur at electron-hole pair densities of the order of 10^{10}–$10^{11}\mathrm{cm}^{-2}$ and temperatures below 10 K [8, 152–154]. In Refs. [8, 152, 153] a picosecond-pulsed excitation was used to create carriers above the quantum well band gap and the carrier dynamics were probed by terahertz or time-resolved photoluminescence spectroscopy. The metallic-insulating state transition in the electron-hole system was reported to occur gradually over a time scale of several hundreds of picoseconds. Stern *et al.* [154] reported an abrupt phase transition inferred from the time-integrated measurements of exciton photoluminescence linewidth and screening-induced energy shift. Theory predictions have reached no consensus about the nature of the exciton Mott transition either, since several works suggest that the ionization of excitons occurs abruptly, which indicates a first-order phase transition [155, 156], and some predict a second-order transition that occurs as a smooth function of the governing parameters, carrier density and temperature [157–159].

Indirect excitons (IXs) in coupled quantum wells (CQWs) form an attractive platform for uncovering fundamental quantum effects. The IX is composed of an electron and a hole residing in opposite QWs, which are separated by a thin potential barrier. The small spatial overlap between the electron and the hole leads to a long radiative lifetime of the IX compared to a spatially direct exciton (DX) [160–164]. The radiative lifetime of the IXs can be tuned by an external electric field via quantum-confined Stark effect [160, 161, 163]. Long-lived IXs can therefore reach a thermodynamic equilibrium with the cold lattice, which allows the study of coherent many-particle effects. Due to their rich and highly tuneable properties, the IXs have become an important platform for studying excitonic transport [165, 166], cold gas condensation [166–169], low threshold lasing [170], terahertz generation [171], and optical refrigeration [172]. The exciton Mott transition in multiple QWs has been studied with various techniques. In terahertz spectroscopy, the transition is investigated by probing the internal transitions of excitons, providing a direct measure of exciton densities and binding energies [8, 152]. In photoluminescence spectroscopy, the transition manifests as a temporal broadening, a change in the spectral shape or a spectral shift of the excitonic peak [154, 173]. Nevertheless, there has been a lack of experimental study of the exciton Mott transition under steady-state excitation, which allows to investigate the nature of the phase transition in equilibrium.

The objective of this chapter is to discuss the Mott transition of IXs observed in time-integrated photoluminescence spectra of CQWs. In semiconductors the insulating state is an exciton gas and the metallic state is an electron-hole plasma (EH-plasma). The exciton Mott transition is studied in InGaAs/GaAs CQWs in a steady state and a gradual ionization of the excitonic peak is observed with increasing excitation intensity and temperature. The insulating and conducting populations recombine radiatively at different energies and are therefore easily resolved spectrally. The exciton-density-temperature phase diagram of the transition exposes two regions with exciton-dominant and plasma-dominant populations that are separated by a linear boundary fulfilling. This boundary has an associated critical exciton density n_c that is extracted using two independent models yielding $n_c \sim 2.3 \times 10^{10}\text{cm}^{-2}$ at $T = 12.5\,\text{K}$, which is in good agreement with previously measured values. The smoothness of the transition is quantified by observing the relative exciton population in the indirect transition. Alternative mechanisms that could explain the observed effects are ruled out. The excitonic Mott transition is studied in a narrow range of externally applied electric field but it is observed also at higher field values. A peculiar feature arises at particular electric fields, where a strong photoluminescence quenching suggests the formation of the excitons of a parallel-spin configuration that are optically dark. Our work emphasizes the rich potential of CQWs for studying fundamental many-body quantum phenomena whose dynamics may be vastly tuned by the external bias.

5.1 Indirect excitons in GaAs-based heterostructures

In this section, the energy structure of the InGaAs CQWs is discussed. CQWs are formed of two single QWs separated with a thin barrier of a semiconductor with a larger band gap. The barrier has to be thin enough to allow tunnelling of carriers between the two QWs. The band diagram of the CQWs computed for an electric field of 19 kV/cm is shown in Fig. 5.1 (a).[1] In order to overview the optical transitions of the CQWs relevant for this work, it is sufficient to account for the first three eigenstates of electrons (e1, e2, e3) and heavy holes (h1, h2, h3). At zero bias, the built-in electric field of the p-i-n junction equal to $30\,\text{kV}\,\text{cm}^{-1}$ renders the ground-state single-particle wavefunctions e1-h1 to be localized in adjacent wells [175]. The exciton formed of e1 and h1

---

[1] The band diagram and the eigenstates of the CQWs are calculated from a model based on the single-particle effective-mass Schrödinger equation (a tunnelling-resonance technique is implemented [34], the band parameters are taken from Ref. [174]). The theory model has been implemented by Dr. Petru Tighineanu.

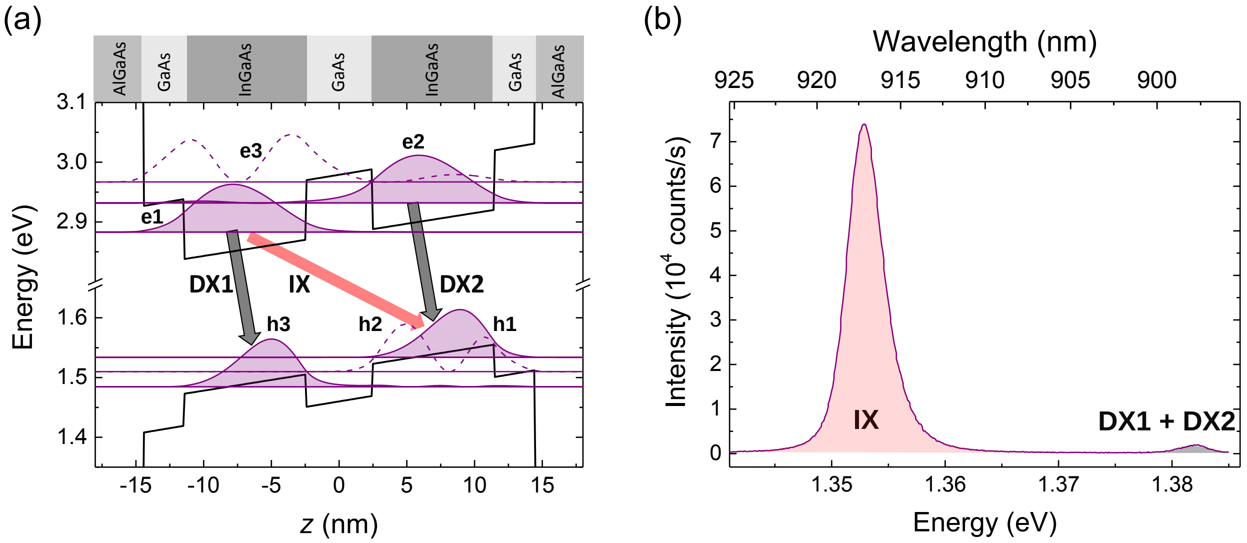

Figure 5.1: Energy structure and the relevant optical transitions in CQWs. (a) The band diagram of the CQWs at an electric field of 19 kV/cm at which the Mott transition is observed. The first three electron (e1, e2, e3) and hole (h1, h2, h3) eigenenergies and probability densities are shown. The indirect-exciton photoluminescence originates from the e1 → h1 (red arrow) transition, while the direct excitons originate from e1 → h3 and e2 → h1 (gray arrows). (b) Low-temperature photoluminescence spectrum of the CQWs. The intense indirect transition is visible at lower energy (IX), whereas the two direct excitons recombine at a higher energy (DX).

is spatially indirect (IX) and is the ground state of the CQWs. Another indirect transition e1 → h2 (IX2) is optically weak. The relevant excited states of the CQWs are excitons composed of charge carriers located in the same quantum well. These are the spatially direct excitons formed of e1-h3 (DX1) and e2-h1 (DX2). In this context, we also refer to excitons in bulk GaAs as direct excitons. For clarity, when discussing the photoluminescence measurements we will refer to a spectral distribution of the indirect excitons as the IX and as the DX for the direct excitons.

Since in this work the properties of the CQWs are probed mainly by optical measurements, a representative photoluminescence spectrum is discussed in relation to the band diagram. Figure 5.1 (b) shows a low-temperature time-integrated photoluminescence spectrum of the CQWs. Two energy distributions separated by around 30 meV are resolved in the spectrum. The intense spectral feature observed at lower energy originates from the radiative recombination of the indirect excitons. The photoluminescence stemming from the two direct excitons is observed at a higher energy. The energies of the direct excitons are close to each other, and, therefore, it is difficult to resolve each of them in the spectrum.

Indirect excitons have significantly different properties compared to direct excitons in bulk GaAs owing to a spatial separation of the charge-carrier wavefunctions and relaxation of the momentum conservation along the growth direction. Consequently, the indirect excitons are long-lived and have an increased cooling rate compared to the excitons in bulk GaAs. Also, the indirect excitons possess a permanent electric dipole moment and interact repulsively. This has the following implications: the indirect excitons efficiently screen a growth-induced disorder potential and can be controlled via an electric field. In the following, these features are discussed in more detail.

5.1.1 Lifetime of indirect excitons

The indirect exciton possesses a prolonged lifetime due to a small overlap between the probability distributions of an electron and a hole. Its radiative lifetime can be a few orders of magnitude longer than that of the direct exciton and vary between tens of nanoseconds to several microseconds [160–164]. It is set by the barrier width of the CQWs and, conveniently, it can be tuned by several orders of magnitude with the applied electric field [176]. Long-lives indirect excitons diffuse in the plane of the QW resulting in a significantly larger area where the radiative recombination takes place as compared to the direct excitons.

5.1.2 Thermalization rate

The lifetime of the indirect excitons exceeds the time scale of thermal relaxation processes in GaAs. In the following, the thermalization dynamics of excitons is reviewed. After nonresonant photon absorption, an initially created unbound electron and hole pair relaxes to the respective single-particle ground states and forms an exciton within tens or hundreds of picoseconds [177]. After the exciton is formed, it has a finite in-plane momentum until it relaxes to a close-to-zero-momentum state. Exciton cooling occurs via exciton-exciton, exciton-free carrier scattering, or emission of longitudinal acoustic (LA) phonons [8, 177]. The latter process is dominant at low temperatures and occurs at characteristic time scales from few tens of picoseconds to a few nanoseconds [178, 179].

The emission of LA phonons in QWs is more efficient as compared to bulk. It is because the momentum of the excitons in the z-direction is not conserved in QWs, and consequently, the ground state exciton couples to a continuum of phonon states [178]. Therefore, excitons in QWs cool to the crystal lattice temperature three orders of magnitude faster than in bulk GaAs [179]. The fast cooling rate along with the long exciton lifetime allows the formation of cold indirect-exciton gases suitable for studying collective quantum effects.

5.1.3 Static electric dipole moment

An indirect exciton possesses a static electric dipole moment due to a spatial separation between the electron and the hole. The indirect excitons, as aligned dipoles, interact repulsively, and thus effectively screen in-plane disorder states occurring due to growth-induced well-width fluctuations. In conventional semiconductor heterostructures, the in-plane variations of the QW potential are on the order of a millielectronvolt[180]. For temperatures relevant for this work ($< 20\,\mathrm{K}$), the thermal energy is smaller than the potential dips and the localization could spoil the 2D behavior of excitons. In CQWs a minimum in the disorder potential can be filled with a small number of indirect excitons and additional excitons no longer see this minimum since it is washed out due to the repulsive interaction between the indirect excitons.

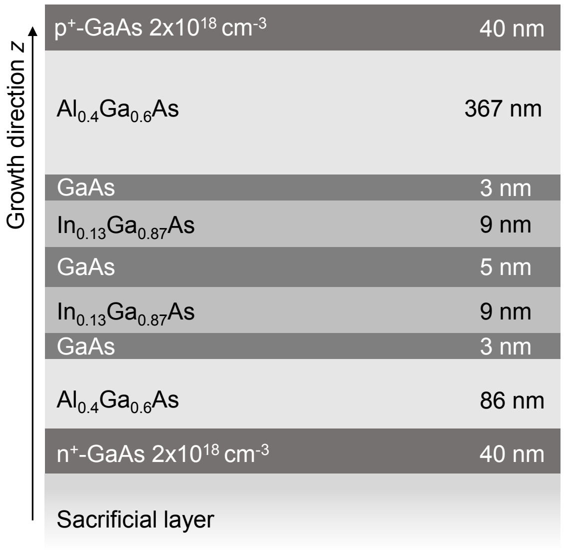

Figure 5.2: Cross section of the CQWs wafer used in this work.

An external electric field can be used to tune the energy of an electric dipole. The dipole moment of an indirect exciton is essentially fixed and set by the quantum-well separation. Therefore, its energy depends linearly on the electric field parallel to the dipole axis. Such a property allows to create artificial traps for indirect excitons by manipulating the spatial profile of an electric field [164, 181]. Spatially defined electrical gates have been used to trap single indirect excitons, which is an example of lithographically defined QDs [182].

5.2 Photoluminescence spectroscopy on coupled quantum wells

Conventional photoluminescence spectroscopy provides an extremely sensitive tool to probe the energy structure and inner dynamics of semiconductor nanostructures. In this work, spectrally resolved photoluminescence spectroscopy is employed to measure the exciton energy by detecting the frequency of the emitted photons. It also provides information about spectral broadening of excitons due to defect states of impurities, interface roughness, or structural disorder. Insight into the exciton-exciton interaction is obtained by measuring the exciton energy as a function of optical-excitation intensity, which is a handle to vary the exciton density. The decay dynamics of excitons can be conveniently studied by measuring the time-resolved photoluminescence trace at a frequency of interest. In this section, the photoluminescence of the CQWs sample used in this work is studied as a function of electric field and excitation power. The time-resolved dynamics of both the DX and the IX is investigated by detecting the time evolution of their photoluminescence.

The sample under study is prepared from the CQWs wafer grown at Swiss Federal Institute of Technology, Zürich, Switzerland. The cross-section apart from the substrate of this wafer is shown in Fig. 5.2. A mesa is defined on the sample via conventional UV lithography and wet-etching, according to the recipes described in Appendix A. Ohmic contacts are deposited on the p- and n-doped GaAs layers to allow for bias application. The procedure for the contact deposition is presented in Appendix A. The sample is mounted on a titanium sample holder and connected to the printed-circuit board via gold wires. The electrical contacts are tested at low temperature by measuring the IV curves and testing the ohmic behavior of the p-type and n-type contacts. The details on their performance can be found in Chapter 2.

This work aims to study many-body effects in a cold interacting exciton gas. In order to create such conditions, the sample is cooled to a temperature of a few Kelvin in a cryostat. For optical measurements, one CQWs sample is placed in a closed-cycle helium cryostat and another sample fabricated with identical procedures is placed in a liquid-helium flow cryostat, see Chapter 2. Only the measurements presented in Figs. 5.3 and 5.4 are performed on the sample placed in the closed-cycle cryostat. The excitons are created by means of optical excitation with laser light. In the experiments discussed in this chapter, the continuous-wave laser beam tuned to a wavelength of 850 nm is used. This wavelength corresponds to pumping of the quasi-continuum of confined states in the CQWs. For the time-resolved measurements of the IX, a pulsed-light source with a repetition rate lower than provided by the Mira laser (76 MHz) is needed. This is due to the long IX lifetime, which prevents it from decaying fully before the sequential excitation pulse generated by the Mira reexcites it after 13 ns. Therefore, a picosecond-pulsed diode laser at 785 nm with a repetition rate of 2.5 MHz, corresponding to a time separation of 400 ns between the consecutive pulses, is used for time-resolved measurements of the CQWs.

In the optical setup around the closed-cycle cryostat the photoluminescence of the CQWs is coupled into a multimode fiber of NA = 0.22 and core diameter of 105 µm to ensure efficient collection of the spatially broad emission from the indirect excitons. Since the optical setup is designed for a particular single-more fiber, significant losses due to mismatched focusing and collimation optics and the multimode fiber are introduced in the collection path. For these reasons, a signal is detected only at high excitation powers. This does not prevent from obtaining information about the optical behavior of the sample but motivates further measurements in the liquid-helium flow cryostat accompanied with an optical setup allowing for free-space collection of photoluminescence.

All other presented optical measurements are performed on the sample placed in the liquid-helium flow cryostat. For the measurements in the flow cryostat the sample is cooled to 12.5 K unless specified otherwise. The temperature is measured by a calibrated Cernox sensor in a four-lead scheme mounted next to the sample on the same surface (see Appendix B) and by a sensor placed on the cold finger. A discrepancy of around 5.8 K between the two measurements is found, the value on the cold finger being smaller. Throughout this work the temperature values obtained by the Cernox sensor are reported, since it provides a more accurate measurement of the actual sample temperature.

The area of the CQWs photoluminescence is measured with a scanning galvanometer-mirror positioning system, which allows to acquire a spatial map of the emission stemming from the sample while keeping the excitation position fixed.

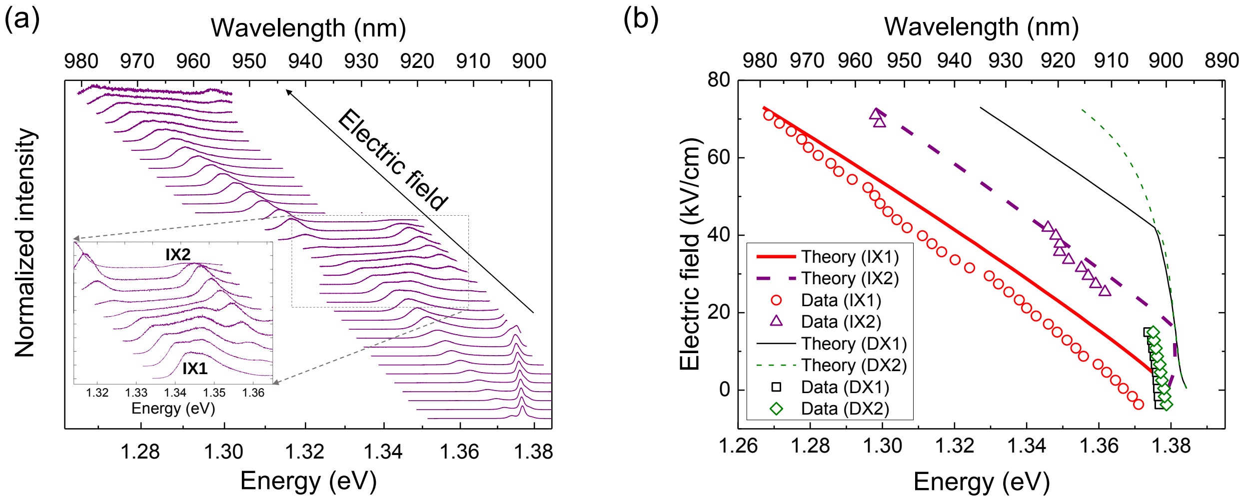

Figure 5.3: Main optical transitions of the CQWs. (a) Photoluminescence spectra taken under high excitation power as a function of electric field. Two indirect, IX1 and IX2, and two direct, DX1 and DX2, excitons are resolved. Inset: A magnified view of the photoluminescence recorded at around the built-in electric field, attributed to the optical-phonon emission. (b) The energy of each transition extracted from the data and calculated using the model presented in Sec. 5.1. The data points for IX1, IX2, DX1, DX2 are shown by the red circles, purple triangles, black squares and green diamonds, respectively. The corresponding theory curves are shown as a thick solid red, thick dashed purple, thin solid black and thin dashed green lines.

5.2.1 Time-integrated photoluminescence spectra

The spectral behavior of the CQWs is investigated by employing time-integrated photoluminescence spectroscopy. In the following, the CQWs photoluminescence is studied as a function of electric field and excitation intensity. Several optical transitions are observed in the spectrum recorded under excitation with high laser power. The origin of the observed signal is analysed and compared to theoretically predicted optical transitions.

As discussed in Sec. 5.1, the electric field is an important parameter that allows to tune the optical properties of excitons in QWs. By analysing the photoluminescence of the CQWs as a function of electric field, the main optical transitions are identified, see Fig. 5.3. High excitation power is used to excite the sample mounted in a closed-cycle cryostat cooled to 4.2 K measured on the cold finger. Note that the sample temperature is likely to be higher by a few Kelvin due to heat load of the printed-circuit board and copper leads and the absence of the radiation shield. The electric field across the CQWs is varied by applying an external bias in steps of 0.1 V from 1.7 to −1.9 V. The photoluminescence spectra are taken with an excitation intensity of 3850 W/cm^2. At such a high intensity, the number of photogenerated excitons is large enough to fill the ground state of the CQWs and populate the higher-energy states. This is evident in the intensity-normalized spectra at small electric fields, shown in Fig. 5.3(a). The emission shifting from around 1.37 to 1.27 eV with an increasing electric field stems from the ground state transition, i.e., IX1, whereas the DX is observed at a slightly higher energy constant at all the field values and is much more

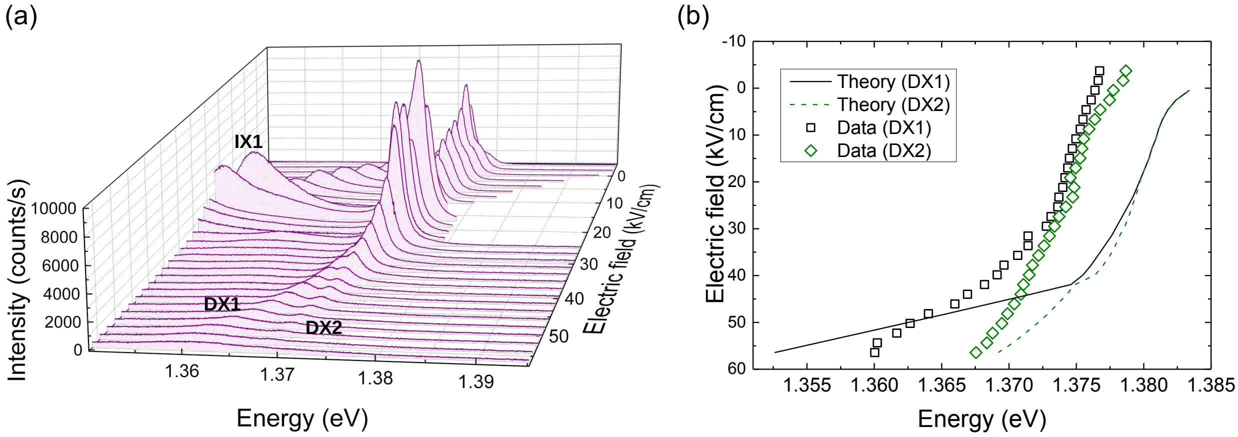

Figure 5.4: Photoluminescence of the direct excitons as a function of electric field. (a) The emission intensity of the two direct transitions DX1 and DX2 is tuned with the electric field. A strong signal observed at zero field reduces as the electric field is increased to around 15 kV cm^{-1}. Further increase in the field strength results in a significant growth of the photoluminescence signal from direct excitons, which again is diminished as the electric field exceeds 30 kV cm^{-1}. The broad signal observed at around 1.35 eV stems from the indirect exciton. (b) Energy of the direct transitions as a function of electric field extracted from the data shown in (a) and calculated using our theory model. Black squares (green diamonds) show the data points and the black solid (green dashed) lines denote the prediction of theory for DX1 (DX2).

intense. The ratio of intensities is dictated mainly by two factors: first, the photoluminescence intensity depends on the oscillator strength of the transitions, which is altered with the electric field, and second, the emitted light is collected through a multimode fiber, which serves as a spatial filter for the diffusive IX emission. The DXs recombine radiatively much faster, so they emit from a smaller spot than the IX, overlapping more efficiently with the spatial mode of the fiber. As a result, the collected photoluminescence of the DX is more intense than that of the IX. Emission originating from another excited state, the IX2 (see the inset of Fig. 5.3(a)), is observed close to the built-in field, which proves to be a peculiar regime in further experiments and is discussed in Sec. 5.4. Interestingly, the IX1 shows a high-energy shoulder as the IX2 emerges in the spectrum, which is attributed to the emission of the longitudinal-optical (LO) phonons.[2] Note that throughout this thesis, IX refers to the lowest-energy transition IX1.

The transitions are identified by their spectral position and electric-field behavior. Due to their direct nature, DXs depend only weakly on the electric field, slightly redshifting in energy as the field strength is increased. Indirect excitons, however, are very sensitive to the electric field and tune in energy by more than 100 meV. In total, under high-power excitation four well-resolved peaks are identified and attributed to IX1, IX2, DX1 and DX2. The peak energy for each exciton is extracted as a function of electric field and compared to the modelled behavior of the respective resonances, see Fig. 5.3(b). Due to a limited spectral range covered by the grating in the

---

[2] The energy of the LO phonons in GaAs (InAs) is around 36 (29)meV, which is very close to the energy separation between the IX1 and the DX (around 28 meV) in the peculiar bias range.

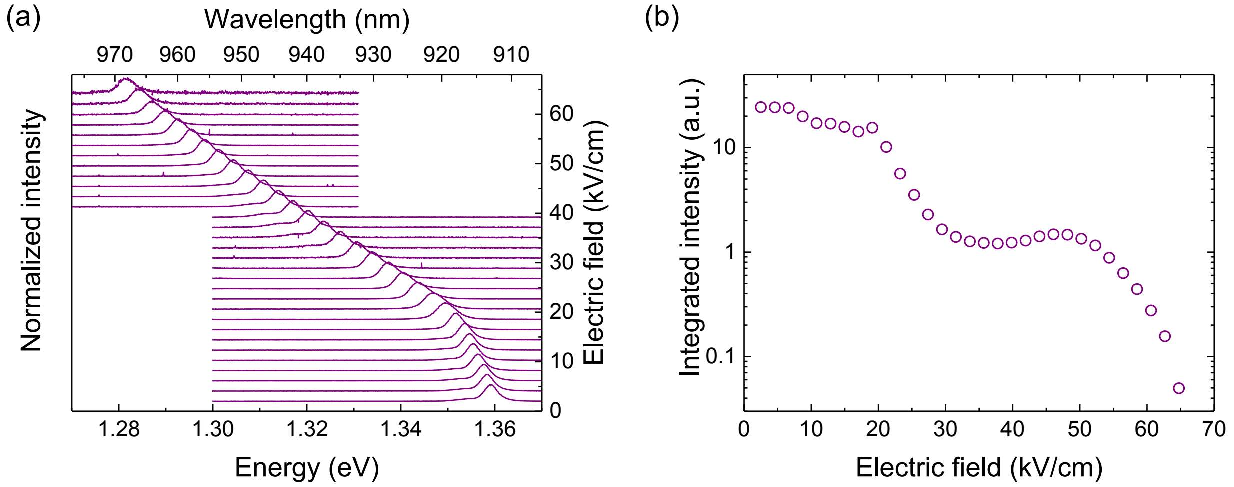

Figure 5.5: Electric-field dependence of the IX photoluminescence. (a) A waterfall plot of the normalized IX spectra as a function of electric field measured at 12.5 K. (b) Bias dependence of the total integrated intensity of the IX extracted from the data in (a). The IX dims by more than a factor of 10 as the field is increased from 0 to 35 kV cm^{-1}. The IX intensity revives again at 50 kV cm^{-1} and is diminished as the field increases further.

spectrometer, the IX2 is observed around the built-in electric field and above 70 kV cm^{-1}, where the photoluminescence signal almost vanishes due to carrier extraction. The data and the theory match very well apart from an offset towards lower energies, which can be caused by a discrepancy of the QW or barrier width, or a material content from the design values. Indeed, an indium content of the quantum wells of 0.151 rather than the designed value of 0.13 fits the data better. Such adjustments are justified since deviations of material content within a few per cent during the growth are plausible.

The direct transition is populated with two excitons, the DX1 and DX2, with similar energy, which are challenging to resolve in the photoluminescence spectra taken at low electric field. However, at large electric field the two transitions diverge from each other in the spectrum as the DX1 becomes indirect and redshifts significantly. Figure 5.4(a) shows the photoluminescence spectra of the direct excitons, where the two transitions are clearly resolved at the electric field values above 35 kV cm^{-1}. The bias dependence of the emission intensity of the DXs is unexpected as the direct excitons become dimmer while the field is increased from 0 to around 15 kV cm^{-1}, but above this value the DX intensity revives and reaches a maximum at 18 kV cm^{-1}. By further increasing the electric field, the DX signal is constantly reduced and finally completely inhibited. This revival of the DX emission coincides with the bias range where the second indirect exciton is observed and emphasizes the peculiarity of this particular regime.

From now on, all the optical measurements are carried out on the CQWs sample mounted in the flow cryostat. The electric field dependence of the IX is studied under an excitation power of 34 W/cm^2, see Fig. 5.5. The electric field is changed by varying the applied voltage from 1.4 to −1.6 V in steps of 0.1 V. The focus is primarily on investigating the emission intensity dependence

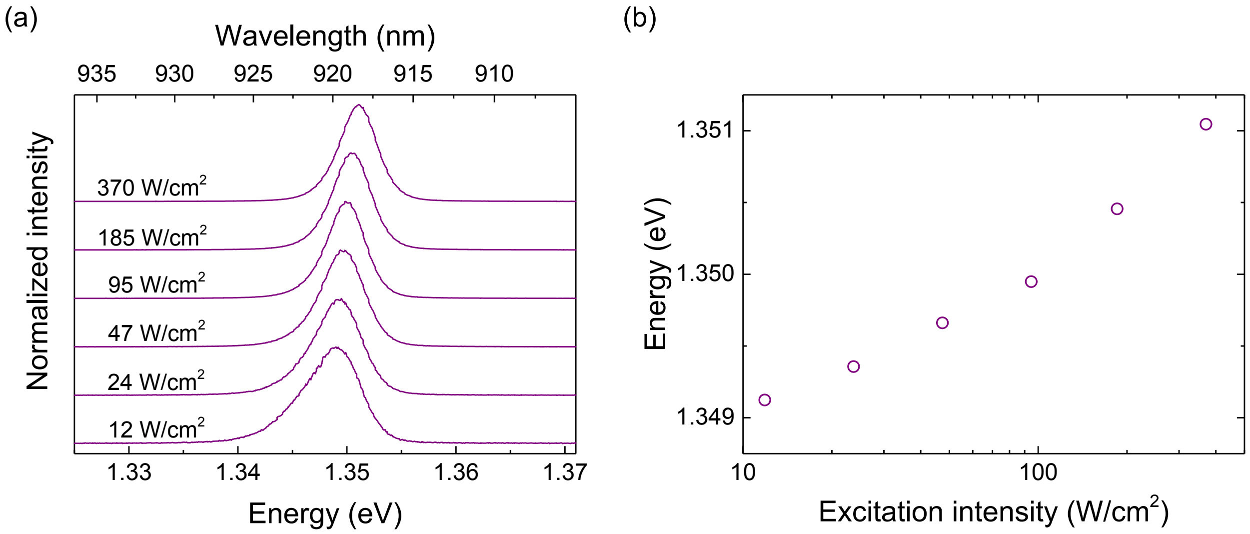

Figure 5.6: Power dependence of the IX emission. (a) Photoluminescence spectra recorded at 19 kV cm^{-1} electric field at varied excitation intensity. (b) The carrier-induced spectral blueshift of 2 meV with increasing power.

on the applied bias and the total integrated intensity of the IX peak extracted from Fig. 5.5(a) is shown in Fig. 5.5(b). The IX intensity seems to follow the unusual dependence on the field as already observed for the direct excitons. While at zero field the photoluminescence stemming from the IX is intense, it is suppressed by more than an order of magnitude at around 35 kV cm^{-1}, and then slightly increases again at 50 kV cm^{-1} before being quenched. This suggests that at certain electric field values, the effects strongly correlating the interplay of the direct and indirect excitons take place, discussed in more detail in Sec. 5.4.

While the externally applied bias provides a knob for controlling the exciton energy, the excitation power is used to vary the exciton-exciton interaction strength, or in the case of EH-plasma, the carrier-induced screening. The density of optically created electron-hole pairs is proportional to the power of the excitation light and is one of the governing parameters of the interaction between the particles. In the following, a power-induced screening of the built-in electric field due to indirect electron-hole pairs is demonstrated in brief.

By increasing the excitation intensity, more and more charge carriers are generated in the ground state. The carriers screen the electric field and shift the transition energies towards lower wavelengths. Figure 5.6 shows emission spectra of the IX at a fixed electric field of 19 kV cm^{-1}. The excitation power is varied by more than an order of magnitude. The IX is lifted in energy by 2 meV with increasing laser power, see Fig. 5.6(b).

5.2.2 Decay dynamics

Under pulsed excitation, the time trace of the photoluminescence intensity allows to study the decay process of the eigenstates of the CQWs. We emphasise that without the microscopic model, describing the decay dynamics of excitons in QWs is a complex task and relies of the phenomeno-

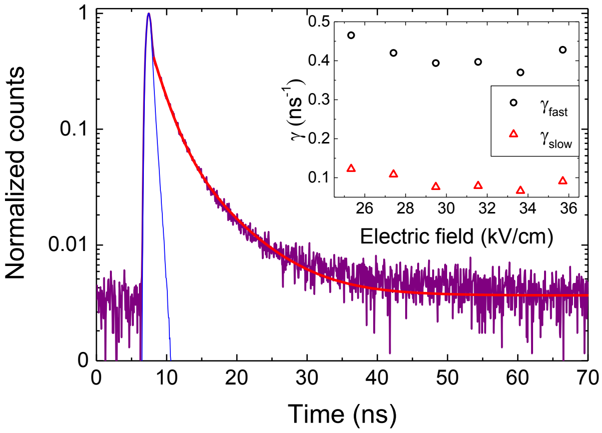

Figure 5.7: Transient photoluminescence intensity curve (purple line) of the DX at the built-in electric field of 30 kV cm^{-1}. The decay curve is fitted well with a biexponential decay model (red line). Inset: the extracted fast and slow decay rates at several electric field values. The DX radiative recombination rate γ_{fast} is slightly reduced with the electric field as the DX slowly turns into the indirect regime. At very short time delays the measured signal is covered by the laser light decay (the blue line).

logical decay models. Since photoluminescence analysis is sensitive to optically active states exclusively, emission decay curves are measured only of the states that couple strongly to light. The dispersed emission spectrum of the CQWs is guided to the avalanche photodiode through a slit with 2.2 meV bandwidth centered at either the IX or the DX peak. The decay dynamics of the DX is discussed first.

The carrier-wavefunction overlap is weakly modified for the DX. Therefore, it decays at a rate close to excitons in bulk GaAs. An example of a transient photoluminescence intensity curve of the DX acquired at the built-in electric field is shown in Fig. 5.7. The decay curves are fitted with a phenomenological biexponential model $I(t) = A_{\text{fast}}e^{-\gamma_{\text{fast}}t} + A_{\text{slow}}e^{-\gamma_{\text{slow}}t}$, where γ_{fast} denotes the lifetime of the fast exponent and γ_{slow} of the slow one. The respective amplitudes of each exponent are A_{fast} and A_{slow}, and t is the observation time of a photon emission event after excitation. The fast constant γ_{fast} of around 0.4 ns^{-1} is attributed to a radiative decay of the DX. The origin of the slow decay γ_{slow} of 0.1 ns^{-1} might be due to the dual nature of the probed transition, since the two direct excitons spectrally overlap. Generally, the DX1 and DX2 can decay at different rates. The radiative decay rate of the DX does not change significantly versus the electric field, since the carrier-wavefunction overlap is roughly constant. At very short time delays, a process even faster than the response function of the used avalanche photodiode takes place. It is likely to be the direct electron-hole pair relaxation to long-lived indirect excitons. However, at a given excitation intensity of 213 W/cm^2, the ground state is rapidly spin filled and this nonradiative channel is closed for higher-energy states.

The key feature of indirect excitons in the context of this work is their long radiative lifetime. Suppressing the IX recombination by an external electric field allows to reach a thermal equilibrium

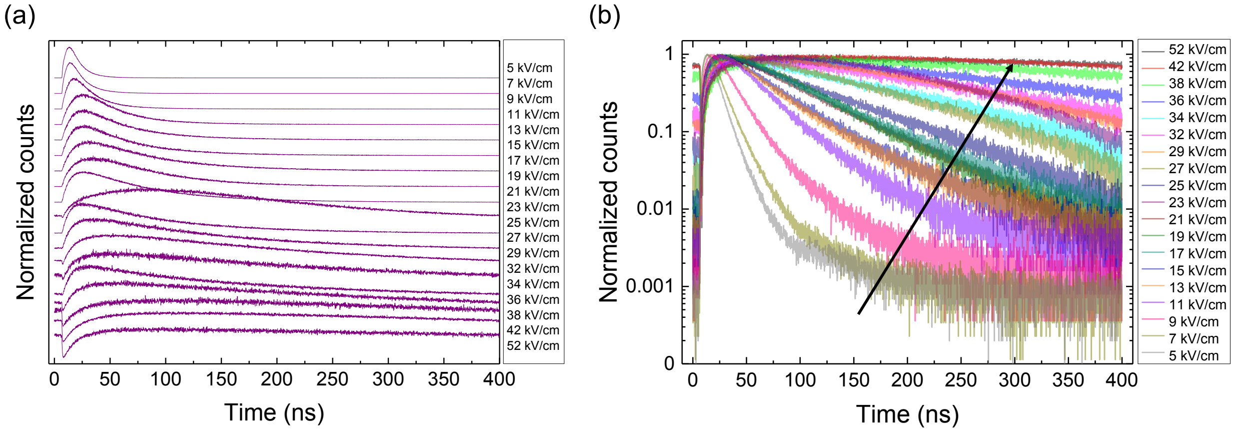

Figure 5.8: Time-resolved photoluminescence measurements of the IX. (a) The decay curves of the IX recorded at varied electric field value in $\mathrm{kV\,cm^{-1}}$ indicated next to each curve. The recombination of the IX speeds up by two orders of magnitude as the electric field is reduced from 52 to $2\,\mathrm{kV\,cm^{-1}}$. (b) The data in (a) shown as an overlay plot. The black arrow indicates the increase of the electric field. The measurements are done under $320\,\mathrm{W/cm^2}$ excitation intensity.

with the crystal lattice, where coherent many-particle effects can emerge. Figure 5.8(a) shows the IX decay curves measured on the center of the energy distribution. As expected, the IX decays faster with a rate of $0.1\,\mathrm{ns^{-1}}$ as the electric field is close to zero. The slow-down of two orders of magnitude is reached at large fields. In comparison to the neighboring curves, the decay curve measured at $23\,\mathrm{kV\,cm^{-1}}$ has an unexpectedly long rise time τ_r (time for the emission intensity to reach its maximum). The rise time reflects the dynamics of the exciton formation and subsequent relaxation to optically active states occurring after a nonresonant excitation into the continuum of the QW. The electric field suppresses the exciton formation efficiency and increases the IX diffusion due to their longer lifetime, hence the longer τ_r. To illustrate how strongly the decay dynamics can be tuned with bias, the time-resolved data is shown in an overlay fashion in Fig. 5.8(b). Close to the flat electrostatic potential (at $5\,\mathrm{kV\,cm^{-1}}$ electric field), the IX decays completely within the sampling window of 400 ns, while it slows down significantly at above $40\,\mathrm{kV\,cm^{-1}}$, where the emission signal stays almost constant between the consecutive excitation pulses.

The measured decay curves are fitted with either a biexponential model close to zero field or a single-exponential model at electric-field values below $25\,\mathrm{kV\,cm^{-1}}$. In the case of the double-exponential fit, the ratio between γ_{fast} and γ_{slow} varies from 2 to 4, and the amplitude A_{fast} is always larger than A_{slow} by more than an order of magnitude. Hence the fast rate is attributed to the dominant radiative recombination of the IX and is compared to the theory model used to calculate the energy diagram of the CQWs (theory 1) and an open-access software provided in Ref. [183] (theory 2). The outcome of the two models and the measured values of the IX lifetime as a function of bias are shown in Fig. 5.9. A very good agreement between the experimental data (purple circles) and theory 2 (solid blue line) is found, while the theory 1 (dashed red line) prediction is slightly offset in bias. The curves calculated by the two models overlap at small electric fields, but the data

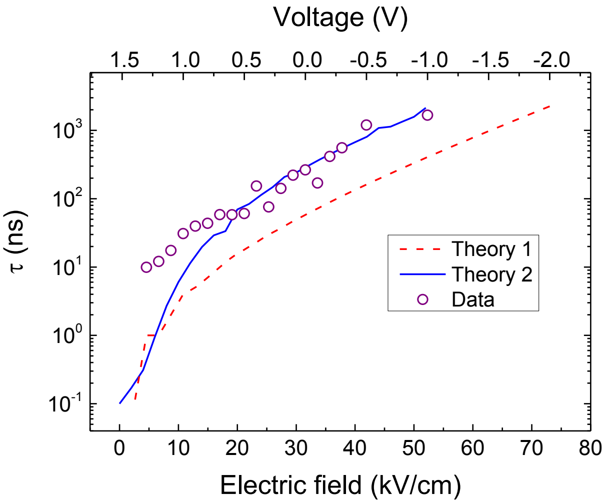

Figure 5.9: Radiative lifetime of the IX as a function of electric field. The experimental data (purple circles) is extracted from the data in Fig. 5.8 and compared to two theory models. Theory 1 (dashed red line) is a model used in this thesis to calculate the eigenstates of the CQWs and theory 2 (solid blue line) is provided in Ref. [183]. A very good agreement between the data and theory 2 is found above the built-in electric field. The deviation from the theoretical prediction close to zero field is due to imperfections of the p-i-n diode and charge-carrier tunnelling.

values there seem to deviate from the predicted behavior. The explanation for such a discrepancy is that the finite resistance of the ohmic contacts and the tunnelling of charge carriers prevents from compensating the built-in electric field, and the actual field dropping across the CQWs is larger, while the theory assumes perfect contacts. Also note that the values extracted for the electric field above 36 kV cm^{-1} must be treated with care due to an incomplete photoluminescence decay that have put constraints on the fitting routine.

The long lifetime of the IX reached at large electric fields results in a particular shape of the transient photoluminescence intensity curve. Right after the excitation pulse is switched off, the emission intensity is quenched and a dip in the decay curve is observed, see curves > 34 kV cm^{-1} in Fig. 5.8(a). The dip is followed by a slow rise of the photoluminescence signal and a subsequent slow decay. The following explanation is suggested for this behavior: after the excitation pulse the photogenerated IXs are hot and take time to relax to $k \approx 0$ states, where they can recombine radiatively, hence the optically active population builds up within τ_r. At a pulse repetition rate of 2.5 MHz, the exciton population is reexcited again before recombining and obtains more energy, which lifts it into the states with large in-plane momentum, which are dark. This results in a dip of the emission intensity when the light pulse hits the sample.

5.3 The exciton Mott transition

A system of interacting electrons and holes can undergo a transition from an insulating phase to an ionized EH-plasma with increasing temperature or density. An insulating system of excitons

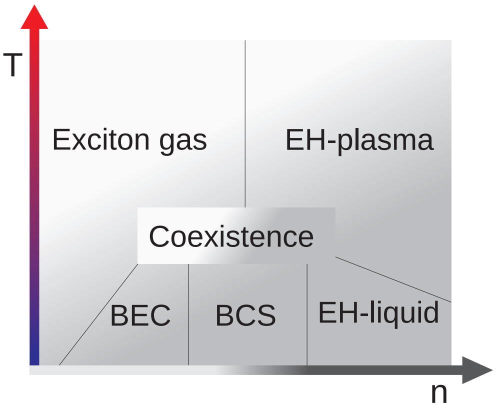

Figure 5.10: Schematic illustration of a phase diagram of electron-hole systems in semiconductors. In the low-temperature limit a BEC condensate can be observed for low-density exciton gas. Dense excitons might form a BCS-like state. At higher temperatures in the low-density limit excitons form classical gas and ionize into an electron-hole plasma as the density is increased. If cooled, the EH-plasma forms a Fermi liquid.

can be ionized thermally or by the screening of the Coulomb interaction between the electrons and the holes, while their density is increased. As said in the introduction of this chapter, this prediction was first formulated by Sir Nevill F. Mott more than fifty years ago [143], [11], and is known simply as the Mott transition. In this section, first, a brief overview of other phenomena observed in cold exciton gases is presented, and finally, the results on the Mott transition observed in the time-integrated photoluminescence of the IXs are reported. The findings of this thesis are compared to literature reports on the transitions between the metallic and insulating states of the electron-hole system in similar platforms.

5.3.1 Phenomena in cold exciton gases

Apart form the Mott transition, a number of other collective quantum effects can be observed in a system of cold exciton gases. This is due to the fact that the particle density in a cold excitonic system can be varied continuously, giving rise to interesting many-body quantum physics. Excitons have a rich phase diagram in the density-temperature phase space, which is sketched in Fig. 5.10. An important reference here is the low-density limit at zero temperature. It says that at zero temperature an electron and a hole will always bind into an exciton due to the Coulomb attraction, and the continuous growth of the number of free electrons and holes from zero value is not possible. At low temperature in the low-density limit, Bose-Einstein condensate (BEC) can occur, where excitons are hydrogen-like bosonic particles [169, 184]. When the mean interparticle distance becomes smaller than the exciton Bohr radius, the BEC state is predicted to evolve into a condensate similar to a Bardeen-Cooper-Schrieffer (BCS) superconducting state, except in this case the Cooper pair is not electrons of opposite spins but an electron-hole pair [185]. Apart from the BEC and BCS-like states, the low-density excitons can form a classical exciton gas at elevated temperatures or dissociate into an electron-hole plasma if the density of particles is increased. The dense electron-hole ensemble at very low temperatures shows high Fermi degeneracy and forms a condensed state, called the electron-hole liquid (EH-liquid) [186]. At medium densities and a certain region of low temperatures, a two-phase coexistence is possible such as liquid-like electron-hole droplets, which formation can be modelled as the nucleation process at a liquid-gas phase separation.

The BEC is expected to occur below temperatures where the exciton gas becomes quantum degenerate [9, 185]. It happens when the mean distance between the particles is comparable to the thermal de Broglie length ($\lambda_{dB} = (2\pi\hbar^2/mk_BT)^{1/2}$). For atoms in 3D, such temperatures correspond to fractions of a microkelvin.[3] Excitons in 2D GaAs with a density of $10^{10}\mathrm{cm}^{-2}$ and mass $M = 0.22m_e$ have $T_{dB} \sim 2.5\,\mathrm{K}$. The creation of the BEC requires access to temperatures of the exciton gas below a few Kelvin, which are, not without difficulty, within reach for conventional refrigeration systems. Generally, excitons might have higher temperature since they recombine before thermalizing with the crystal lattice. Long-lived and fast-cooling indirect excitons allow to fulfill thermal conditions for the BEC realization. BEC of IXs has been studied for more than a couple of decades [166, 167, 169, 187, 188]. Even though indubitable evidence of the IX BEC has not been provided yet, the tremendous efforts revealed other intriguing phenomena of the IXs, e.g., formation of nearly millimeter-sized spatial patterns in the exciton emission has been found and thoroughly investigated [189–191]. A crossover from BEC to the BCS-like state so far has been investigated in theory [192, 193]. At certain conditions a cold exciton gas can undergo a Mott transition, which is discussed next.

5.3.2 The Mott transition of indirect excitons

Two key parameters govern the Mott transition — excitation intensity and temperature. It is still debated in literature whether it occurs as a first-order phase transition or as a smooth function of the governing parameters, which implies a thermodynamic transition of second order. In the following this question is addressed experimentally in our CQWs, and the gradual transition of indirect excitons to an indirect EH-plasma is demonstrated as a function of the key parameters.

First, the data on the exciton Mott transition driven by the excitation intensity is presented in Fig. 5.11(a). During these measurements a constant electric field of $19\,\mathrm{kV\,cm^{-1}}$ is applied on a sample kept at a fixed temperature of 12.5 K. A doublet structure in the time-integrated IX photoluminescence is spectrally resolved. The IX spectrum is fitted with a sum of two Voigt functions, which takes into account the line-shape of the free excitons and the inhomogeneous broadening [194]. The resulting distributions are separated by 3.5–8 meV, which is comparable to the IX binding energy $E_b = 3.8\,\mathrm{meV}$ at a given electric field calculated for our structure using the code presented in Ref. [183]. The low-energy peak is attributed to excitons (red shading) and the high-energy peak to EH-plasma (blue shading). Other mechanisms, such as an interplay of defect-bound and free excitons, are ruled out in Sec. 5.3.5. At sufficiently low temperature and pumping power, the photo-generated carriers bind into excitons, which is reproduced in our data from Fig. 5.11(a). Increasing the pumping power results in more excitons being ionized, which

---

[3] For Rb^{87} atoms at $n > 10^{13}\mathrm{cm}^{-3}$ concentration with $m_{\mathrm{Rb}} = 1.5 \times 10^5 m_e$, the temperature for condensation is $T_{dB} \sim 100\,\mathrm{nK}$.

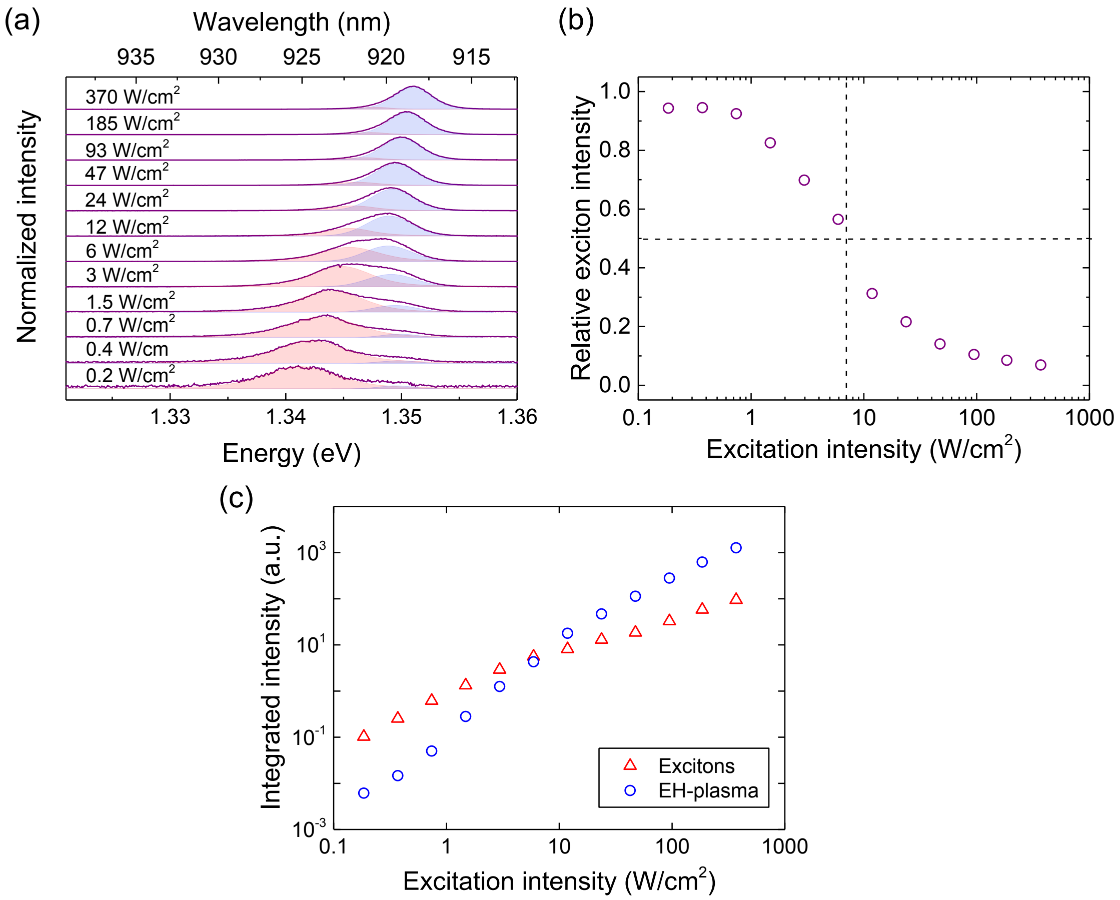

Figure 5.11: Dynamics of the exciton Mott transition as a function of excitation intensity. (a) Spectra of the IX taken at different pumping powers. At low powers the photoluminescence stems mainly from excitons (red), which is gradually overtaken by the EH-plasma (blue) at larger carrier densities. (b) Ratio between the emission intensity of excitons and the total signal extracted from (a). The crossover from an exciton- to a plasma-dominated population occurs at 7 W/cm^2. (c) The absolute intensity of the two species.

screen the electrostatic interaction between the remaining excitons and provide an avalanche process that facilitates the ionization of more excitons. This is seen in our spectra as a gradual enhancement of the plasma contribution. A continuous reduction of the excitonic population is observed as the excitation intensity is increased from 0.2 to 47 W/cm^2. In order to observe where the EH-plasma population overtakes the excitons, relative integrated intensity of the latter species is calculated from the fitted curves and plotted as a function of pumping power. The cross-over point occurs at 7 W/cm^2 excitation intensity as seen in the relative-intensity plot of the excitons in Fig. 5.11(b).

As Mott pointed out, a similar ionization process of excitons is expected to occur by keeping the pumping power fixed and increasing the temperature. The excitation intensity of 1.5 W/cm^2 is used, which corresponds to an exciton density of around 1.9×10^{10}cm^{-2} at 12.5 K. At low temperature

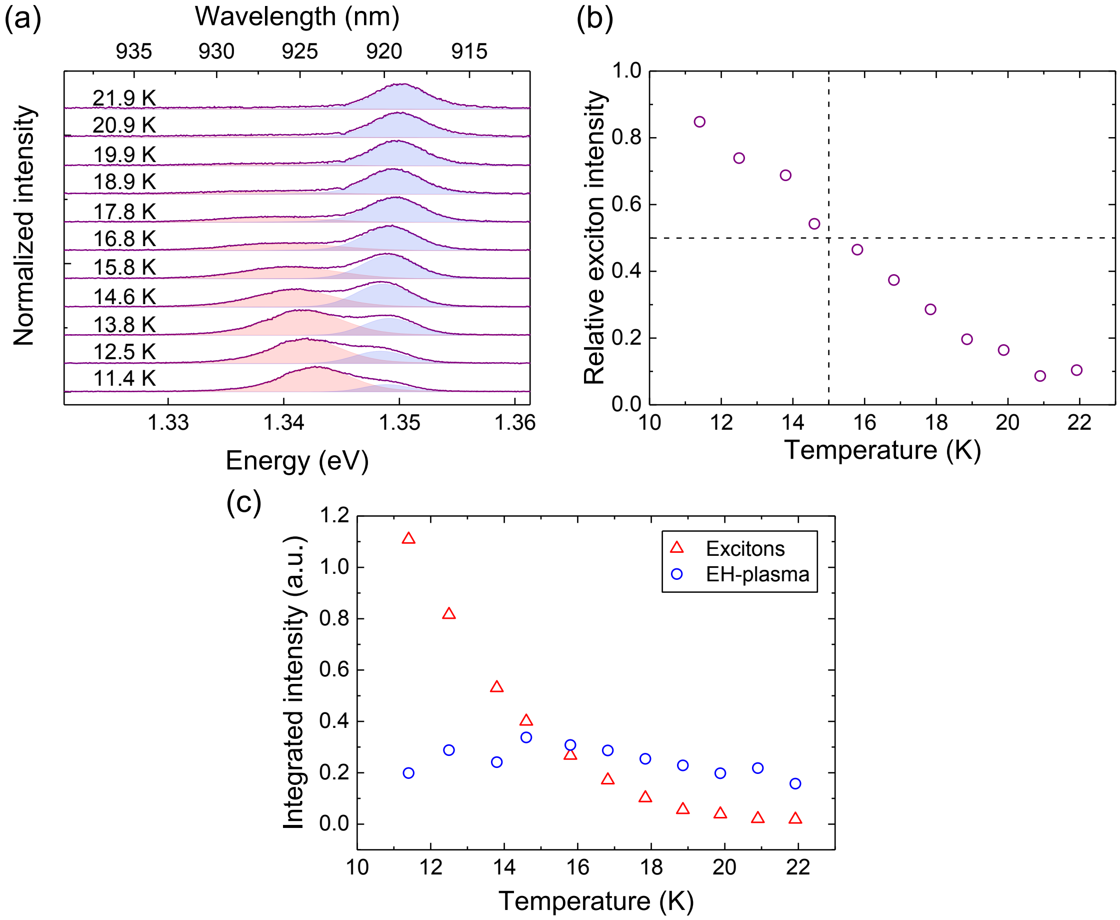

Figure 5.12: Dynamics of the exciton Mott transition as a function of temperature. (a) Spectra taken at different temperatures and at an excitation intensity of 1.5 W/cm^2. As the temperature is increased, the excitons ionize into free carriers. (b) Ratio between the photoluminescence stemming from the exciton resonance and the total signal extracted from (a). The crossover of the two populations occurs around 15 K. (c) The temperature dependence of the absolute intensity.

the photoluminescence is mainly due to free-exciton recombination. This situation corresponds to an excitonic gas that has a thermal energy lower than a typical binding energy of IXs in CQWs [183, 195]. With increasing temperature, free electrons and holes facilitate the ionization of the excitons until the Coulomb bonds are broken. This can be seen in our data as a continuous relative decrease of the excitonic signal with temperature, see Fig. 5.12. The excitonic peak is gradually inhibited due to thermal ionization as the sample is heated from 11.4 K to 21.9 K. We are therefore able to create the conditions required to induce the exciton Mott transition by tuning both the excitation intensity and temperature.

The fact that the IXs undergo a cross-over-like transition indicates that the exciton Mott transition in the CQWs is of second order. It is consistent with a theoretically predicted scenario that the exciton transition into a metallic state is associated with a smooth reduction of the exciton binding energy [158, 196, 197]. Several groups have provided experimental reports of the exciton transition between the insulating and the metallic states occurring gradually over a time scale of

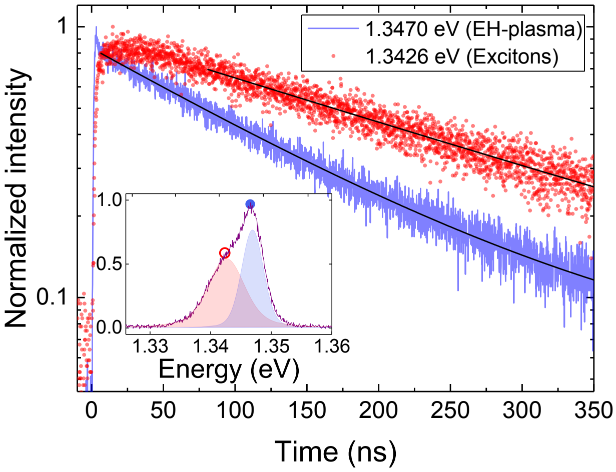

Figure 5.13: Time-resolved decay dynamics of excitons (red dashed line) and EH-plasma (blue solid line) taken at a pumping intensity of 1 W/cm^2. The curves are fitted well by a single (excitons) or double-exponential model (EH-plasma) (black solid lines). Inset: the corresponding spectrum of the indirect transition under pulsed excitation. The red circle and the blue dot denote the two spectral positions probed by the time-resolved measurement.

several hundreds of picoseconds [8, 152, 153]. In these experiments carriers above the QW band gap were created by picosecond pulses delivered with a time delay of more than 10 ns, and the carrier dynamics were probed by terahertz or time-resolved photoluminescence spectroscopy. However, periodic excitation with pulses prevents the excitonic system from reaching a steady state. In this context, the steady state means that the concentration of excitons is constant over the measurement time. It is expected that these steady-state excitons are able to thermalize. This corresponds to the usual assumption of thermal equilibrium, under which the exciton Mott transition is studied theoretically [155, 156, 159, 198–200], see also, e.g., Ref. [201] and references therein.

Experimentally, the steady state can be reached by generating the carriers with continuous excitation. These are the conditions for the time-integrated photoluminescence measurements on the CQWs reported in this thesis. Generally, in literature there is a lack of experimental study of the exciton Mott transition under steady-state excitation, with an exception of a work presented by Stern *et al.* [154]. Their study has been carried out on a GaAs/AlGaAs CQWs, where they reported an abrupt phase transition inferred from the time-integrated measurements of the exciton photoluminescence linewidth and the screening-induced energy shift. Our findings are in contrast with the behavior of the phase boundary reported in Ref. [154].

For completeness, time-resolved measurements on the two species populating the indirect transition are performed to study their decay dynamics. The measurements are recorded at two spectral positions corresponding to the central emission frequency of the two populations, see the inset of Fig. 5.13. At short delays a very fast emission decay of the EH-plasma (blue solid line) is observed and attributed to the phonon-mediated relaxation of the free-carriers into the exciton population. A fraction of the optically generated free carriers relaxes to the lowest-energy states and recombines radiatively as free excitons. The phase space is quickly filled with long-lived zero-momentum excitons and the rest of the electron-hole pairs recombine from higher-energy states. A faster decay of EH-plasma is observed with a rate of 6.6 μs^{-1}, whereas the excitons decay at a rate of 4.6 μs^{-1}. A decay of the mobile excitons slower than that of the free carriers has been reported in previous works on GaAs and InGaAs QWs, but with the lifetime of both types of population on the order of a nanosecond [153, 202]. The time-resolved study of the IX photoluminescence at early delays provides insight into the carrier dynamics right after the excitation pulse. The longer rise time of the excitonic peak reflects slow phonon-assisted thermalization of the excitons with high in-plane momentum into optically active excitons with $k \approx 0$. The emission from the EH-plasma reaches the maximum faster indicating that the hot charge carriers approach the band edges first before forming excitons and recombine radiatively.

5.3.3 Effective exciton density

The characteristic parameter of the Mott transition is the critical exciton density n_c at which the phase transition occurs. Here, n_c is defined as the total carrier density at which the amount of photoluminescence stemming from the exciton and EH-plasma peaks is the same. An equal intensity results in a roughly equal density of the two species because the emission area and the radiative decay rate have been measured to be about the same, see Fig. 5.14. In this work, n_c is estimated with two independent approaches: the so-called plate-capacitor model [203], and an independent procedure based on the CQWs steady-state optical absorption [204].

In the following, n_c is estimated using the plate-capacitor formula $E_{\text{cap}} = e^2 dn/\epsilon_0\epsilon_r$ [203], where e is the elementary charge, n is the exciton density, ϵ_r and ϵ_0 are the relative dielectric constant and the vacuum permittivity, respectively. IXs can be viewed as two layers of electrons and holes separated by d, defined as the distance between the expectation value of the electron coordinate $x_e = \int x|\psi_e|^2 \mathrm{d}x$ and the hole coordinate x_h. In the simplest approximation, d can be taken as the distance between the center of the two QWs $d \sim 14\,\text{nm}$.[4] The energy stored in the capacitor induces an energy shift of the IX emission and allows for a direct measure of the carrier density. Assuming a homogeneous exciton distribution, the exciton density n is proportional to the spectral blueshift ΔE of the IX:

$$n = \frac{\Delta E \epsilon_r \epsilon_0}{e^2 d}. \tag{5.1}$$

From the measured IX energy shift in the data presented in Fig. 5.11, the critical exciton density n_c of 2.3×10^{10} cm^{-2} at $T = 12.5$ K is obtained. Note that, as discussed by Ben-Tabou de-Leon *et al.* [205], the capacitor formula assumes uncorrelated electrons and holes without taking into account exciton-exciton interaction, and therefore, underestimates the exciton density by around 50% at densities of the order of 10^{10} cm^{-2}. Similar work on energy shifts including exciton-exciton interactions has been done by Boldt *et al.* [206]. Additionally, at higher temperatures the interaction

---

[4] More precisely, d can be evaluated from the shift of the exciton peak energy E_0 induced by an external electric field, expressed as $\Delta E \approx eFd \approx ef(V_{bi} - V)/l_i$, where f is the fraction of the voltage $V_{bi} - V$ dropping across l_i. By using a linear slope $\frac{\mathrm{d}E_0}{\mathrm{d}(V_{bi}-V)} = efd/l_i$ at low excitation power and assuming perfect ohmic contacts, such that $f \approx 1$, the separation between electron and hole layers is obtained as $d \approx \frac{\mathrm{d}E_0}{\mathrm{d}(V_{bi}-V)e} l_i$. For data in Fig. 5.11, $d = 15.2$ nm is obtained, which is very close to the interwell separation of 14 nm.

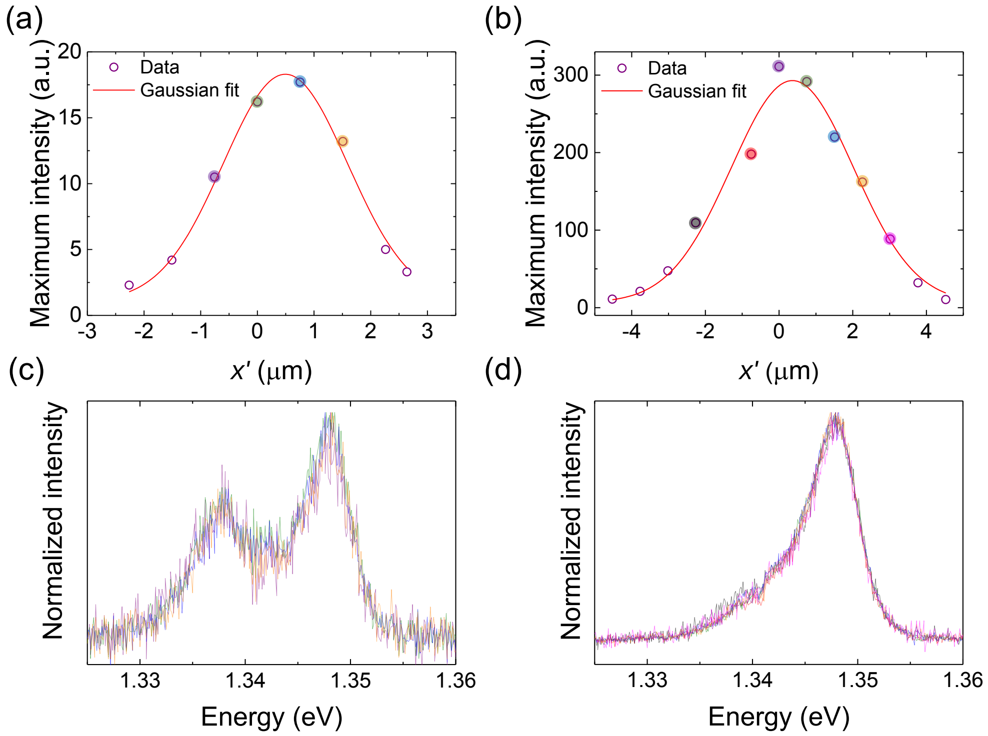

Figure 5.14: Spatial dependence of the photoluminescence spectra of the IX. Maximum emission intensity as a function of position x' relative to the excitation spot measured for an excitation intensity of (a) $1.1\,\mathrm{W/cm^2}$ and (b) $8.5\,\mathrm{W/cm^2}$ at $19\,\mathrm{kV\,cm^{-1}}$. The data is fitted with a Gaussian function (red line), from which the IX emission spot size is calculated. (c) and (d) Normalized emission spectra of the IX acquired at spatial positions indicated by the colored dots in (a) and (b), respectively. The ratio of the exciton and EH-plasma contribution to the photoluminescence does not vary spatially.

between excitons and electron-hole pairs gives a temperature dependent correction to the energy shift [197].

An additional procedure is used to estimate n_c based on a steady-state optical absorption of the CQWs [204]. The model presented in Sec. 5.1 is employed to calculate the CQWs absorption coefficient $\alpha = 1.2 \times 10^4\ \mathrm{cm^{-1}}$, which allows to estimate the number of the absorbed photons per time N_{abs} in the CQWs of thickness L yielding $N_{\mathrm{abs}} = \frac{P_i}{\hbar\omega}(1 - e^{-\alpha L})$, where P_i is the pumping power and ω the corresponding frequency. Multiplying N_{abs} with the radiative lifetime of the IX τ_{IX}, which is measured in Fig. 5.8(b), yields the steady-state number of excitons in the CQWs. The density of excitons n is expressed as:

$$n = \frac{P_i}{\hbar\omega}\frac{1}{A_{\mathrm{eff}}}(1 - e^{-\alpha L})\tau_{\mathrm{IX}}, \tag{5.2}$$

where A_{eff} is the IX emission area. The diffusion of the IXs is related to their lifetime, and thus, strongly depends on the electric field and the excitation power, which is why A_{eff} has to be measured in order to correctly estimate the exciton density for given values of these parameters. The IX emission area is measured by exciting the sample at a constant position and collecting

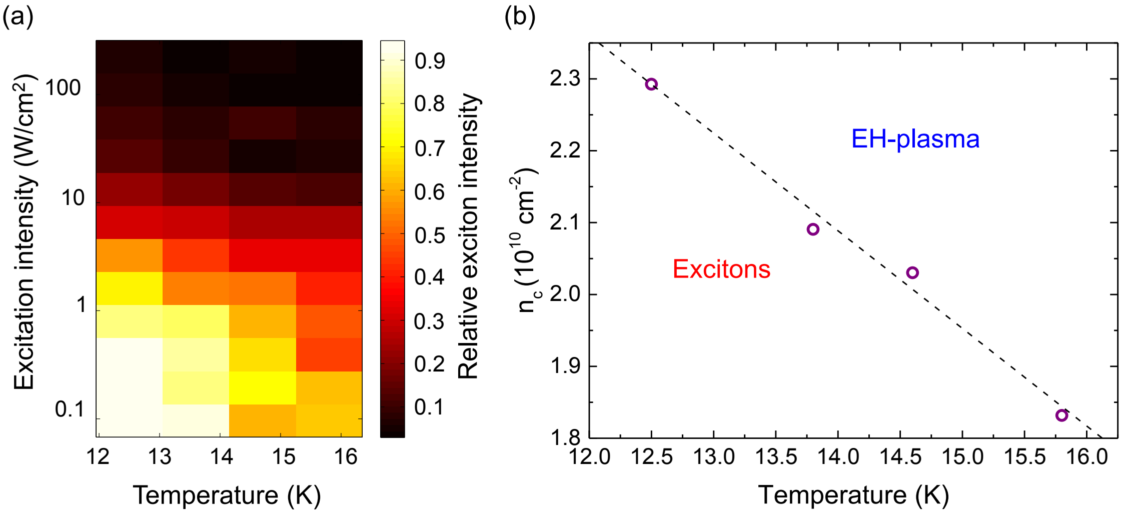

Figure 5.15: Phase diagram of the exciton Mott transition. (a) Relative exciton intensity as a function of temperature and excitation intensity. The insulating phase of excitons dominates the indirect transition at low temperature under weak optical excitation, whereas the transition is populated mainly by the metallic EH-plasma as the temperature or excitation power is increased. (b) Critical density n_c is estimated for each temperature (purple circles). Two regions are distinguished where either the insulating excitons or the metallic plasma dominates. The black dashed line is a linear fit $n_c = \zeta T + \xi$.

the photoluminescence from many different positions along a line, defined by the galvanometer mirror deflection. The details of the setup can be found in Chapter 2. The galvanometer mirrors are calibrated by measuring a spatial profile of a laser at 920 nm wavelength and comparing it to a diffraction-limited spot size. The maximum emission intensity of the IX is plotted as a function of position x' and fitted with a Gaussian curve to extract a half-width half-maximum, δ, see Fig. 5.14(a) and (b). Assuming a round spot, the area is calculated from $A_{\text{eff}} = \pi\delta^2$.

By using Eq. (5.2), $n_c \sim 1.2 \times 10^{10}$ cm^{-2} at 12.5 K is obtained. The two independent estimations of n_c differ by a factor of about 2, which is likely caused by the fact that excitons with high in-plane momentum are optically dark and are not captured by Eq. (5.2). Therefore, the value of n_c calculated by Eq. (5.1) is employed, which agrees well with the estimations for GaAs/AlGaAs and InGaAs/GaAs QWs reported in literature, where the exciton Mott transition was found to occur at n_c of the order of 10^{10}–10^{11}cm^{-2} and temperatures below 10 K [8, 152–154]. We point out that in this work the sample temperature is measured accurately on the same surface that the sample is mounted, which is a few Kelvin higher than the cold-finger values, usually reported in literature.

5.3.4 Phase diagram

To complete the picture of the exciton Mott transition, a phase diagram of the transition is provided in Fig. 5.15. A color-coded map of the integrated intensity of the excitonic peak relative to the total IX intensity in the phase space of temperature and excitation intensity is shown in Fig. 5.15(a). By linear interpolation for each temperature value the critical density n_c is found and plotted in

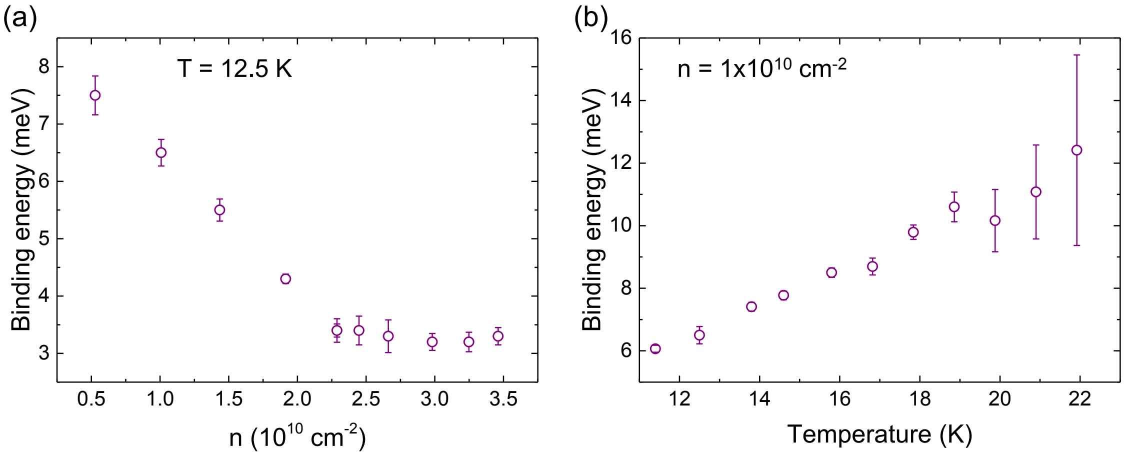

Figure 5.16: Binding energy of the IX across the Mott transition extracted from data shown in Figs. 5.11(a) and 5.12(a). (a) As the carrier density n is increased the binding energy of the IX is reduced due to screening of the Coulomb interaction. (b) E_b behavior with temperature. At the carrier density of 1×10^{10}cm^{-2} and at 12.5 K, the binding energy E_b is 6.5 meV and becomes larger with increasing temperature. The error bars are calculated from the fitting errors of the centers of the exciton and EH-plasma distributions.

Fig. 5.15(b). The phase boundary is defined by n_c, which divides the diagram into two regions with exciton- or EH-plasma-dominant populations. The boundary can be well approximated by a straight line $n_c = \zeta T + \xi$ with $\zeta = -0.137\text{K}^{-1}\text{cm}^{-2}$ and $\xi = 4 \times 10^{10}\text{cm}^{-2}$, where n_c is measured in 10^{10}cm^{-2} and T in K. The diagram partially agrees with the theoretical prediction from Refs. [156], [207]. In Ref. [207], the relative fraction of excitons in a GaAs QW is calculated using the mass-action law in equilibrium and the static screening approximation, whereas Nikolaev *et al.*[156] use the Green's function formalism to calculate the phase diagram for a CQWs. The picture is qualitatively similar in both works with an insulating state of excitons dominating in the low density-low temperature regime and a transition into the electron-hole plasma occurring with an increase in one of the key parameters. Our results map out a rather restricted part of the suggested phase diagram where the carrier density-temperature relation is approximately linear. The limits of the phase boundary curve can be compared to theory using the model presented in Ref. [156]. For our CQWs, with a binding energy of the IX of 3.8 meV and assuming a Bohr radius of 14 nm, the exciton Mott transition is found to occur between 8.8–15.5 K and 1.5–5 × 10^{10}cm^{-2}, which is in good agreement with our experimental phase diagram. Additionally, our phase boundary curve is compared with the linear part of the curve presented by the dashed line in Fig. 6 in Ref. [207] and a close match of the carrier density is found. However, the theory predicts transition temperatures lower by around 6 K compared to our data. Overall, our data reproduce well the main features of the predicted dynamics, but no sharp boundary between the insulating and the metallic states is observed. Instead, the transition from the state with 90 to 10% excitonic population occurs as the exciton density increases two times from 1.5×10^{10} to 3.1×10^{10}cm^{-2} at 12.5 K. With increasing temperature, the excitonic population reduces from 90 to 10% as the sample is heated from 10.9

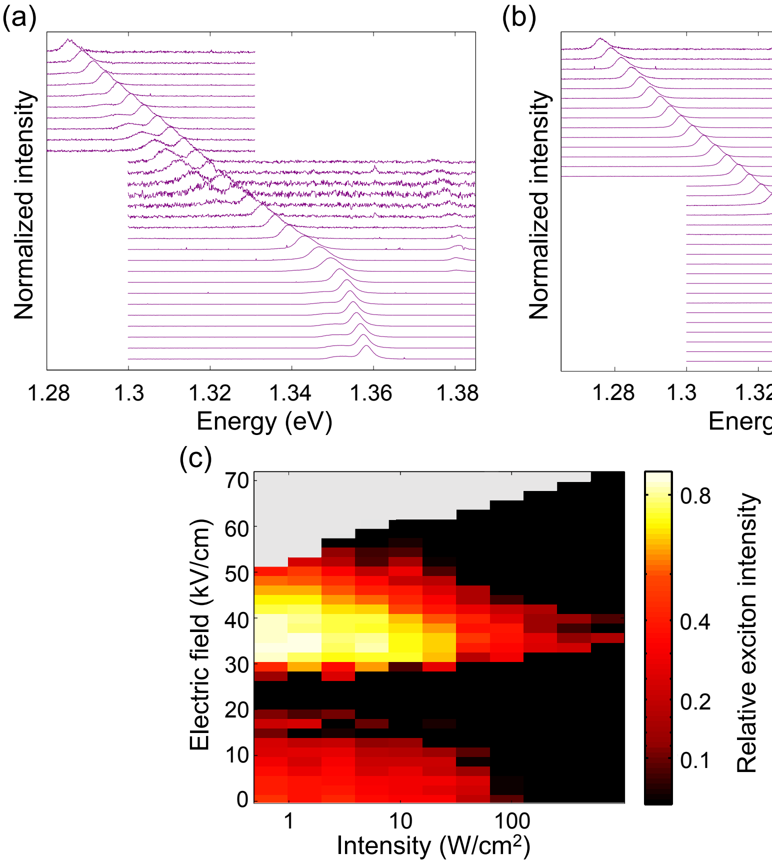

Figure 5.17: Power-voltage phase diagram of the Mott transition in the CQWs. (a) and (b) Waterfall plots of the CQWs photoluminescence taken at an excitation intensity of 4.3 W/cm^2 and 136.2 W/cm^2, respectively. The data curves from bottom to top are acquired at an electric field increased accordingly from 2.5 to 69 kV cm^{-1}. (c) A colormap of the relative exciton intensity in the electric-field-power coordinates at 12.5 K. The gray colored area shows where no data is recorded due to a complete quenching of the photoluminescence.

to 21.7 K at $n = 1.9 \times 10^{10}$cm^{-2}. A smooth transition between the metallic and the insulating states probed in a picosecond-time scale has been reported in experiments on QWs but under ultrashort-pulsed excitation, which implies a non-equilibrium excitonic population [8, 153].

The gradual ionization of excitons is in consensus with the prediction of a continuous reduction of the exciton binding energy associated with the Mott transition [158, 196, 197]. Therefore, knowledge of the behavior of the IX binding energy as a function of the governing parameters would shed light on the dynamics of the exciton Mott transition. The IX binding energy E_b is extracted from Figs. 5.11(a) and 5.12(a) as the energy difference between the exciton and EH-plasma distributions. We emphasize the difficulty to precisely extract the center of the excitonic distribution at high excitation powers and temperatures. The binding energy E_b reduces as the carrier density increases, see Fig. 5.16(a), as expected due to a carrier-induced screening of the Coulomb attraction between an electron and a hole. A very good agreement is found when comparing our data with a theoretically predicted behavior of E_b at 65 K as a function of the free-carrier density [155]. It has been suggested that the binding energy should be reduced by a smaller extent as the temperature increases since hot carriers screen less efficiently [155]. In our case, however, an interesting increase of E_b is observed as a function of temperature, see Fig. 5.16(b).

Additionally, the exciton Mott transition is investigated in a phase space of electric field and excitation intensity. A corresponding phase diagram at 12.5 K is shown in Fig. 5.17. The data used for the phase diagram is collected using an objective of NA = 0.6, which collects the IX photoluminescence from a smaller spot. Therefore, the experimental conditions should not be directly compared with those of NA = 0.25. The representative data sets acquired at the excitation intensity of 4.3 W/cm^2 and 136.2 W/cm^2 are shown in Fig. 5.17(a) and (b), respectively. The phase diagram reveals two regions where the excitonic and the free-carrier populations coexist in the indirect transition. The first transition region is in the reverse-bias regime corresponding to an electric field of around 35 kV/cm. Close to zero electric field, another region is observed where the excitons also coexist with the EH-plasma, but due to a shorter IX lifetime, the effective density is reduced and the excitonic population does not dominate even at lowest excitation intensities. The electric field influences many system parameters, which makes it a nontrivial task to evaluate its impact on the transition regime quantitatively.

5.3.5 Ruling out of alternative mechanisms

In the present chapter the exciton Mott transition in the behavior of the IX photoluminescence spectra has been observed and studied. Since this effect occurs in a solid-state environment, which hosts a plethora of physical phenomena, it is essential to rule out alternative mechanisms that may explain our data. A possible mechanism is the interplay of localized and free excitons [208, 209]. The localized excitons are caused by doping impurities or fluctuations in the quantum-well thickness [208, 210, 211], which form random localized traps for the excitons, or can be created by external lateral electric fields [208]. These traps are saturated with relative ease due to Pauli exclusion [208, 209] at carrier densities of the order of 10^9cm^{-2} below 2 K [168, 212], and at even lower densities for higher temperatures [213]. In our measurements, however, the low-energy peak does not reach saturation even at carrier densities of the order of 10^{11}cm^{-2}. Additionally, sharp features are expected in the photoluminescence spectrum due to the spectrally narrow density of states of the trapping sites [208, 211]. In our case, no such features or changes in the substructure are present in the spectrum even at the smallest excitation intensities.

Another reason for a doublet structure in the spectrum of the indirect transition may be related to QWs of different thicknesses. Due to a finite growth accuracy, the layer thickness might fluctuate by an atomic monolayer. For our CQWs a fluctuation of one monolayer results in an energy shift of around 1.5 meV, and one-monolayer deviation in the barrier thickness b induces a shift of less than 1 meV. Since the energy difference between the two resonances of the indirect transition varies between 6–10 meV, it is concluded that this effect cannot explain our data.

Other possible mechanisms like thermally activated high-energy states are excluded, since the energy difference between the ground state and the first excited exciton state is much larger than the spectral separation in the indirect doublet.

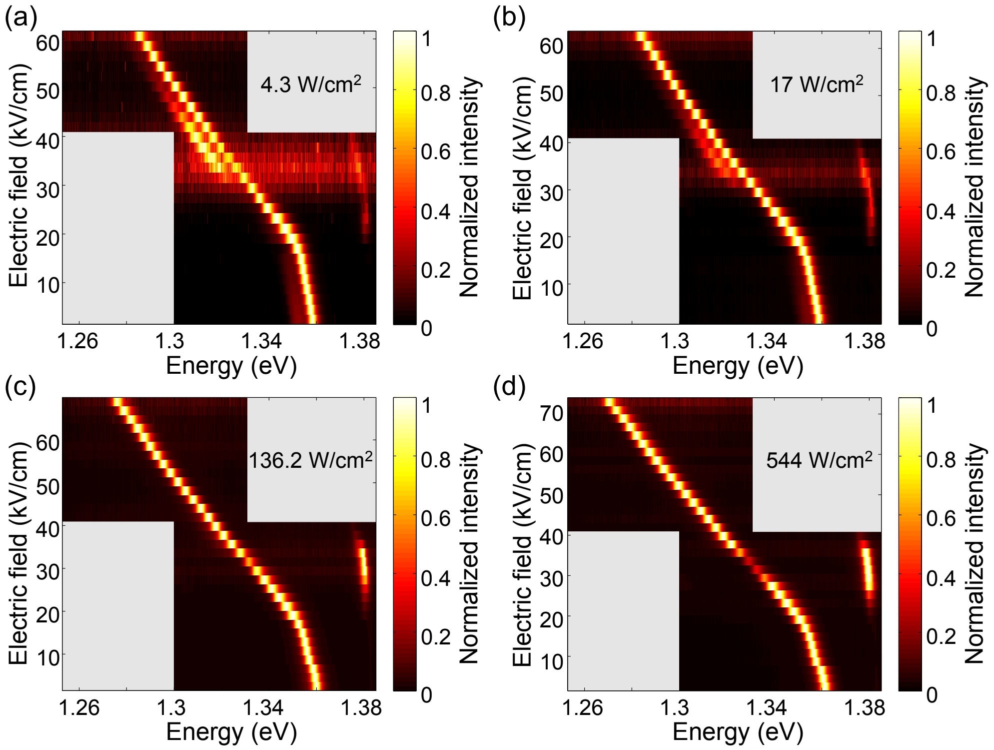

Figure 5.18: Dynamics of the IX and DX photoluminescence intensity versus electric field. (a)–(d) Color-scale plots of a normalized emission intensity of the CQWs as a function of electric field recorded at an excitation intensity of 4.3, 17, 136.2 and 544 W/cm^2, respectively. At the electric-field values of around 30 kV/cm the DX peak becomes several times brighter than the IX peak at hight excitation powers. Gray squares show where no data is taken due to a complete quenching of the photoluminescence.

5.4 The role of dark excitons

The properties of an IX photoluminescence depend strongly on the electric field, as already demonstrated in Sec. 5.2. The external electric field can be used to tune the absorption and the band diagram of the CQWs, which set the dynamics of the radiative transitions. Our findings on the CQWs behavior when the applied bias is varied are discussed in more detail. The electric-field dependency of the CQWs emission recorded at a varied excitation intensity is shown in Fig. 5.18. A surprising interplay of the IX and the DX emission intensity at the electric-field values of 20–40 kV/cm is observed as the excitation power is increased. The recombination of an excited state of the system, the DX, is detected by the spectral measurements and becomes much more intense than the IX. Moreover, the absolute photoluminescence intensity of both the direct and the indirect transition drops considerably in this region, as shown in Fig. 5.19. These features are reproducible at all values of excitation intensity and temperature used in this work. The following mechanism is proposed to be responsible for the dominant role of the DX. Since the IX lifetime and the energy gap between the 2D states is increased greatly by the electric field, the system can turn into a regime where the absolute power cannot be released solely from the IX. In this case, the rate of

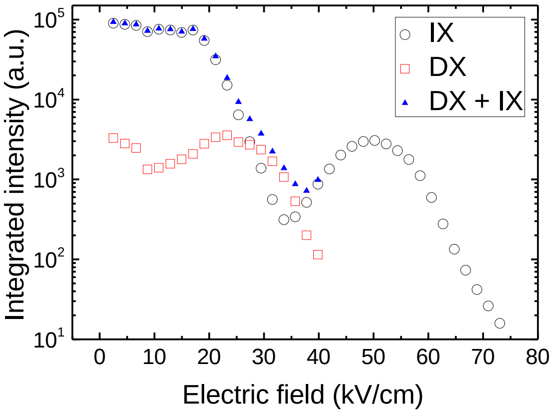

Figure 5.19: Quenching of the photoluminescence as a function of bias. The electric-field-dependent integrated intensity stemming from the indirect and direct transitions at 544 W/cm^2 excitation intensity. The total emission intensity (blue triangles) drops significantly above the built-in field and increases again at larger electric fields. We suggest that at this particular band alignment a large population of dark excitons is present in the system.

the IX recombination is too slow to drain the population of the ground state and the first excited state becomes populated and appears as the DX peak in the spectrum. However, this process does not explain the drop of the absolute photoluminescence intensity. The observed features cannot be due to carrier escape from the QWs since the tunnelling rate is negligible, and no increase in the photocurrent is measured in this regime. Therefore, it is suggested that the dark excitons are responsible for the quenching of the photoluminescence. Theory predicts the excitons to have optically bright and dark states, where the dark state lies slightly lower in energy [214]. A fraction of excitons in such a state might contribute to the reduced photoluminescence, but it is surprising why the population of the optically inactive excitons would play an important role only at certain electric fields. This effect might deserve further study.

5.5 Conclusions

In the present chapter, a study of the Mott transition in CQWs is presented and reveals a gradual ionization of the IX with increasing carrier density and temperature. The critical density n_c of $2.3 \times 10^{10}\text{cm}^{-2}$, at which the transition occurs, is extracted, and a good agreement with previously reported values is found. Calculating n_c enables to build a density-temperature phase diagram, which is a desired tool for gaining insight into the thermodynamics of the Mott transition. The phase diagram reveals no sharp boundary between the insulating and the metallic states implying a continuous reduction of the exciton binding energy E_b due to thermal ionization and free-carrier screening. Alternative mechanisms that could explain the observed scenario are discussed and ruled out by analysing the saturation behavior and the relative spectral position. Additionally, a peculiar darkening of the IX photoluminescence at a certain bias is observed. It is suggested that this feature is due to the formation of dark excitons. Moreover, the electric field turns out to induce an interplay between the photoluminescence of the DX and IX. We hope that our results will encourage further theoretical effort dedicated to research the behavior of IXs in the Mott regime.

Appendices

Appendix A

Fabrication of photonic-crystal membranes

For experiments described in this thesis, PhC devices are fabricated on three types of GaAs wafers, which layer structure is shown in Fig. 3.2 (Chapter 3), Fig. 5.2 (Chapter 5), and Fig. A.1 below. The wafer in Fig. A.1 was grown at the Korea Institute of Science and Technology, Seoul, Korea. The samples from the wafer with the doped GaAs layers are first processed by defining a mesa structure and depositing ohmic contacts. Afterwards, the PhC structure fabrication takes place, which is the same for samples from the wafer with an intrinsic GaAs membrane (Fig. A.1).

The fabrication procedure consists of the following steps.

1. **Mesa preparation**

   a) Sample preparation: Clean a sample by flushing it with acetone, methanol, and isopropanol (IPA) and blow dry with N_2. Dehydrate by baking it for 5 min at 185 °C

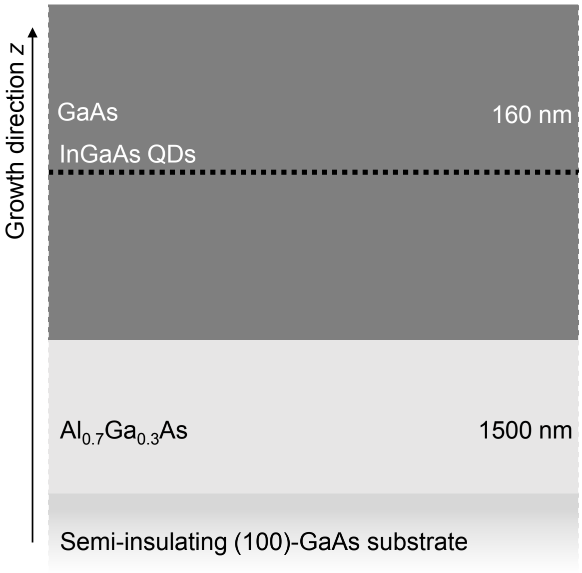

Figure A.1: A layer structure of the wafer used for fabricating the glide-plane ring cavities. An InGaAs QD layer is embedded into an intrinsic layer of GaAs.

   (optional).

   b) Spin-coating: Apply several droplets of a photoresist AZ1505 and spin at 4000 rpm for 45 s. To prevent sticking clean the back of the sample by sliding it on the cleanroom wipe, mount on a piece of a silicon wafer and prebake for 45 s at 115 °C. This results in a resist thickness of ~ 500 nm.

   c) UV lithography: by using a Karl Suss MJB-3 mask aligner expose the sample through the appropriate mask. The exposure time can vary from 2 to 3 s depending on the depreciation of the UV lamp ($\lambda = 365\,\text{nm}$).

   d) Development: Immerse the sample into a developer AZ400K:H_2O (1:4) for 25 – 30 s, rinse in millipore water and blow dry with N_2. Postbake for 45 s at 115 °C.

   e) Nonselective etching: Prior to etching remove residuals of resist by O_2-plasma ashing for 20 s. Prepare a solution of H_3PO_4:H_2O (1:5) for deoxidation and a solution of H_3PO_4:H_2O_2:H_2O (1:4:45) for nonselective etching. An exothermic reaction takes place when mixing these solutions, therefore, it needs about 20 min to cool to room temperature (for a volume of < 0.5 L). Dip the sample into the deoxidising solution for 20 s, rinse in millipore water, and dip in the etching solution for an appropriate amount of time. This solution typically etches GaAs and low Al content AlGaAs with a rate of 5 – 6 nm/s. The etching rate can be calibrated by measuring the etch depth with a profiler. For the mesa structure one needs to terminate the etching a few nanometers above the n-dopes GaAs layers by rinsing the sample in millipore water and blow drying with N_2.

   f) Photomask removal: After etching the photoresist is removed by immersion in acetone for several minutes.

Once the mesa structure is prepared, ohmic contacts are deposited by a three-step process for each type of contacts: UV lithography, metal evaporation, and lift-off. In the following, these steps are described in detail.

2. **UV lithography for ohmic contacts I: negative-tone resist**

   a) Sample preparation: as before.

   b) Spin-coating: Apply several droplets of a negative resist ma-N400 and spin at 4000 rpm for 45 s. This resist is more viscous than AZ1505, therefore, it is more important to clean the back of the sample by sliding it on the cleanroom wipe to avoid sticking. Prebake at 90 °C for 5 min. This results in a resist thickness of ~ 7 µm.

   c) UV lithography: Expose the sample through the appropriate mask for 110 s.

   d) Development: Immerse the sample into a developer ma-D332/S for 90 s, rinse in millipore water and blow dry with N_2. A reentrant profile of ~ 2 µm-wide is obtained.

3. **UV lithography for ohmic contacts II: double-layer lithography**

   a) Sample preparation: as before.

  b) Spin-coating I: First, spin the sample with a resist LOR3B at 4000 rpm for 45 s. Clean the back of the sample by sliding it on the cleanroom wipe to avoid sticking, which can be very strong for this resist. Prebake for 2.5 min at 185 °C. This results in a reentrant profile of $\sim 1\,\mu$m.
  c) Spin-coating II: Spin AZ1505 at 4000 rpm for 45 s. Clean the back of the sample as before. Prebake for 45 s at 115 °C.
  d) UV lithography I: If size allows, expose the edges of the sample for 60 s to remove edge beads. This helps to improve the contact between the mask and the sample for subsequent exposures.
  e) Development: Immerse the sample into a developer AZ400K:H_2O (1:4) for 45 s, rinse in millipore water and blow dry with N_2.
  f) UV lithography II: Expose the sample through the appropriate mask for 10 s.
  g) Development: Immerse the sample into a fresh developer AZ400K:H_2O (1:4) for 25 s, rinse in millipore water and blow dry with N_2.

4. **UV lithography for GaAs bridges: image-reversal resist**
  a) Sample preparation: as before.
  b) Spin-coating: Spin the sample with a resist AZ5214E at 8000 rpm for 100 s. This results in a resist thickness of $\sim 1\,\mu$m.
  c) Exposure for negative-tone: Prebake at 90 °C for 2 min, expose through an appropriate mask for 2 s, bake at 120 °C for 2 min and expose without a mask (flood) for 20 s.
  d) Development for negative-tone: Immerse in a developer AZ726MIF for 30 – 40 s, rinse in IPA and blow dry with N_2. This results in a reentrant profile of $\sim 1\,\mu$m.
  e) Exposure for positive-tone: Prebake at 90 °C for 2 min, expose through an appropriate mask for 10 – 12 s.
  f) Development for positive-tone: Immerse in a developer AZ726MIF for 25 s, rinse in IPA and blow dry with N_2.

In a usual procedure, first, metals for n-type ohmic contacts are deposited on the sample in a house-made e-beam evaporator. After lift-off, the n-type contacts are annealed in a rapid thermal annealer (RTA) (Allwin 21). Metals for the p-type contacts are deposited either in the e-beam or in a thermal evaporator (Edwards) depending on the used materials. Thermally deposited contacts are annealed in a house-made thermal furnace after lift-off.

5. **Deposition of n-type ohmic contacts**
  a) Sample preparation: Before metal deposition remove resist residues by ashing in O_2 plasma for 20 s and deoxidise the sample by dipping it into a solution of H_3PO_4:H_2O (1:5) for 2 min. Rinse in millipore water and blow dry with N_2.

   b) Metal e-beam evaporation: Deposit the following sequence of metals: 5 nm of Ni, 40 nm of Ge, 60 nm of Au, 27 nm of Ni and at least 100 nm of Au.

6. **Deposition of p-type ohmic contacts I: AuZn**

   a) Sample preparation: as before for the n-type contact deposition.

   b) Thermal evaporation: Deposit the following sequence of metals: 20 nm of Au, 50 nm of Zn, and at least 100 nm of Au.

7. **Deposition of p-type ohmic contacts II: TiAu**

   a) Sample preparation: as before for the n-type contact deposition.

   b) E-beam evaporation: Deposit the following sequence of metals: 50 nm of Ti and 150 nm of Au.

8. **Lift-off**

   a) Lift-off for the negative-tone resist: Prepare a beaker with a teflon holder immersed in acetone such that the sample is exposed only to acetone vapor. Keep the beaker covered for 1 h, flush the sample with acetone, and blow dry with N_2.

   b) Lift-off for the double-layer resist: Immerse the sample into n-methyl-2-pyrrolidone (NMP) and leave it overnight.

9. **Thermal annealing**

   a) Annealing for the n-type contacts: Anneal the sample in RTA for 40 s at 420 °C in a forming gas atmosphere.

   b) Annealing for the p-type contacts: Anneal the sample in the thermal furnace for 60 s at 450 °C in a N_2 atmosphere. Note that the TiAu contacts are not annealed.

10. **Contact protection**

    a) Spin-coating and UV lithography: Perform steps (a)–(d) from the mesa preparation routine. Use the UV mask for the contact protection. Asher in O_2-plasma for 20 s.

    b) Hard-bake: Bake the sample for 30 min at 185 °C.

Fabrication procedure of the PhC structures on both gated and intrinsic samples consists of e-beam lithography, ICP etching, and wet chemical processing described below.

11. **E-beam lithography**

    a) Sample preparation: Clean a sample by flushing it with acetone, methanol, and isopropanol (IPA) and blow dry with N_2. Dehydrate by baking it for 5 min at 185 °C (optional).

b) Spin-coating: Apply a few droplets of an e-beam resist ZEP520A and spin at 2000 rpm for 60 s. Clean the back of the sample by sliding it on the cleanroom wipe to avoid sticking. Prebake at 185 °C for 5 min. This results in a resist thickness of $\sim 530\,\mu\text{m}$, which is measured with a film-thickness monitor. Deviations of $\pm 20\,\text{nm}$ do not require readjustment of the exposure dose.

c) E-beam exposure: Expose a desired design with an appropriate dose (current of 100 pA and 40 µm aperture is used). For PhC structures $\sim 400\,\mu\text{C/cm}^2$ is needed when o-xylene is used for development, and $\sim 300\,\mu\text{C/cm}^2$ ($\sim 230\,\mu\text{C/cm}^2$) is enough for development of features smaller (larger) than a few hundreds of nm in n-amyl acetate (ZED-N50).

d) Development I: Immerse the sample in o-xylene for 20 s, rinse in IPA, and blow dry with N_2.

e) Development II: Immerse the sample in a developer ZED-N50 for 60 s at 20 – 25 °C, rinse in IPA for 10 s, and blow dry with N_2. Note that precipitation of flake-like particles occurs in ZED-N50 below 20 °C, which might contaminate the sample.

After processing the sample with the e-beam lithography, the pattern is transferred from the soft-mask into the GaAs layer by dry-etching via inductively coupled plasma (ICP) in a PlasmlabSystem 100 ICP65 (Oxford Instruments) etcher.

12. ICP etching

a) Sample preparation: Mount the sample on a Si carrier wafer wetted with a drop of Fomblin oil to ensure thermal contact.

b) Etching for PhC structures: Etch the sample with a gas mixture of $BCl_3/Cl_2/Ar$ with respective flows 3/4/25 sccm at chamber pressure of 4 mTorr, the ICP power of 300 W and table temperature of 0 °C. The DC bias should be around 310 – 315 V. After etching, clean the back of the sample from the Fomblin oil to avoid pollution during the subsequent wet processing.

c) Deep etching for large structures: Etch the sample with a gas mixture of BCl_3/Ar with respective flows 3/10 sccm at chamber pressure of 10 mTorr, zero ICP power and table temperature of 15 °C. The plasma strike pressure is set to 30 mTorr. After etching, clean the back of the sample from the Fomblin oil to avoid pollution during the subsequent wet processing.

The final step of the PhC membrane fabrication involves stripping of the e-beam resist, selective etching of the AlGaAs sacrificial layer, a cleaning procedure to remove byproducts of chemical reactions with HF and drying in a Leica EM CPD300 (Leica) critical point dryer.

13. Underetching and cleaning

a) Stripping the resist: Immerse the sample into NMP at 60 °C for 10 min, then clean it agitating gently for 2 min in a room temperature NMP. Rinse the sample in IPA and blow dry with N_2.

b) Cleaning step 1: Immerse the sample in a solution of KOH:H_2O 25 g/100 mL for 5 min. The solution is prepared in advance to be able to cool to room temperature due to exothermic reaction. Rinse the sample in fresh millipore water and blow dry with N_2.

c) Underetching: Etch the sample in a 10% solution of HF for 45 s agitating slowly. For the next steps, care must be taken when transferring the sample from one liquid to another in order to prevent damage from capillary forces. The sample must be kept horizontal to maintain a liquid drop on top of it. The underetching is terminated by immersing the sample in fresh millipore water for 5 min.

d) Cleaning step 2: Dip the sample in a 30% (w/w) solution of H_2O_2 for 1 min. Rinse in fresh millipore water for 1 min.

e) Cleaning step 3: Immerse the sample in a fresh solution of KOH:H_2O 25 g/100 mL for 2 min. Rinse in fresh millipore water for 1 min.

f) Drying: Dip the sample in IPA, place it into the sample holder of the CPD, and run the drying process. Samples without fragile ridge structures, e.g., PhC cavities, can be dried in a fume hood by letting the droplet of IPA evaporate naturally.

Appendix B

Electrical sample mount

To accommodate samples with electrical contacts a custom sample holder has been made[1]. The holder design has been implemented in a liquid-helium flow cryostat, but is compatible with other cryostats, e.g., bath and closed-cycle, as well. Images of the sample holder installed in the flow cryostat chamber are shown in Fig. B.1. The main parts of the holder are sketched in Fig. B.1(a) and assembled as follows. A customized copper cold-finger (1) is placed in the cryostat and tightened with a couple of screws. A radiation shield (2) is modified to accommodate a printed circuit board (PCB) made in-house (3), which is mounted on the cold-finger allowing it to protrude through the square cutout in the middle. A leadless-chip-carrier (LCC) socket (Image sensor 0.050 pitch 44 pin LCC socket, Andon Electronics Corp.) (4) is mounted on the PCB and secured by soldering the socket terminals to the PCB traces with leadless soldering iron. The socket is used to mount an LCC sample holder (5), which is the only removable part in the assembly. Figure B.1(b) shows the permanent installation inside the cryostat. The PCB is connected to a 10-pin built-in teeth PCB (6), which provides electrical feedthroughs to room environment. Low thermal conductivity wires (Phosphor bronze (Cu94/Sn6) polyimide insulated wire, 36 AWG[2], Goodfellow) are used to establish this connection (7). Such wires together with manganin (Cu83/Mg13/Ni4) and nichrome (Ni80/Cr20) wires owing to their low thermal conductivity ($< 5\,\mathrm{W\,m^{-1}\,K^{-1}}$ at $10\,\mathrm{K}$) are among the best options for cryogenic applications when heat load is to be avoided. However, the latter two types of wires contain Ni and thus are not desired for applications, where magnetic fields are involved. The removable part of the sample holder contains a nickel-free LCC (44 LCC package, Kyocera), which is modified by drilling a hole in the middle of the carrier and inserting a specially designed copper piece (8), see Fig. B.1(c). The copper piece is glued with epoxy resin to the LCC. The samples are glued with silver glue on this copper inset and wire bonded to the contact pads on the LCC, as shown in Fig. B.1(c). The surface of the cold-finger and the back of the copper inset are cleaned with isopropanol and cleanroom wipe to remove dust and grease. To enhance the mechanical contact area, n-grease is applied on each surface. The LCC is then pressed into the socket and fastened to the cold-finger with a screw to ensure thermal contact. In a typical cryostat

---

[1] The design of the holder has been inspired by the solution proposed by Montana Instruments, which can be found on www.montanainstruments.com.

[2] American wire gauge standard, 36 AWG $\approx 0.125\,\mathrm{mm}$.

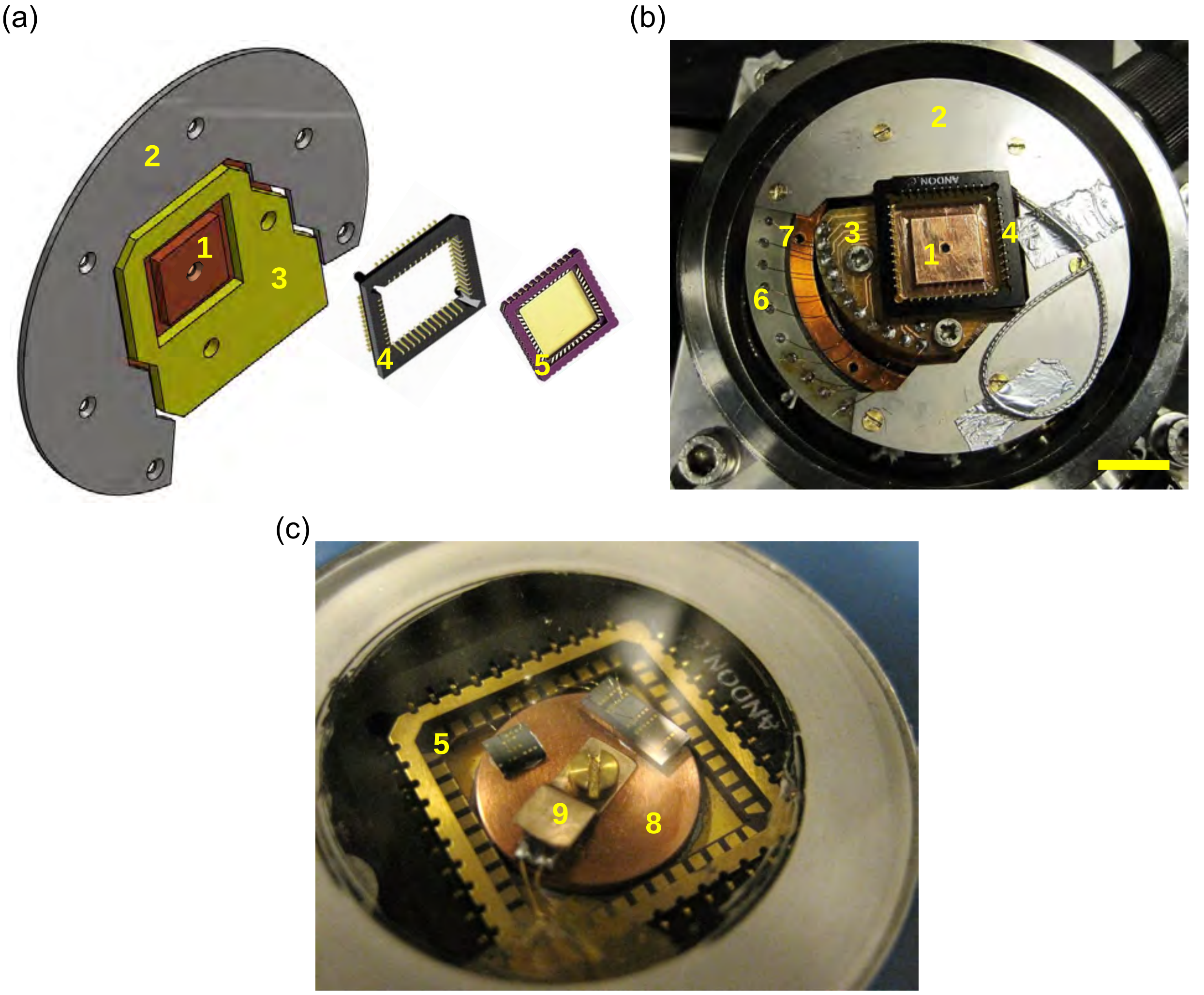

Figure B.1: Images of a custom-made holder for samples with electrical contacts. (a) Sketch of an assembly of the main sample holder parts: customized cold-finger (1), radiation shield (2), PCB (3), LCC socket (4) and a chip carrier (5). (b) Top view of the installation inside a liquid-helium flow cryostat chamber. A radiation shield (2) is modified to accommodate a customized PCB (3), which is connected to electrical feedthroughs inside the cryostat (6) via wires with high thermal resistivity (7). The PCB is tightened on a modified cold-finger piece (1). Finally, an LCC socket (4) is soldered onto the PCB. The yellow scale bar is around 1 cm. (c) Image of the removable sample holder, made of an LCC chip carrier (5) with a copper inset (8), and placed in the flow cryostat. The holder is inserted into the LCC socket and tightened to the cold-finger by a screw. Optionally, a copper clamp (9) can be used to secure the temperature sensor. The three images in (a) are the courtesy of Dennis W. Wistisen, Andon Electronics Corp., and Kyocera, respectively.

configuration, the temperature sensor is mounted somewhere below the sample holder in close proximity to the cold-finger, which reports a temperature that is generally different from the actual sample temperature. In the work reported in Chapter 5, the temperature has been measured by a sensor (Cernox RTD CX-1050-SD-HT-1.4L calibrated, Lake Shore Cryotronics, Inc.) mounted next to the sample on the copper inset. The sensor is clamped with a copper clamp (9) using the same screw that is used to fasten the LCC to the cold-finger.

Bibliography

[1] Z. I. Alferov, "The history and future of semiconductor heterostructures from the point of view of a Russian scientist", Phys. Scr. **T68**, 32–45 (1996).

[2] H. Kroemer, "Band offsets and chemical bonding: the basis for heterostructure applications", Phys. Scr. **T68**, 10–16 (1996).

[3] M. Nielsen and I. Chuang, *Quantum Computation and Quantum Information: 10th Anniversary Edition* (Cambridge University Press, 2010).

[4] E. Knill, R. Laflamme, and G. J. Milburn, "A scheme for efficient quantum computation with linear optics", Nature **409**, 46–52 (2001).

[5] N. Somaschi, V. Giesz, L. De Santis, J. C. Loredo, M. P. Almeida, G. Hornecker, S. L. Portalupi, T. Grange, C. Anton, J. Demory, C. Gomez, I. Sagnes, N. D. L. Kimura, A. Lemaitre, A. Auffeves, A. G. White, L. Lanco, and P. Senellart, "Near-optimal single-photon sources in the solid state", (2015), `arXiv:1510.06499`.

[6] P. Lodahl, S. Mahmoodian, and S. Stobbe, "Interfacing single photons and single quantum dots with photonic nanostructures", Rev. Mod. Phys. **87**, 347–400 (2015).

[7] S. John and T. Quang, "Spontaneous emission near the edge of a photonic band gap", Phys. Rev. A **50**, 1764–1769 (1994).

[8] R. Kaindl, M. A. Carnahan, D. Hägele, R. Lövenich, and D. S. Chemla, "Ultrafast terahertz probes of transient conducting and insulating phases in an electron-hole gas.", Nature **423**, 734–738 (2003).

[9] L. Butov, "Exciton condensation in coupled quantum wells", Solid State Commun. **127**, 89–98 (2003).

[10] T. Byrnes, N. Y. Kim, and Y. Yamamoto, "Exciton-polariton condensates", Nat. Phys. **10**, 803–813 (2014).

[11] N. F. Mott, "The transition to the metallic state", Philos. Mag. **6**, 287–309 (1961).

[12] A. J. Shields, "Semiconductor quantum light sources", Nat. Photonics **1**, 215–223 (2007).

[13] S. Mokkapati and C. Jagadish, "III-V compound SC for optoelectronic devices", Mater. Today **12**, 22–32 (2009).

[14] J. A. del Alamo, "Nanometre-scale electronics with III-V compound semiconductors", Nature **479**, 317–323 (2011).

[15] P. S. Zory, *Quantum Well Lasers* (Academic Press, Boston, MA, 1993), p. 505.

[16] X. Zhu, P. B. Littlewood, M. S. Hybertsen, and T. M. Rice, "Exciton Condensate in Semiconductor Quantum Well Structures", Phys. Rev. Lett. **74**, 1633–1636 (1995).

[17] A. A. High, E. E. Novitskaya, L. V. Butov, M. Hanson, and A. C. Gossard, "Control of Exciton Fluxes in an Excitonic Integrated Circuit", Science **321**, 229–231 (2008).

[18]G. Grosso, J. Graves, A. T. Hammack, A. A. High, L. V. Butov, M. Hanson, and A. C. Gossard, “Excitonic switches operating at around 100 K”, Nat. Photonics **3**, 577–580 (2009).

[19]P. Y. Yu and M. Cardona, *Fundamentals of Semiconductors*, Vol. 1, 11 (Springer Berlin Heidelberg, Berlin, Heidelberg, 2010), p. 793.

[20]G. H. Wannier, “The Structure of Electronic Excitation Levels in Insulating Crystals”, Phys. Rev. **52**, 191–197 (1937).

[21]P. T. Kristensen, “Light-matter interaction in nano-structures materials”, PhD thesis (Technical University of Denmark, 2009).

[22]D. M. Bruls, P. M. Koenraad, H. W. M. Salemink, J. H. Wolter, M. Hopkinson, and M. S. Skolnick, “Stacked low-growth-rate InAs quantum dots studied at the atomic level by cross-sectional scanning tunneling microscopy”, Appl. Phys. Lett. **82**, 3758 (2003).

[23]M. Bayer, G. Ortner, O. Stern, A. Kuther, A. A. Gorbunov, A. Forchel, P. Hawrylak, S. Fafard, K. Hinzer, T. L. Reinecke, S. N. Walck, J. P. Reithmaier, F. Klopf, and F. Schäfer, “Fine structure of neutral and charged excitons in self-assembled In(Ga)As/(Al)GaAs quantum dots”, Phys. Rev. B **65**, 195315 (2002).

[24]Q. Wang, S. Stobbe, and P. Lodahl, “Mapping the Local Density of Optical States of a Photonic Crystal with Single Quantum Dots”, Phys. Rev. Lett. **107**, 167404 (2011).

[25]J. Johansen, B. Julsgaard, S. Stobbe, J. M. Hvam, and P. Lodahl, “Probing long-lived dark excitons in self-assembled quantum dots”, Phys. Rev. B **81**, 081304 (2010).

[26]L. Novotny and B. Hecht, *Principles of Nano-Optics*, Second (Cambridge University Press, 2012), p. 564.

[27]V. P. Bykov, “Spontaneous emission from a medium with a band spectrum”, Sov. J. Quantum Electron. **4**, 861–871 (1975).

[28]E. Yablonovitch, “Inhibited Spontaneous Emission in Solid-State Physics and Electronics”, Phys. Rev. Lett. **58**, 2059–2062 (1987).

[29]S. John, “Strong localization of photons in certain disordered dielectric superlattices”, Phys. Rev. Lett. **58**, 2486–2489 (1987).

[30]J. Joannopoulos, S. Johnson, J. Winn, and R. Meade, *Photonic Crystals: Molding the Flow of Light* (Princeton University Press, 2011), p. 304.

[31]M. Arcari, I. Söllner, A. Javadi, S. Lindskov Hansen, S. Mahmoodian, J. Liu, H. Thyrrestrup, E. H. Lee, J. D. Song, S. Stobbe, and P. Lodahl, “Near-Unity Coupling Efficiency of a Quantum Emitter to a Photonic Crystal Waveguide”, Phys. Rev. Lett. **113**, 093603 (2014).

[32]Y. Vlasov, M. O’Boyle, H. F. Hamann, and S. J. McNab, “Active control of slow light on a chip with photonic crystal waveguides”, Nature **438**, 65–69 (2005).

[33]J. H. Davies, *The Physics of Low-dimensional Semiconductors: An Introduction* (Cambridge University Press, 1998), p. 438.

[34]D. A. B. Miller, D. S. Chemla, T. C. Damen, A. C. Gossard, W. Wiegmann, T. H. Wood, and C. A. Burrus, “Electric field dependence of optical absorption near the band gap of quantum-well structures”, Phys. Rev. B **32**, 1043–1060 (1985).

[35]P. W. Fry, I. E. Itskevich, D. J. Mowbray, M. S. Skolnick, J. J. Finley, J. A. Barker, E. P. O’Reilly, L. R. Wilson, I. A. Larkin, P. A. Maksym, M. Hopkinson, M. Al-Khafaji, J. P. R. David, A. G. Cullis, G. Hill, and J. C. Clark, “Inverted Electron-Hole Alignment in InAs-GaAs Self-Assembled Quantum Dots”, Phys. Rev. Lett. **84**, 733–736 (2000).

[36] T. F. Krauss, R. M. D. L. Rue, and S. Brand, "Two-dimensional photonic-bandgap structures operating at near-infrared wavelengths", Nature **383**, 699–702 (1996).

[37] O. Painter, "Two-Dimensional Photonic Band-Gap Defect Mode Laser", Science **284**, 1819–1821 (1999).

[38] K. Takeda, T. Sato, A. Shinya, K. Nozaki, W. Kobayashi, H. Taniyama, M. Notomi, K. Hasebe, T. Kakitsuka, and S. Matsuo, "Few-fJ/bit data transmissions using directly modulated lambda-scale embedded active region photonic-crystal lasers", Nat. Photonics **7**, 569–575 (2013).

[39] I. P. González, L. E. Muñoz Camuñez, A. G. Taboada, C. Robles Urdiales, J. M. Ripalda Cobián, and P. A. Postigo Resa, "Fabrication of high quality factor GaAs/InAsSb photonic crystal microcavities by inductively coupled plasma etching and fast wet etching", J. Vac. Sci. Technol. B Microelectron. Nanom. Struct. **32**, 011204 (2014).

[40] J. P. Sprengers, A. Gaggero, D. Sahin, S. Jahanmirinejad, G. Frucci, F. Mattioli, R. Leoni, J. Beetz, M. Lermer, M. Kamp, S. Höfling, R. Sanjines, and A. Fiore, "Waveguide superconducting single-photon detectors for integrated quantum photonic circuits", Appl. Phys. Lett. **99**, 181110 (2011).

[41] L. Midolo, T. Pregnolato, G. Kiršanskė, and S. Stobbe, "Soft-mask fabrication of gallium arsenide nanomembranes for integrated quantum photonics", Nanotechnology **26**, 484002 (2015).

[42] B. Ellis, M. A. Mayer, G. Shambat, T. Sarmiento, J. Harris, E. E. Haller, and J. Vučković, "Ultralow-threshold electrically pumped quantum-dot photonic-crystal nanocavity laser", Nat. Photonics **5**, 297–300 (2011).

[43] S. M. Thon, H. Kim, C. Bonato, J. Gudat, J. Hagemeier, P. M. Petroff, and D. Bouwmeester, "Independent electrical tuning of separated quantum dots in coupled photonic crystal cavities", Appl. Phys. Lett. **99**, 161102 (2011).

[44] S. G. Carter, T. M. Sweeney, M. Kim, C. S. Kim, D. Solenov, S. E. Economou, T. L. Reinecke, L. Yang, A. S. Bracker, and D. Gammon, "Quantum control of a spin qubit coupled to a photonic crystal cavity", Nat. Photonics **7**, 329–334 (2013).

[45] D. R. S. Cumming, S. Thoms, S. P. Beaumont, and J. M. R. Weaver, "Fabrication of 3 nm wires using 100 keV electron beam lithography and poly(methyl methacrylate) resist", Appl. Phys. Lett. **68**, 322 (1996).

[46] A. G. Baca and C. I. H. Ashby, *Fabrication of GaAs Devices* (Institution of Engineering and Technology, London, 2005).

[47] K. A. Atlasov, P. Gallo, A. Rudra, B. Dwir, and E. Kapon, "Effect of sidewall passivation in BCl_3/N_2 inductively coupled plasma etching of two-dimensional GaAs photonic crystals", J. Vac. Sci. Technol. B Microelectron. Nanom. Struct. **27**, L21 (2009).

[48] K. Hennessy, A. Badolato, P. Petroff, and E. Hu, "Positioning photonic crystal cavities to single InAs quantum dots", Photonic. Nanostruct. 2, 65–72 (2004).

[49] E. Yablonovitch, T. Gmitter, J. P. Harbison, and R. Bhat, "Extreme selectivity in the lift-off of epitaxial GaAs films", Appl. Phys. Lett. **51** (1987).

[50] M. M. A. J. Voncken, J. J. Schermer, A. T. J. van Niftrik, G. J. Bauhuis, P. Mulder, P. K. Larsen, T. P. J. Peters, B. de Bruin, A. Klaassen, and J. J. Kelly, "Etching AlAs with HF for Epitaxial Lift-Off Applications", J. Electrochem. Soc. **151**, G347 (2004).

[51]J. Sweet, B. C. Richards, J. D. Olitzky, J. Hendrickson, G. Khitrova, H. M. Gibbs, D. Litvinov, D. Gerthsen, D. Z. Hu, D. M. Schaadt, M. Wegener, U. Khankhoje, and A. Scherer, “GaAs photonic crystal slab nanocavities: Growth, fabrication, and quality factor”, Photonic. Nanostruct. **8**, 1–6 (2010).

[52]G. C. DeSalvo, “Wet Chemical Digital Etching of GaAs at Room Temperature”, J. Electrochem. Soc. **143**, 3652 (1996).

[53]R. Maboudian, “Critical Review: Adhesion in surface micromechanical structures”, J. Vac. Sci. Technol. B Microelectron. Nanom. Struct. **15**, 1 (1997).

[54]M. Scheibner, M. Yakes, A. S. Bracker, I. V. Ponomarev, M. F. Doty, C. S. Hellberg, L. J. Whitman, T. L. Reinecke, and D. Gammon, “Optically mapping the electronic structure of coupled quantum dots”, Nat. Phys. **4**, 291–295 (2008).

[55]T. C. Shen, G. B. Gao, and H. Morkoç, “Recent developments in ohmic contacts for III-V compound semiconductors”, J. Vac. Sci. Technol. B **10** (1992).

[56]A. G. Baca, F. Ren, J. C. Zolper, R. D. Briggs, and S. J. Pearton, “A survey of ohmic contacts to III-V compound semiconductors”, Thin Solid Films **308-309**, 599–606 (1997).

[57]N. Braslau, J. B. Gunn, and J. L. Staples, “Metal-semiconductor contacts for GaAs bulk effect devices”, Solid. State. Electron. **10**, 381–383 (1967).

[58]I. Shtrichman, C. Metzner, B. D. Gerardot, W. V. Schoenfeld, and P. M. Petroff, “Photoluminescence of a single InAs quantum dot molecule under applied electric field”, Phys. Rev. B **65**, 081303 (2002).

[59]H. Kim, S. M. Thon, P. M. Petroff, and D. Bouwmeester, “Independent tuning of quantum dots in a photonic crystal cavity”, Appl. Phys. Lett. **95**, 243107 (2009).

[60]J. D. Mar, X. L. Xu, J. J. Baumberg, A. C. Irvine, C. Stanley, and D. A. Williams, “Electrically tunable hole tunnelling from a single self-assembled quantum dot embedded in an n-i-Schottky photovoltaic cell”, Appl. Phys. Lett. **99**, 031102 (2011).

[61]M. Stern, V. Umansky, and I. Bar-Joseph, “Exciton Liquid in Coupled Quantum Wells”, Science **343**, 55–57 (2014).

[62]G. Stareev, “Formation of extremely low resistance Ti/Pt/Au ohmic contacts to p-GaAs”, Appl. Phys. Lett. **62**, 2801 (1993).

[63]V. Adivarahan, A. Lunev, M. A. Khan, J. Yang, G. Simin, M. S. Shur, and R. Gaska, “Very-low-specific-resistance Pd/Ag/Au/Ti/Au alloyed ohmic contact to p GaN for high-current devices”, Appl. Phys. Lett. **78**, 2781 (2001).

[64]C.-H. Wu, S.-M. Liao, and K.-C. Chang, “Ni/Pd/Au ohmic contact for p-GaAs and its application in red RCLED”, Mater. Sci. Eng. B **117**, 205–209 (2005).

[65]T. Sanada and O. Wada, “Ohmic Contacts to p-GaAs with Au/Zn/Au Structure”, Jpn. J. Appl. Phys. **19**, L491–L494 (1980).

[66]D. E. Kren, A. A. Rezazadeh, and P. K. Rees, “Low ohmic contacts to C-doped p-GaAs with Au/Zn/Au structure”, Electron. Lett. **28**, 1248 (1992).

[67]A. Boronat, S. Silvestre, and A. Orpella, “Ohmic contacts fabricated on moderately doped p-type GaAs by sputtering deposition and a laser-firing process”, J. Vac. Sci. Technol. B Microelectron. Nanom. Struct. **31**, 051209 (2013).

[68]D. J. P. Ellis, A. J. Bennett, A. J. Shields, P. Atkinson, and D. A. Ritchie, “Electrically addressing a single self-assembled quantum dot”, Appl. Phys. Lett. **88**, 133509 (2006).

[69] G. Mariani, A. C. Scofield, C.-H. Hung, and D. L. Huffaker, “GaAs nanopillar-array solar cells employing in situ surface passivation”, Nat. Commun. **4**, 1497 (2013).

[70] Y.-C. Shih, M. Murakami, E. L. Wilkie, and A. C. Callegari, “Effects of interfacial microstructure on uniformity and thermal stability of AuNiGe ohmic contact to n-type GaAs”, J. Appl. Phys. **62**, 582 (1987).

[71] Y. Huang, J. Luo, and D. G. Ivey, “Comparative study of GaAs corrosion in H_2SO_4 and $NH_3{\cdot}H_2O$ solutions by electrochemical methods and surface analysis”, Mater. Chem. Phys. **93**, 429–442 (2005).

[72] A. Faraon, A. Majumdar, D. Englund, E. Kim, M. Bajcsy, and J. Vučković, “Integrated quantum optical networks based on quantum dots and photonic crystals”, New J. Phys. **13**, 055025 (2011).

[73] C. Bentham, I. E. Itskevich, R. J. Coles, B. Royall, E. Clarke, J. O’Hara, N. Prtljaga, A. M. Fox, M. S. Skolnick, and L. R. Wilson, “On-chip electrically controlled routing of photons from a single quantum dot”, Appl. Phys. Lett. **106**, 221101 (2015).

[74] L. H. Frandsen, A. Harpøth, P. I. Borel, M Kristensen, J. S. Jensen, and O. Sigmund, “Broadband photonic crystal waveguide 60° bend obtained utilizing topology optimization”, Opt. Express **12**, 5916 (2004).

[75] M. Ayre, T. J. Karle, Lijun Wu, T. Davies, and T. F. Krauss, “Experimental verification of numerically optimized photonic crystal injector, Y-splitter, and bend”, IEEE J. Sel. Areas Commun. **23**, 1390–1395 (2005).

[76] Y. Taguchi, Y. Takahashi, Y. Sato, T. Asano, and S. Noda, “Statistical studies of photonic heterostructure nanocavities with an average Q factor of three million”, Opt. Express **19**, 11916 (2011).

[77] P. W. Anderson, “Absence of Diffusion in Certain Random Lattices”, Phys. Rev. **109**, 1492–1505 (1958).

[78] L. Sapienza, H. Thyrrestrup, S. Stobbe, P. D. Garcia, S. Smolka, and P. Lodahl, “Cavity Quantum Electrodynamics with Anderson-Localized Modes”, Science **327**, 1352–1355 (2010).

[79] J. D. Joannopoulos, R. D. Meade, and J. N. Winn, *Photonic Crystals: Molding the Flow of Light* (Princeton University Press, Princeton, Oxford, 1995).

[80] N. Le Thomas, Z. Diao, H. Zhang, and R. Houdré, “Statistical analysis of subnanometer residual disorder in photonic crystal waveguides: Correlation between slow light properties and structural properties”, J. Vac. Sci. Technol. B Microelectron. Nanom. Struct. **29**, 051601 (2011).

[81] H. Thyrrestrup, S. Smolka, L. Sapienza, and P. Lodahl, “Statistical Theory of a Quantum Emitter Strongly Coupled to Anderson-Localized Modes”, Phys. Rev. Lett. **108**, 113901 (2012).

[82] S. R. Huisman, G. Ctistis, S. Stobbe, A. P. Mosk, J. L. Herek, A. Lagendijk, P. Lodahl, W. L. Vos, and P. W. H. Pinkse, “Measurement of a band-edge tail in the density of states of a photonic-crystal waveguide”, Phys. Rev. B **86**, 155154 (2012).

[83] P. D. García, A. Javadi, H. Thyrrestrup, and P. Lodahl, “Quantifying the intrinsic amount of fabrication disorder in photonic-crystal waveguides from optical far-field intensity measurements”, Appl. Phys. Lett. **102**, 031101 (2013).

[84] A. Javadi, I. Söllner, M. Arcari, S. Lindskov Hansen, L. Midolo, S. Mahmoodian, G. Kiršanskė, T. Pregnolato, E. H. Lee, J. D. Song, S. Stobbe, and P. Lodahl, “Single-photon non-linear optics with a quantum dot in a waveguide”, Nat. Commun. **6**, 8655 (2015).

[85] L.-M. Duan and H. J. Kimble, “Scalable Photonic Quantum Computation through Cavity-Assisted Interactions”, Phys. Rev. Lett. **92**, 127902 (2004).

[86] H. Zheng, D. J. Gauthier, and H. U. Baranger, “Waveguide-QED-Based Photonic Quantum Computation”, Phys. Rev. Lett. **111**, 090502 (2013).

[87] D. E. Chang, A. S. Sørensen, E. A. Demler, and M. D. Lukin, “A single-photon transistor using nanoscale surface plasmons”, Nat. Phys. **3**, 807–812 (2007).

[88] D. Witthaut, M. D. Lukin, and A. S. Sørensen, “Photon sorters and QND detectors using single photon emitters”, Europhys. Lett. **97**, 50007 (2012).

[89] I. Söllner, S. Mahmoodian, S. L. Hansen, L. Midolo, A. Javadi, G. Kiršanskė, T. Pregnolato, H. El-Ella, E. H. Lee, J. D. Song, S. Stobbe, and P. Lodahl, “Deterministic photon-emitter coupling in chiral photonic circuits”, Nat. Nanotechnol. **10**, 775–778 (2015).

[90] A. J. Bennett, M. A. Pooley, R. M. Stevenson, M. B. Ward, R. B. Patel, A. B. de la Giroday, N. Sköld, I. Farrer, C. A. Nicoll, D. A. Ritchie, and A. J. Shields, “Electric-field-induced coherent coupling of the exciton states in a single quantum dot”, Nat. Phys. **6**, 947–950 (2010).

[91] O. Benson, C. Santori, M. Pelton, and Y. Yamamoto, “Regulated and Entangled Photons from a Single Quantum Dot”, Phys. Rev. Lett. **84**, 2513–2516 (2000).

[92] R. J. Warburton, C. Schäflein, D. Haft, F. Bickel, A. Lorke, K. Karrai, J. M. Garcia, W. Schoenfeld, and P. M. Petroff, “Optical emission from a charge-tunable quantum ring”, Nature **405**, 926–929 (2000).

[93] R. J. Warburton, “Single spins in self-assembled quantum dots”, Nat. Mater. **12**, 483–493 (2013).

[94] S. John and J. Wang, “Quantum electrodynamics near a photonic band gap: Photon bound states and dressed atoms”, Phys. Rev. Lett. **64**, 2418–2421 (1990).

[95] I. M. Lifshitz, “The energy spectrum of disordered systems”, Adv. Phys. **13**, 483–536 (1964).

[96] V. Savona, “Electromagnetic modes of a disordered photonic crystal”, Phys. Rev. B **83**, 085301 (2011).

[97] P. Sheng, *Introduction to Wave Scattering, Localization and Mesoscopic Phenomena* (Springer, Berlin, Heidelberg, 2006).

[98] A. Baron, S. Mazoyer, W. Smigaj, and P. Lalanne, “Attenuation Coefficient of Single-Mode Periodic Waveguides”, Phys. Rev. Lett. **107**, 153901 (2011).

[99] S. Smolka, H. Thyrrestrup, L. Sapienza, T. B. Lehmann, K. R. Rix, L. S. Froufe-Pérez, P. D. García, and P. Lodahl, “Probing the statistical properties of Anderson localization with quantum emitters”, New J. Phys. **13**, 063044 (2011).

[100] A. J. Bennett, R. B. Patel, J. Skiba-Szymanska, C. A. Nicoll, I. Farrer, D. A. Ritchie, and A. . Shields, “Giant Stark effect in the emission of single semiconductor quantum dots”, Appl. Phys. Lett. **97**, 031104 (2010).

[101] A. Faraon, I. Fushman, D. Englund, N. Stoltz, P. Petroff, and J. Vučković, “Coherent generation of non-classical light on a chip via photon-induced tunnelling and blockade”, Nat. Phys. **4**, 859–863 (2008).

[102] P. W. Fry, I. E. Itskevich, D. J. Mowbray, M. S. Skolnick, J. J. Finley, J. A. Barker, E. P. O’Reilly, L. R. Wilson, I. A. Larkin, P. A. Maksym, M. Hopkinson, M. Al-Khafaji, J. P. R. David, A. G. Cullis, G. Hill, and J. C. Clark, “Inverted Electron-Hole Alignment in InAs-GaAs Self-Assembled Quantum Dots”, Phys. Rev. Lett. **84**, 733–736 (2000).

[103] J. A. Barker and E. P. O'Reilly, "Theoretical analysis of electro-hole alignment in InAs-GaAs quantum dots", Phys. Rev. B **61**, 13840–13851 (2000).

[104] J. J. Finley, M Sabathil, P Vogl, G. Abstreiter, R Oulton, A. I. Tartakovskii, D. J. Mowbray, M. S. Skolnick, S. L. Liew, A. G. Cullis, and M Hopkinson, "Quantum-confined Stark shifts of charged exciton complexes in quantum dots", Phys. Rev. B **70**, 201308 (2004).

[105] J. Johansen, S. Stobbe, I. S. Nikolaev, T. Lund-Hansen, P. T. Kristensen, J. M. Hvam, W. L. Vos, and P. Lodahl, "Size dependence of the wavefunction of self-assembled InAs quantum dots from time-resolved optical measurements", Phys. Rev. B **77**, 073303 (2008).

[106] 1D Poisson-Schrödinger solver, developed by Gregory Snider, University of Notre Dame, IN, USA, 1998, [www.nd.edu].

[107] R. Faggiani, A. Baron, X. Zang, L. Lalouat, S. A. Schulz, K. Vynck, B. O'Regan, B. Cluzel, F. de Fornel, T. F. Krauss, and P. Lalanne, "Ultimate limits of light confinement in randomly-perturbed periodic structures", (2015), arXiv:1505.03472.

[108] J. Topolancik, B. Ilic, and F. Vollmer, "Experimental Observation of Strong Photon Localization in Disordered Photonic Crystal Waveguides", Phys. Rev. Lett. **99**, 253901 (2007).

[109] P. D. García, S. Stobbe, I. Söllner, and P. Lodahl, "Nonuniversal Intensity Correlations in a Two-Dimensional Anderson-Localizing Random Medium", Phys. Rev. Lett. **109**, 253902 (2012).

[110] M. L. Povinelli, S. G. Johnson, E. Lidorikis, J. D. Joannopoulos, and M. Soljačić, "Effect of a photonic band gap on scattering from waveguide disorder", Appl. Phys. Lett. **84**, 3639 (2004).

[111] S. Mazoyer, J. P. Hugonin, and P. Lalanne, "Disorder-Induced Multiple Scattering in Photonic-Crystal Waveguides", Phys. Rev. Lett. **103**, 063903 (2009).

[112] P. D. García, S. Smolka, S. Stobbe, and P. Lodahl, "Density of states controls Anderson localization in disordered photonic crystal waveguides", Phys. Rev. B **82**, 165103 (2010).

[113] P. D. García, A. Javadi, and P. Lodahl, "Interplay between effective mass and group velocity in the formation of Anderson-localized modes in photonic-crystal waveguides", (Unpublished).

[114] T. Baba, "Slow light in photonic crystals", Nat. Photonics **2**, 465–473 (2008).

[115] M. Charbonneau-Lefort, E. Istrate, M. Allard, J. Poon, and E. H. Sargent, "Photonic crystal heterostructures: Waveguiding phenomena and methods of solution in an envelope function picture", Phys. Rev. B **65**, 125318 (2002).

[116] J. Liu, P. D. García, S. Ek, N. Gregersen, T. Suhr, M. Schubert, J. Mørk, S. Stobbe, and P. Lodahl, "Random nanolasing in the Anderson localized regime", Nat. Nanotechnol. **9**, 285–289 (2014).

[117] S. Seidl, M. Kroner, A. Högele, K. Karrai, R. J. Warburton, A. Badolato, and P. M. Petroff, "Effect of uniaxial stress on excitons in a self-assembled quantum dot", Appl. Phys. Lett. **88**, 203113 (2006).

[118] J. D. Plumhof, V. Křápek, F. Ding, K. D. Jöns, R. Hafenbrak, P. Klenovský, A. Herklotz, K. Dörr, P. Michler, A. Rastelli, and O. G. Schmidt, "Strain-induced anticrossing of bright exciton levels in single self-assembled GaAs/$Al_xGa_{1-x}As$ and $In_xGa_{1-x}As$/GaAs quantum dots", Phys. Rev. B **83**, 121302 (2011).

[119] S. Malik, C. Roberts, R. Murray, and M. Pate, "Tuning self-assembled InAs quantum dots by rapid thermal annealing", Appl. Phys. Lett. **71**, 1987 (1997).

[120] W. Heller, U. Bockelmann, and G. Abstreiter, "Electric-field effects on excitons in quantum dots", Phys. Rev. B **57**, 6270–6273 (1998).

[121] S. Marcet, K. Ohtani, and H. Ohno, “Vertical electric field tuning of the exciton fine structure splitting and photon correlation measurements of GaAs quantum dot”, Appl. Phys. Lett. **96**, 101117 (2010).

[122] T. M. Stace, G. J. Milburn, and C. H. W. Barnes, “Entangled two-photon source using biexciton emission of an asymmetric quantum dot in a cavity”, Phys. Rev. B **67**, 085317 (2003).

[123] T. Yoshie, A. Scherer, J. Hendrickson, G. Khitrova, H. M. Gibbs, G. Rupper, C. Ell, O. B. Shchekin, and D. G. Deppe, “Vacuum Rabi splitting with a single quantum dot in a photonic crystal nanocavity”, Nature **432**, 200–203 (2004).

[124] J. P. Reithmaier, G. Sęk, A Löffler, C Hofmann, S Kuhn, S Reitzenstein, L. V. Keldysh, V. D. Kulakovskii, T. L. Reinecke, and A Forchel, “Strong coupling in a single quantum dot-semiconductor microcavity system”, Nature **432**, 197–200 (2004).

[125] R. Trotta, J. S. Wildmann, E. Zallo, O. G. Schmidt, and A. Rastelli, “Highly Entangled Photons from Hybrid Piezoelectric-Semiconductor Quantum Dot Devices”, Nano Lett. **14**, 3439–3444 (2014).

[126] J. Zhang, J. S. Wildmann, F. Ding, R. Trotta, and Y. Huo, “Strain-tunable entangled-light-emitting diodes with high yield and fast operation speed”, `arXiv:1505.03026`.

[127] Y. Chen, J. Zhang, M. Zopf, K. Jung, Y. Zhang, F. Ding, and O. G. Schmidt, “Energy-tunable entangled photon sources on a III-V/Silicon chip”, (2015), `arXiv:1508.00042`.

[128] J Beetz, T Braun, C Schneider, S Höfling, and M Kamp, “Anisotropic strain-tuning of quantum dots inside a photonic crystal cavity”, Semicond. Sci. Technol. **28**, 122002 (2013).

[129] K. D. Jöns, R. Hafenbrak, R. Singh, F. Ding, J. D. Plumhof, A. Rastelli, O. G. Schmidt, G. Bester, and P. Michler, “Dependence of the Redshifted and Blueshifted Photoluminescence Spectra of Single In_xGa_{1-x} As/GaAs Quantum Dots on the Applied Uniaxial Stress”, Phys. Rev. Lett. **107**, 217402 (2011).

[130] Y. Sun, S. E. Thompson, and T. Nishida, *Strain effect in semiconductors: Theory and device application*, First (Springer US, New York, 2010), p. 350.

[131] J. Hirth and J. Lothe, *Theory of Dislocations* (Wiley, New York, 1982), p. 857.

[132] G. L. Pikus and G. E. Bir, *Symmetry and strain-induced effects in semiconductors* (Wiley, New York, 1974), p. 484.

[133] S.-E. Park and T. R. Shrout, “Ultrahigh strain and piezoelectric behavior in relaxor based ferroelectric single crystals”, J. Appl. Phys. **82**, 1804 (1997).

[134] A. Herklotz, J. D. Plumhof, A. Rastelli, O. G. Schmidt, L. Schultz, and K. Dörr, “Electrical characterization of PMN–28%PT(001) crystals used as thin-film substrates”, J. Appl. Phys. **108**, 094101 (2010).

[135] S. Nomura and K. Uchino, “Electrostrictive effect in $Pb(Mg_{1/3}Nb_{2/3})O_3$-type materials”, Ferroelectrics **41**, 117–132 (1982).

[136] R. Trotta, P. Atkinson, J. D. Plumhof, E. Zallo, R. O. Rezaev, S. Kumar, S. Baunack, J. R. Schröter, A. Rastelli, and O. G. Schmidt, “Nanomembrane Quantum-Light-Emitting Diodes Integrated onto Piezoelectric Actuators”, Adv. Mater. **24**, 2668–2672 (2012).

[137] M. Levinshtein, S. Rumyantsev, and M. Shur, *Handbook Series on Semiconductor Parameters*, 2nd ed. (World Scientific, London, 1996), p. 452.

[138] S Rodt, R Heitz, A Schliwa, R. L. Sellin, F Guffarth, and D Bimberg, “Repulsive exciton-exciton interaction in quantum dots”, Phys. Rev. B **68**, 035331 (2003).

[139] K. Alam, “Uniaxial Stress-Modulated Electronic Properties of a Free-Standing InAs Nanowire”, IEEE Trans. Electron Devices **59**, 661–665 (2012).

[140] J. R. Jain, A. Hryciw, T. M. Baer, D. A. B. Miller, M. L. Brongersma, and R. T. Howe, “A micromachining-based technology for enhancing germanium light emission via tensile strain”, Nat. Photonics **6**, 398–405 (2012).

[141] M. J. Süess, R. Geiger, R. A. Minamisawa, G. Schiefler, J. Frigerio, D. Chrastina, G. Isella, R. Spolenak, J. Faist, and H. Sigg, “Analysis of enhanced light emission from highly strained germanium microbridges”, Nat. Photonics **7**, 466–472 (2013).

[142] R. A. Minamisawa, M. J. Süess, R Spolenak, J Faist, C David, J Gobrecht, K. K. Bourdelle, and H Sigg, “Top-down fabricated silicon nanowires under tensile elastic strain up to 4.5%”, Nat. Commun. **3**, 1096 (2012).

[143] N. F. Mott, “The basis of the electron theory of metals, with special reference to the transition metals”, Proc. Phys. Soc. Sect. A **62**, 416–422 (1949).

[144] J. Neuenschwander and P. Wachter, “Pressure-driven semiconductor-metal transition in intermediate-valence $TmSe_{1-x}Te_x$ and the concept of an excitonic insulator”, Phys. Rev. B **41**, 12693–12709 (1990).

[145] A. Zylbersztejn and N. F. Mott, “Metal-insulator transition in vanadium dioxide”, Phys. Rev. B **11**, 4383–4395 (1975).

[146] A. Chernikov, C. Ruppert, H. M. Hill, A. F. Rigosi, and T. F. Heinz, “Population inversion and giant bandgap renormalization in atomically thin WS2 layers”, Nat. Photonics **9**, 466–470 (2015).

[147] M. R. Oliver, J. A. Kafalas, J. O. Dimmock, and T. B. Reed, “Pressure Dependence of the Electrical Resistivity of EuO”, Phys. Rev. Lett. **24**, 1064–1067 (1970).

[148] W. Sasaki, “The Metal-non Metal Transition in Doped Semiconductors”, Le J. Phys. Colloq. **37**, C4–307–C4–311 (1976).

[149] P. Limelette, P. Wzietek, S. Florens, A. Georges, T. A. Costi, C. Pasquier, D. Jérome, C. Mézière, and P. Batail, “Mott Transition and Transport Crossovers in the Organic Compound κ-(BEDT-TTF)$_2$Cu[N(CN)$_2$]Cl”, Phys. Rev. Lett. **91**, 016401 (2003).

[150] M. Greiner, O. Mandel, T. Esslinger, T. W. Hänsch, and I. Bloch, “Quantum phase transition from a superfluid to a Mott insulator in a gas of ultracold atoms”, Nature **415**, 39–44 (2002).

[151] N. Poccia, T. I. Baturina, F. Coneri, C. G. Molenaar, X. R. Wang, G. Bianconi, A. Brinkman, H. Hilgenkamp, A. A. Golubov, and V. M. Vinokur, “Critical behavior at a dynamic vortex insulator-to-metal transition”, Science **349**, 1202–1205 (2015).

[152] R. Huber, R. Kaindl, B. Schmid, and D. Chemla, “Broadband terahertz study of excitonic resonances in the high-density regime in GaAs/AlGaAs quantum wells”, Phys. Rev. B **72**, 161314 (2005).

[153] L. Kappei, J. Szczytko, F. Morier-Genoud, and B. Deveaud, “Direct observation of the Mott transition in an optically excited semiconductor quantum well.”, Phys. Rev. Lett. **94**, 147403 (2005).

[154] M. Stern, V. Garmider, V. Umansky, and I. Bar-Joseph, “Mott transition of excitons in coupled quantum wells”, Phys. Rev. Lett. **100**, 256402 (2008).

[155] S. Ben-Tabou de Leon and B. Laikhtman, “Mott transition, biexciton crossover, and spin ordering in the exciton gas in quantum wells”, Phys. Rev. B **67**, 235315 (2003).

[156] V. Nikolaev and M. Portnoi, “Theory of the excitonic Mott transition in quasi-two-dimensional systems”, Superlattices Microstruct. **43**, 460–464 (2008).

[157] Y. E. Lozovik and O. L. Berman, “Phase transitions in a system of two coupled quantum wells”, J. Exp. Theor. Phys. Lett. **64**, 573–579 (1996).

[158] S. W. Koch, W. Hoyer, M. Kira, and V. S. Filinov, “Exciton ionization in semiconductors”, Phys. Status Solidi C **238**, 404–410 (2003).

[159] G. Manzke, D. Semkat, and H. Stolz, “Mott transition of excitons in GaAs-GaAlAs quantum wells”, New J. Phys. **14**, 095002 (2012).

[160] Y. J. Chen, E. S. Koteles, B. S. Elman, and C. A. Armiento, “Effect of electric fields on excitons in a coupled double-quantum-well structure”, Phys. Rev. B **36**, 4562–4565 (1987).

[161] D. Fisher and P. Hohenberg, “Dilute Bose gas in two dimensions”, Phys. Rev. B **37**, 4936–4943 (1988).

[162] M. Hagn, A. Zrenner, G. Böhm, and G. Weimann, “Electric-field-induced exciton transport in coupled quantum well structures”, Appl. Phys. Lett. **67**, 232 (1995).

[163] J. H. Kim, T. W. Kim, and K. H. Yoo, “Interband Stark effects in $\mathrm{In}_x\mathrm{Ga}_{1-x}\mathrm{As}/\mathrm{In}_y\mathrm{Al}_{1-y}\mathrm{As}$ coupled step quantum wells”, Appl. Surf. Sci. **240**, 452–455 (2005).

[164] M. Remeika, M. M. Fogler, L. V. Butov, M. Hanson, and A. C. Gossard, “Two-dimensional electrostatic lattices for indirect excitons”, Appl. Phys. Lett. **100**, 061103 (2012).

[165] A. G. Winbow, J. R. Leonard, M. Remeika, Y. Y. Kuznetsova, A. A. High, A. T. Hammack, L. V. Butov, J. Wilkes, A. A. Guenther, A. L. Ivanov, M. Hanson, and A. C. Gossard, “Electrostatic conveyer for excitons”, Phys. Rev. Lett. **106**, 196806 (2011).

[166] L. V. Butov and A. Filin, “Anomalous transport and luminescence of indirect excitons in AlAs/GaAs coupled quantum wells as evidence for exciton condensation”, Phys. Rev. B **58**, 1980–2000 (1998).

[167] L. V. Butov, A. Zrenner, G. Abstreiter, G. Böhm, and G. Weimann, “Condensation of Indirect Excitons in Coupled AlAs/GaAs Quantum Wells”, Phys. Rev. Lett. **73**, 304–307 (1994).

[168] A. V. Larionov, V. B. Timofeev, P. A. Ni, S. V. Dubonos, I. Hvam, and K. Soerensen, “Bose condensation of interwell excitons in double quantum wells”, J. Exp. Theor. Phys. Lett. **75**, 570–574 (2002).

[169] L. V. Butov, C. W. Lai, A. L. Ivanov, A. C. Gossard, and D. S. Chemla, “Towards Bose-Einstein condensation of excitons in potential traps.”, Nature **417**, 47–52 (2002).

[170] G. Christmann, A. Askitopoulos, G. Deligeorgis, Z. Hatzopoulos, S. I. Tsintzos, P. G. Savvidis, and J. J. Baumberg, “Oriented polaritons in strongly-coupled asymmetric double quantum well microcavities”, Appl. Phys. Lett. **98**, 081111 (2011).

[171] M. S. C. Luo, P. C. M. Planken, I. Brener, H. G. Roskos, and M. C. Nuss, “Generation of terahertz electromagnetic pulses from quantum-well structures”, IEEE J. Quantum Electron. **30**, 1478–1488 (1994).

[172] R. S. Daveau, P. Tighineanu, P. Lodahl, and S. Stobbe, “Optical refrigeration with coupled quantum wells”, Opt. Express **23**, 25340 (2015).

[173] G. K. G. Burau, G. Manzke, F. Kieseling, H. Stolz, D. Reuter, and A. Wieck, “Nonlinear behaviour of the resonance fluorescence from excitons in quantum wells”, J. Phys. Conf. Ser. **210**, 012017 (2010).

[174] I. Vurgaftman, J. R. Meyer, and L. R. Ram-Mohan, "Band parameters for III-V compound semiconductors and their alloys", J. Appl. Phys. **89**, 5815–5875 (2001).

[175] L. V. Butov, A. Zrenner, G. Abstreiter, A. V. Petinova, and K. Eberl, "Direct and indirect magnetoexcitons in symmetric $\mathrm{In}_x\mathrm{Ga}_{1-x}\mathrm{As}$/GaAs coupled quantum wells", Phys. Rev. B **52**, 12153–12157 (1995).

[176] Z. Vörös, R. Balili, D. Snoke, L. Pfeiffer, and K. West, "Long-distance diffusion of excitons in double quantum well structures", Phys. Rev. Lett. **94**, 226401 (2005).

[177] T. Damen, J. Shah, D. Oberli, D. Chemla, J. Cunningham, and J. Kuo, "Dynamics of exciton formation and relaxation in GaAs quantum wells", Phys. Rev. B **42**, 7434–7438 (1990).

[178] A. L. Ivanov, P. B. Littlewood, and H. Haug, "Bose-Einstein statistics in thermalization and photoluminescence of quantum-well excitons", Phys. Rev. B **59**, 5032–5048 (1999).

[179] L. V. Butov, A. L. Ivanov, A. Imamoglu, P. B. Littlewood, A. A. Shashkin, V. T. Dolgopolov, K. L. Campman, and A. C. Gossard, "Stimulated Scattering of Indirect Excitons in Coupled Quantum Wells: Signature of a Degenerate Bose-Gas of Excitons", Phys. Rev. Lett. **86**, 5608–5611 (2001).

[180] M. Henini, *Molecular Beam Epitaxy: From Research to Mass Production* (Elsevier Science, 2012), p. 744.

[181] G. J. Schinner, E. Schubert, M. P. Stallhofer, J. P. Kotthaus, D. Schuh, A. K. Rai, D. Reuter, A. D. Wieck, and A. O. Govorov, "Electrostatically trapping indirect excitons in coupled $\mathrm{In}_x\mathrm{Ga}_{1-x}\mathrm{As}$ quantum wells", Phys. Rev. B **83**, 165308 (2011).

[182] G. Schinner, J. Repp, E. Schubert, A. Rai, D. Reuter, A. Wieck, A. Govorov, A. Holleitner, and J. Kotthaus, "Confinement and Interaction of Single Indirect Excitons in a Voltage-Controlled Trap Formed Inside Double InGaAs Quantum Wells", Phys. Rev. Lett. **110**, 127403 (2013).

[183] K. Sivalertporn, L. Mouchliadis, A. L. Ivanov, R. Philp, and E. A. Muljarov, "Direct and indirect excitons in semiconductor coupled quantum wells in an applied electric field", Phys. Rev. B **85**, 045207 (2012).

[184] S. Moskalenko and D. Snoke, *Bose-Einstein Condensation of Excitons and Biexcitons: And Coherent Nonlinear Optics with Excitons* (Cambridge University Press, 2000), p. 415.

[185] L. V. Keldysh and A. N. Kozlov, "Collective properties of excitons in semiconductors", Sov. Phys. JETP **27**, 521–528 (1968).

[186] K. L. V. Jeffries, C. D., *Electron-hole droplets in semiconductors* (Amsterdam: North-Holland, 1983), p. 656.

[187] A. A. High, J. R. Leonard, M Remeika, L. V. Butov, M Hanson, and A. C. Gossard, "Condensation of Excitons in a Trap", (2012).

[188] Y. Shilo, K. Cohen, B. Laikhtman, K. West, L. Pfeiffer, and R. Rapaport, "Particle correlations and evidence for dark state condensation in a cold dipolar exciton fluid.", Nat. Commun. **4**, 2335 (2013).

[189] L. V. Butov, A. C. Gossard, and D. S. Chemla, "Macroscopically ordered state in an exciton system.", Nature **418**, 751–4 (2002).

[190] S. Yang, A. Hammack, M. Fogler, L. Butov, and A. Gossard, "Coherence Length of Cold Exciton Gases in Coupled Quantum Wells", Phys. Rev. Lett. **97**, 187402 (2006).

[191] M. Remeika, A. T. Hammack, S. V. Poltavtsev, L. V. Butov, J. Wilkes, A. L. Ivanov, K. L. Campman, M. Hanson, and A. C. Gossard, "Pattern formation in the exciton inner ring", Phys. Rev. B **88**, 125307 (2013).

[192] J. Keeling, P. R. Eastham, M. H. Szymanska, and P. B. Littlewood, "BCS-BEC crossover in a system of microcavity polaritons", Phys. Rev. B **72**, 115320 (2005).

[193] M. Yamaguchi, K. Kamide, T. Ogawa, and Y. Yamamoto, "BEC-BCS-laser crossover in Coulomb-correlated electron-hole-photon systems", New J. Phys. **14**, 065001 (2012).

[194] J. Humlíček, E. Schmidt, L. Bočánek, R. Švehla, and K. Ploog, "Exciton line shapes of GaAs/AlAs multiple quantum wells", Phys. Rev. B **48**, 5241–5248 (1993).

[195] M. H. Szymanska and P. B. Littlewood, "Excitonic binding in coupled quantum wells", Phys. Rev. B **67**, 193305 (2003).

[196] H. Haug and S. Schmitt-Rink, "Electron theory of the optical properties of laser-excited semiconductors", Prog. Quantum Electron. **9**, 3–100 (1984).

[197] R. Zimmermann, "Nonlinear optics and the Mott transition in semiconductors", Phys. Status Solidi B **146**, 371–384 (1988).

[198] D. W. Snoke and J. D. Crawford, "Hysteresis in the Mott transition between plasma and insulating gas", Phys. Rev. E **52**, 5796–5799 (1995).

[199] A. Georges, G. Kotliar, W. Krauth, and M. Rozenberg, "Dynamical mean-field theory of strongly correlated fermion systems and the limit of infinite dimensions", Rev. Mod. Phys. **68**, 13–125 (1996).

[200] T. Yoshioka and K. Asano, "Exciton-Mott Physics in a Quasi-One-Dimensional Electron-Hole System", Phys. Rev. Lett. **107**, 256403 (2011).

[201] N. F. Mott, *Metal-Insulator Transitions*, 1st ed., Vol. 1 (Taylor& Francis Ltd, London, 1974), p. 278.

[202] A. Amo, M. D. Marti'n, L. Viña, A. I. Toropov, and K. S. Zhuravlev, "Photoluminescence dynamics in GaAs along an optically induced Mott transition", J. Appl. Phys. **101**, 081717 (2007).

[203] C. Schindler and R. Zimmermann, "Analysis of the exciton-exciton interaction in semiconductor quantum wells", Phys. Rev. B **78**, 045313 (2008).

[204] J. Černe, J Kono, M. S. Sherwin, M Sundaram, A. C. Gossard, and G. E. W. Bauer, "Terahertz Dynamics of Excitons in GaAs/AlGaAs Quantum Wells", Phys. Rev. Lett. **77**, 1131–1134 (1996).

[205] S. Ben-Tabou de Leon and B. Laikhtman, "Exciton-exciton interactions in quantum wells: Optical properties and energy and spin relaxation", Phys. Rev. B **63**, 125306 (2001).

[206] F. Boldt, K. Henneberger, and V. May, "Many-Body Theory for the Dense Exciton Gas of Direct Semiconductors II. Calculation of Exciton Level Shift and Damping in Dependence on Exciton Density", Phys. status solidi **130**, 675–687 (1985).

[207] D. Snoke, "Predicting the ionization threshold for carriers in excited semiconductors", Solid State Commun. **146**, 73–77 (2008).

[208] A. A. High, A. T. Hammack, L. V. Butov, L Mouchliadis, A. L. Ivanov, M Hanson, and A. C. Gossard, "Indirect excitons in elevated traps.", Nano Lett. **9**, 2094–2098 (2009).

[209] V. I. Sugakov, "Exciton condensation in quantum wells. Exciton hydrodynamics. The effect of localized states", Condens. Matter Phys. **17**, 33702 (2014).

[210] R. Höger, E. O. Gobel, J. Kuhl, K. Ploog, and H. J. Quiesser, "Kinetics of free and bound excitons in GaAs/AlGaAs double heterostructures", J. Phys. C Solid State Phys. **17**, L905–L910 (1984).

[211] K Leosson, J. R. Jensen, W Langbein, and J. M. Hvam, "Exciton localization and interface roughness in growth-interrupted GaAs/AlAs quantum wells", Phys. Rev. B **61**, 10322–10329 (2000).

[212] A. A. Dremin, V. B. Timofeev, A. V. Larionov, J. Hvam, and K. Soerensen, "Phase diagram of the Bose condensation of interwell excitons in GaAs/AlGaAs double quantum wells", J. Exp. Theor. Phys. Lett. **76**, 450–455 (2002).

[213] A. G. Cui, Y. J. Ding, S. J. Lee, J. V. D. Veliadis, J. B. Khurgin, S. Li, D. C. Reynolds, and J. Grata, "Spatially localized band-gap renormalization and band-filling effects in three growth-interrupted multiple asymmetric coupled narrow quantum wells", J. Opt. Soc. Am. B **13**, 536–545 (1996).

[214] M. Combescot and M. N. Leuenberger, "General argument supporting Bose-Einstein condensate of dark excitons in single and double quantum wells", Solid State Commun. **149**, 567–571 (2009).